

GALVANIC CORROSION OF ALUMINUM COUPLED TO PASSIVATING AND NON-PASSIVATING ALLOYS

A THESIS SUBMITTED TO THE GRADUATE DIVISION OF THE UNIVERSITY OF
HAWAII AT MĀNOA IN PARTIAL FULFILLMENT OF THE REQUIREMENTS FOR THE
DEGREE OF

MASTER OF SCIENCE

IN

MECHANICAL ENGINEERING

December 2016

By

Kathleen F. Quiambao

Thesis Committee:

Lloyd H. Hihara, Chairperson

Mehrdad N. Ghasemi Nejhada

Scott F. Miller

Acknowledgements

Foremost, I would like to sincerely thank my advisor Dr. Lloyd Hihara for his continuous support of my research in every capacity. His knowledge, patience, and devotion to the members of his lab are unparalleled, and the guidance I have received from him in the early stages of my research career has been invaluable in shaping me as a scientist.

I would like to thank my committee members, Dr. Mehrdad Nejhad and Dr. Scott Miller for agreeing to serve on my thesis committee and for their input in the writing of my thesis.

I am very grateful for the support of the project entitled “Galvanic Corrosion Studies of Aluminum Coupled to Non-Passivating and Passivating Alloys in Diverse Micro-Climates” funded by the US Air Force Academy. I am particularly grateful to Daniel Dunmire, Richard Hays, Larry Lee, William Abbott, Gregory Shoales, David Robertson, and Christopher Scurlock of the Technical Corrosion Collaboration sponsored by the Office of Corrosion Policy and Oversight, Office of the Under Secretary of Defense. I would like to thank Joseph Leone, Lightning support team, Luke AFB, AZ, and Andrew Sheetz of the Naval Surface Warfare Center Carderock Division, USMC Corrosion Prevention and Control Program for their initial input for the project.

I would like to thank the current and former members of the Hawai`i Corrosion Lab for their support during the duration of my thesis: Mr. Brent Howard, Mr. Khoa Huynh, Mr. Dan Jensen, Mrs. Jan Kealoha, Mr. Jeff Nelson, Ms. Melissa Sanders, and Ms. Natalie Wohner.

Special thanks to Dr. Raghu Srinivasan for imparting knowledge related to my thesis, his guidance in demonstrating laboratory techniques, and providing preliminary data.

I would especially like to thank Mr. Ryan Sugamoto for his assistance in the design of my thesis project, his superb lab management skills, and his exceptional patience and kindness towards each member of the Hawai`i Corrosion Lab. The progress on this project is largely attributed to him and for that I am forever grateful.

Lastly, I am forever thankful for the love and support of my family during the entire duration of my academic studies thus far. The words of encouragement from my siblings and the unwavering support my parents have provided have contributed immensely to my accomplishments. Every one of my achievements now and henceforth is dedicated to them.

Abstract

Galvanic corrosion of 6061-T6 aluminum-coupled metals was studied in marine, volcanic, and rainforest environments. In addition to field research, galvanic couples were subjected to the chloride-containing GM-9540P accelerated corrosion test. The galvanic couple types included 6061-T6 Al with Ti-6Al-4V, 316 stainless steel, silver, copper, 1018 steel, and Mg AZ31B connected via insulating fasteners.

In this research, galvanic corrosion currents were measured through portable data loggers connected to each metal in the aluminum-coupled specimens. The total corrosion on an anode in a galvanic couple results from galvanic corrosion between the anode and the cathode plus additional simultaneous local corrosion on the anode caused by cathodic reactions occurring on the anode. The value of the total corrosion rate, that is, local corrosion and galvanic corrosion, was determined by mass loss of the galvanically-coupled aluminum coupons. The local corrosion was determined using the difference between the total corrosion rate and the galvanic corrosion rate, as determined from the galvanic current data and Faraday's law. The mass loss of the coupons was also compared to those of uncoupled aluminum coupons which were not subjected to galvanic corrosion. Corroded aluminum samples were subjected to surface analysis using SEM/EDXA and XRD. Potentiodynamic polarization and pH experiments were also conducted in order to study the mechanisms of galvanic corrosion for the couples described above.

Table of Contents

Section	Page #
Acknowledgements.....	i
Abstract.....	ii
List of Figures.....	vi
List of Tables.....	xi
Chapter 1. Introduction	
1.1. Theory.....	1
1.2. Background.....	3
1.3. Research objectives.....	4
Chapter 2. Literature Review	
2.1. Pitting corrosion of aluminum.....	6
2.2. Atmospheric corrosion of aluminum alloys.....	7
2.3. Galvanic corrosion of aluminum-coupled metals.....	8
Chapter 3. Preliminary Experiments	
3.1. Observation of pH change in galvanic couples.....	10
3.2. Potentiodynamic polarization.....	12
Chapter 4. Experimental Procedures for Environmental Exposure	
4.1. Galvanic couple specimen assembly.....	23
4.2. Support system.....	23
4.3. Data logger configuration.....	24
4.4. Specimen exposure.....	26
Chapter 5. Determination of Corrosion Rate	
5.1. Total mass loss.....	31

5.2. Galvanic mass loss.....	41
5.3. Discussion of mass loss.....	44
Chapter 6. Surface Analysis	
6.1. Scanning electron microscopy and energy-dispersive X-ray analysis.....	49
6.1.1. Test specimens at Marine Corps Base Hawaii.....	49
6.1.2. Test specimens at Lyon Arboretum.....	62
6.1.3. Test specimens at Kilauea Volcanoes National Park.....	70
6.1.4. Test specimens in the cyclic corrosion testing chamber.....	76
6.2. X-ray diffraction analysis.....	81
6.2.1. Comparison of Al spectra by location.....	81
6.2.2. Comparison of Al spectra by couple type.....	90
Chapter 7. Conclusions.....	95

List of Figures

Figure	Page #
Fig. 1: Galvanic couple schematic exhibiting galvanic corrosion and local corrosion.....	2
Fig. 2: Galvanic couples of Al-Cu, Al-stainless steel, Al-Mg, and Al-Ag, Al-Ti, and Al-mild steel after	
a. 0 hours (5-minutes exposure)	
b. 4 hours	
c. 12 hours	
d. 24 hours	
e. 36 hours	
f. 48 hours.....	12
Fig. 3: Cathodic Ag and anodic Al polarization in 3.15 wt% NaCl solution.....	14
Fig. 4: Cathodic Cu and anodic Al polarization in 3.15 wt% NaCl solution.....	14
Fig. 5: Cathodic Ti and anodic Al polarization in 3.15 wt% NaCl solution.....	15
Fig. 6: Cathodic stainless steel and anodic Al polarization in 3.15 wt% NaCl solution.....	15
Fig. 7: Cathodic mild steel and anodic Al polarization in 3.15 wt% NaCl solution.....	16
Fig. 8: Cathodic Al and anodic Mg polarization in 3.15 wt% NaCl solution.....	16
Fig. 9: Cathodic Ag and anodic Al polarization in 0.5 M Na ₂ SO ₄ solution.....	17
Fig. 10: Cathodic Cu and anodic Al polarization in 0.5 M Na ₂ SO ₄ solution.....	17
Fig. 11: Cathodic Ti and anodic Al polarization in 0.5 M Na ₂ SO ₄ solution.....	18
Fig. 12: Cathodic stainless steel and anodic Al polarization in 0.5 M Na ₂ SO ₄ solution.....	18
Fig. 13: Cathodic Al and anodic mild steel polarization in 0.5 M Na ₂ SO ₄ solution.....	19
Fig. 14: Cathodic Al and anodic Mg polarization in 0.5 M Na ₂ SO ₄ solution.....	19
Fig. 15: Overlay of anodic and cathodic polarization curves in 3.15 wt% NaCl solution....	20
Fig. 16: Overlay of anodic and cathodic polarization curves in 0.5 M Na ₂ SO ₄ solution.....	20
Fig. 17: Assembled galvanic couple	
a. Schematic	
b. Assembled and mounted Al-Cu couple pre-environmental exposure.....	23

Fig. 18: Face plate containing Al-Cu galvanic couples and uncoupled Cu.....	24
Fig. 19: Illustration of support system.....	24
Fig. 20: Wiring schematic of voltage data loggers.....	25
Fig. 21: Top view of enclosed data loggers.....	25
Fig. 22: Color-coded cable joints outside of logger box.....	25
Fig. 23: Experimental specimens at	
a. CCTC	
b. MCBH	
c. Kilauea	
d. Lyon Arboretum.....	26
Fig. 24: Environmental conditions of the GM-9540P accelerated corrosion test.....	27
Fig. 25: Galvanic couples following four cycles of the GM-9540P test consisting of	
a. Al and Ag	
b. Al and stainless steel	
c. Al and mild steel	
d. Al and Mg	
e. Al and Ti	
f. Al and Cu.....	27
Fig. 26: Galvanic couples after one month of exposure at MCBH consisting of	
a. Al and Ag	
b. Al and stainless steel	
c. Al and mild steel	
d. Al and Mg	
e. Al and Ti	
f. Al and Cu.....	29
Fig. 27: Galvanic couples after one month of exposure at Kilauea consisting of	
a. Al and Ag	
b. Al and stainless steel	
c. Al and mild steel	
d. Al and Mg	
e. Al and Ti	
f. Al and Cu.....	30
Fig. 28: Galvanic couples after one month of exposure at Lyon Arboretum consisting of	
a. Al and Ag	
b. Al and stainless steel	
c. Al and mild steel	

d. Al and Mg	
e. Al and Ti	
f. Al and Cu.....	31
Fig. 29: SEM of uncoupled Al exposed at MCBH.....	49
Fig. 30: SEM of uncovered region of Al coupled to Ag exposed at MCBH.....	51
Fig. 31: SEM of interface between covered and uncovered regions of Al coupled to Ag at MCBH.....	52
Fig. 32: SEM of uncovered region of Al coupled to Cu exposed at MCBH.....	53
Fig. 33: SEM of covered region of Al coupled to Cu exposed at MCBH.....	54
Fig. 34: SEM of uncovered region of Al coupled to Ti exposed at MCBH.....	55
Fig. 35: SEM of uncovered region of Al coupled to stainless steel exposed at MCBH.....	56
Fig. 36: SEM of boron salts found on Al coupled to stainless steel at MCBH.....	57
Fig. 37: SEM of covered region of Al coupled to stainless steel near the crevice mouth exposed at MCBH.....	57
Fig. 38: SEM of uncovered region of Al coupled to mild steel exposed at MCBH.....	58
Fig. 39: SEM of the interface between covered and uncovered regions of Al coupled to mild steel at MCBH.....	59
Fig. 40: SEM of uncovered region of Al coupled to Mg exposed at MCBH.....	60
Fig. 41: SEM comparison of corrosion in covered regions of Al coupled to Mg and Al coupled to Ag exposed at MCBH.....	61
Fig. 42: SEM of uncoupled Al exposed at Lyon Arboretum.....	62
Fig. 43: SEM of uncovered region of Al coupled to Ag exposed at Lyon Arboretum.....	63
Fig. 44: SEM of surface cracking on the uncovered region of Al coupled to Cu at Lyon Arboretum.....	64
Fig. 45: SEM of covered region of Al coupled to Cu exposed at Lyon Arboretum.....	65
Fig. 46: SEM of covered region of Al coupled to mild steel exposed at Lyon Arboretum...	66

Fig. 47: SEM of covered and uncovered regions of Al coupled to Ti exposed at Lyon Arboretum.....	67
Fig. 48: SEM of covered and uncovered regions of Al coupled to stainless steel exposed at Lyon Arboretum.....	68
Fig. 49: SEM of covered and uncovered regions of Al coupled to Mg exposed at Lyon Arboretum.....	69
Fig. 50: SEM of uncoupled Al exposed at Kilauea.....	70
Fig. 51: SEM of uncovered region of Al coupled to Ag exposed at Kilauea.....	71
Fig. 52: SEM of uncovered region of Al coupled to Cu exposed at Kilauea.....	71
Fig. 53: SEM of uncovered region of Al coupled to Ti exposed at Kilauea.....	72
Fig. 54: SEM of uncovered region of Al coupled to stainless steel exposed at Kilauea.....	73
Fig. 55: SEM of pit on the uncovered region of Al coupled to stainless steel at Kilauea.....	74
Fig. 56: SEM of uncovered region of Al coupled to mild steel exposed at Kilauea.....	75
Fig. 57: Uncovered region of Al coupled to Mg exposed at Kilauea.....	75
Fig. 58: SEM of uncovered region of Al coupled to stainless steel exposed in the CCTC...	76
Fig. 59: SEM of covered region of Al coupled to Ag exposed in the CCTC.....	77
Fig. 60: SEM of covered region of Al coupled to Cu exposed in the CCTC.....	78
Fig. 61: SEM of uncovered region of Al coupled to Ti exposed in the CCTC.....	79
Fig. 62: SEM of uncovered region of Al coupled to Mg exposed in the CCTC.....	79
Fig. 63: SEM of covered region of Al coupled to mild steel exposed in the CCTC.....	80
Fig. 64: XRD spectra of virgin Al coupon.....	81
Fig. 65: XRD spectra overlay of unexposed Al at each exposure location.....	82
Fig. 66: XRD spectra overlay of Al coupled to Ag at each exposure location.....	84
Fig. 67: XRD spectra overlay of Al coupled to Cu at each exposure location.....	85
Fig. 68: XRD spectra overlay of Al coupled to Ti at each exposure location.....	86

Fig. 69: XRD spectra overlay of Al coupled to stainless steel at each exposure location.....	87
Fig. 70: XRD spectra overlay of Al coupled to mild steel at each exposure location.....	88
Fig. 71: Overlay of Mg coupled to stainless steel at each exposure location.....	89
Fig. 72: XRD spectra overlay of all exposed Al types at Lyon Arboretum.....	90
Fig. 73: XRD spectra overlay of all exposed Al types at MCBH.....	91
Fig. 74: XRD spectra overlay of all exposed Al types at Kilauea.....	92
Fig. 75: Overlay of all exposed Al types in the CCTC.....	94

List of Tables

Table	Page #
Table 1: Alloying elements of all experimental alloys.....	4
Table 2: Open circuit potentials for all experimental metals.....	13
Table 3: Extrapolated i_{galv} values.....	21
Table 4: Average penetration rate of Al coupled to Ag.....	33
Table 5: Average penetration rate of Al coupled to Cu.....	33
Table 6: Average penetration rate of Al coupled to Ti.....	34
Table 7: Average penetration rate of Al coupled to stainless steel.....	34
Table 8: Average penetration rate of Al coupled to mild steel.....	35
Table 9: Average penetration rate of Al coupled to Mg.....	35
Table 10: Average penetration rate of Al coupled to Al.....	36
Table 11: Average penetration rate of Mg coupled to Al.....	36
Table 12: Average mass loss ratios between different orientations of Al coupled to Ag.....	37
Table 13: Average mass loss ratios between different orientations of Al coupled to Cu.....	38
Table 14: Average mass loss ratios between different orientations of Al coupled to Ti.....	38
Table 15: Average mass loss ratios between different orientations of Al coupled to stainless steel.....	39
Table 16: Average mass loss ratios between different orientations of Al coupled to mild steel.....	39
Table 17: Average mass loss ratios between different orientations of Al coupled to Mg.....	40
Table 18: Average mass loss ratios between different orientations of Mg coupled to Al.....	40
Table 19: Parameters used to calculate mass loss and penetration rate due to galvanic current for each anode.....	41
Table 20: Calculated mass loss of Al due to galvanic current.....	42

Table 21: Calculated mass loss of Mg due to galvanic current.....	42
Table 22: Calculated penetration rate of Al due to galvanic current.....	42
Table 23: Calculated penetration rate of Mg due to galvanic current.....	43
Table 24: Percent of total Al corrosion due to calculated galvanic corrosion.....	43
Table 25: Percent of total Mg corrosion due to calculated galvanic corrosion.....	43
Table 26: Elemental composition of regions shown in Fig. 29.....	50
Table 27: Elemental composition of regions shown in Fig. 31.....	52
Table 28: Elemental composition of regions shown in Fig. 33.....	54
Table 29: Elemental composition of regions shown in Fig. 35.....	56
Table 30: Elemental composition of the covered region shown in Fig. 39.....	59
Table 31: Elemental composition of region shown in Fig. 42.....	62
Table 32: Elemental composition of region shown in Fig. 32.....	64
Table 33: Elemental composition of region shown in Fig. 45.....	65
Table 34: Elemental composition of region shown in Fig. 46.....	66
Table 35: Elemental composition of regions shown in Fig. 50.....	70
Table 36: Elemental composition of region shown in Fig. 51.....	71
Table 37: Elemental composition of regions shown in Fig. 52.....	72
Table 38: Elemental composition of region shown in Fig. 53.....	72
Table 39: Elemental composition of region shown in Fig. 54.....	73
Table 40: Elemental composition of inclusion shown in Fig. 55.....	74
Table 41: Elemental composition of region shown in Fig. 56.....	75
Table 42: Elemental composition of regions shown in Fig. 58.....	76
Table 43: Elemental composition of regions shown in Fig. 59.....	77

Table 44: Elemental composition of region shown in Fig. 60.....	78
Table 45: Elemental composition of region shown in Fig. 61.....	79
Table 46: Elemental composition of region shown in Fig. 62.....	80
Table 47: Elemental composition of region shown in Fig. 63.....	80

Chapter 1: Introduction

Aluminum alloys are used ubiquitously in commercial manufacture and laboratory applications due to its availability, mechanical properties, light weight, and high corrosion resistance. The natural passivation of aluminum is a major component in the relatively high corrosion resistance of aluminum compared to other metals in practical use. However, in practical use aluminum is commonly used in combination with components of different types of materials which provide the desired properties. In this research, the aluminum alloy 6061-T6, one of the most common general-purpose aluminum alloys which contains silicon and magnesium as its main alloying elements, is analyzed for its corrosion behavior to other passivating metals (titanium alloy 6Al-4V and 316 stainless steel), non-passivating active metals (1018 mild steel and magnesium alloy AZ31B), and elemental noble metals (copper and silver). Aluminum alloy 6061-T6 will henceforth be referred to as **Al**, titanium alloy 6Al-4V as **Ti**, 316 stainless steel as **stainless steel**, 1018 mild steel as **mild steel**, magnesium alloy AZ31B as **Mg**, copper as **Cu**, and silver as **Ag**.

1.1.Theory

Galvanic corrosion is a widely researched electrochemical process and is caused by the flow of current between dissimilar metals in electrical contact.¹ In an electrolytic solution, this current, called galvanic current, electrons flow from the anode to the cathode in the galvanic couple and thereby increases the corrosion rate of the anode. Local corrosion on the anode also occurs due to the formation of local cathodic sites on the anode surface. The total corrosion rate i_{total} can therefore be summarized as:

$$i_{\text{total}} = i_{\text{galv}} + i_{\text{local}} \quad (\text{Eq. 1})$$

where i_{galv} is the galvanic component of corrosion and i_{local} is the local component of corrosion. The local corrosion rate i_{local} is often estimated as the corrosion rate of an uncoupled metal, called $i_{corr,uncoupled}$; however, the effects of the cathodic material may influence i_{local} in a manner unrelated to the galvanic current. Therefore i_{total} is difficult to predict in practical application without experimental data.

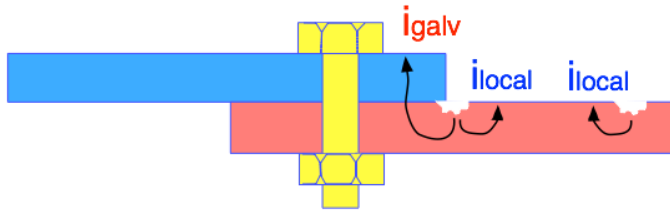


Fig. 1. Galvanic couple schematic exhibiting galvanic corrosion and local corrosion.

Galvanic corrosion of the anode can be quantified using Faraday’s law, which states that the amount of species reacted is proportional to the current and the time that the current flowed.² The mass loss may be calculated using the equation:

$$\partial m = \frac{W \Delta t \sum_j I_j}{n F} \quad (\text{Eq. 2})$$

where W is the atomic weight of the anode, I is the galvanic current, Δt is the time increment for each measurement of I , j is number of iterations for the measurements of I , n is the number of electrons transferred in the half-cell reaction, and F is a Faraday equal to 98,487 Coulombs.

Using the same principle as above, the penetration rate due to galvanic current may also be calculated using known parameters. The penetration rate (PR) uses several of the same parameters in (Eq. 2) and follows the equation:

$$PR = \frac{Q W}{n F \rho t_{exp} \alpha} \quad (\text{Eq. 3})$$

where ρ is the density of the anode, t_{exp} is the total time of exposure, α is the surface area of the anode, and Q is the charge, calculated by the equation:

$$Q = \sum_j I_j \Delta t \quad (\text{Eq. 4})$$

1.2. Background

According to the EMF Series and the Galvanic Series, the standard potentials of Ti, Fe, Cu, and Ag position these metals higher in the series than Al; thus, their position as the more noble metals would name them the cathode in a galvanic couple with Al. Magnesium, however, is lower on both series than aluminum, thus Mg would be the anode when coupled to Al.

Magnesium alloys are commonly used in a process called cathodic protection. As magnesium is the lowest metal in the Galvanic Series, its ability to cathodically polarize a more noble metal is exploited in order to lend corrosion protection to the cathode. In this type of galvanic couple the magnesium is called the sacrificial anode.² Aluminum is frequently used as a sacrificial anode due to its relatively low position on the Galvanic Series, however, its role as the more noble metal when coupled to magnesium lends insight into the behavior of aluminum as a cathode.

The alloying elements of an alloy are significant with regards to local corrosion. As an alloy corrodes, alloying elements may leach out to the surface of the metal and create local cathodic sites thereby increasing corrosion rate. An example relevant to this research is the presence of copper in aluminum alloy 6061-T6; copper is noble to aluminum and therefore its

presence on the surface of the aluminum creates a cathodic site which creates a local action cell and enhances corrosion. The alloying elements of all alloys used in this research are listed in Table 1.

Table 1: Alloying elements of all experimental alloys.

Aluminum Alloy 6061-T6		316 Stainless Steel		Magnesium Alloy AZ31B		Titanium Alloy 6Al-4V		1018 Carbon Steel	
Si	0.4-0.8%	Cr	18%(max)	Al	2.50-3.50%	Al	6%	C	0.14-0.20%
Mg	0.8-1.2%	Ni	14%(max)	Zn	0.60-1.40%	V	4%	Mn	0.60-0.90%
Cu	0.15-0.4%	Mo	3%(max)	Mn	0.20%	Fe	0.25%(max)	P	0.040%(max)
Fe	0.7%(max)	Mn	2%(max)	Si	0.10%	O	0.2%(max)	S	0.050%(max)
Zn	0.25%(max)	Si	1%(max)	Cu	0.050%				
Mn	0.15%(max)	Cr	0.08%(max)	Ca	0.040%				
Ti	0.15%(max)	P	0.045%(max)	Fe	0.0050%				
Cr	0.04-0.35%	S	0.03%(max)	Ni	0.0050%				

The environmental conditions in which the metals are exposed can influence the corrosion properties of a metal. For example, anodic polarization in the presence of halogen ions is shown to cause a passive layer on a metal to break down, thus an environment heavy in chlorides can be highly corrosive due to the ability of chlorides to readily cause pitting corrosion on a passivating metal.²

1.3. Research objectives

The objective of this work is to understand the galvanic corrosion mechanisms of aluminum by obtaining quantitative metrics of aluminum coupled to a variety of metals and exposed to diverse climates. The availability of access to diverse microclimates in Hawaii lends

an opportunity to gain a comprehensive view of the corrosion properties in varying corrosive environments. For this reason the experimental test sites included a marine environment at Marine Corps Base Hawaii (MCBH), a rainforest environment at Lyon Arboretum, a volcanic environment at Kilauea Volcanoes National Park, and in a cyclic corrosion testing chamber subjected to a standardized accelerated corrosion test in the laboratory to simulate outdoor exposure. The large variety of commonly used alloys were selected for this research in order to provide the most practical insight into aluminum-coupled metals and provide data for future modeling of galvanic corrosion of aluminum.

Experimental techniques employed in order to predict galvanic corrosion behavior of aluminum included potentiodynamic polarization to generate mixed-potential plots, and observation of pH change of galvanically-coupled aluminum in a solid electrolyte. Analytical techniques following laboratory and field exposure of the corroded galvanic couples included standardized cleaning in order to obtain mass loss data, calculations of mass loss and penetration rate due to galvanic corrosion using (Eq. 2) and (Eq. 3) based on Faraday's law, and surface analysis techniques including Scanning Electron Microscopy (SEM) in combination with Energy Dispersive X-ray Analysis (EDXA) and X-ray Diffraction (XRD).

Chapter 2: Literature Review

2.1. Pitting corrosion of aluminum

The innate corrosion resistance of aluminum due to its ability to passivate is often reduced by pitting corrosion. Numerous studies have been performed on the effect of chloride ions on pitting corrosion.²⁻⁷ A study by McCafferty describes the sequence of pitting on aluminum by chloride ions, in which the chloride ions adsorb onto the oxide surface and penetrate the passive oxide film, dissolve the aluminum, and propagate by rupture of blisters formed at the metal surface.⁴ Another study on pitting corrosion of aluminum by Szklarska-Smialowska, the author describes the adsorption of chloride ions on the passive film. Szklarska-Smialowska discusses the heterogeneity of the metal surface, which caused a variation in the adsorption of chloride ions to the passive film.⁵ A study by Blanc and Mankowski also describes the pitting corrosion on aluminum alloy 6056 as being partially attributed to the heterogeneous passive film due to the alloy's intermetallic particles.⁶

While chloride ions are known to initiate and propagate pitting corrosion, other ions have been found to suppress corrosion. In a study by Datta, Bhattacharya, and Bandyopadhyay, the effect of Cl^- , Br^- , NO_3^- , and SO_4^{2-} on aluminum alloy 6061 were examined; it was found that while Cl^- increased pitting corrosion, NO_3^- and Br^- were less corrosive and SO_4^{2-} seemed to increase the passivity of the alloy, further reducing the pitting corrosion of the alloy.⁷ The aforementioned study by Szklarska-Smialowska also makes note that the addition of sulfate to the chlorides introduced to the aluminum slowed the chloride adsorption, albeit without ceasing chloride uptake.⁵

The susceptibility of 6*** series aluminum alloys to pitting corrosion is of particular interest for this research. In the previously mentioned study by Blanc and Mankowski, the

authors found that aluminum alloy 6056 was more susceptible to pitting corrosion than aluminum alloy 2024 for lower chloride ion concentrations, while the 2024 alloy was much more susceptible in high chloride ion concentrations.⁶ Similarly in a study by Dan, Muto and Hara, aluminum alloy 6061 experienced more rapidly increasing pitting than aluminum alloy 1100 until a chloride-deposition rate of $100 \text{ mg m}^{-2} \text{ day}^{-1}$ was reached, at which the pitting of the 1100 alloy increased with increased chloride deposition and the pitting of the 6061 alloy decreased with pitting corrosion rate.⁸ These data are significant in a study involving aluminum alloy 6061 so that the corrosion behavior of the alloy may be well-understood.

2.2. Atmospheric corrosion of aluminum alloys

The corrosion behavior of aluminum and aluminum alloys in an atmospheric study is invaluable due to the marked difference in laboratory-induced results versus field results. Atmospheric corrosion data is potentially more representative of corrosion in practical settings. Previous atmospheric corrosion studies of aluminum includes a study by Cui et al. wherein aluminum alloy 7A04 was exposed in a tropical marine atmosphere for four years; one significant finding in this study was that corrosion rate actually slowed long-term due to the buildup of corrosion product over the surface of the metal.⁹ Another study by Ezuber, El-houd, and El-Shawesh examined the corrosion of aluminum alloys 5083 and 1100 in natural seawater. One conclusion of this study was that $\text{Al}_{12}\text{Fe}_3\text{Si}_2$ particles as well as Mg in the alloy were greatly susceptible to pitting corrosion when exposed to sea water.¹⁰ These findings are also pertinent regarding aluminum alloy 6061, as it contains both Al-Fe-Si inclusions and also contains Mg as one of its major alloying elements.

2.3. Galvanic corrosion of aluminum-coupled metals

Previous studies of galvanically-coupled aluminum and aluminum alloys have been surveyed for those involving the metals used in this research. In a similar yet smaller-scale study by Acevedo-Hurtado et al., aluminum alloy 2024 was galvanically coupled to commercially pure Ag and exposed in a tropical marine environment as well as in accelerated corrosion tests ASTM B117 and GM-9540P. The authors findings included pitting corrosion of the aluminum alloy with increased corrosion in the crevice, as well as uniform corrosion on the Ag, albeit minimal Ag corrosion due to protective film formation and galvanic protection. The authors also found that sulfate and oxide deposits inhibit pit nucleation.¹¹

Galvanic corrosion of commercially pure iron and aluminum in NaCl solution was studied by Raj and Nishimura wherein a scanning electrochemical microscope (SECM) was used to determine the sacrificial behavior of aluminum as the anode in the couple. A drop in potential over time was detected by the SECM tip and the concentration of oxygen decreased due to oxygen reduction on the iron.¹²

A study by Rafla et al. of aluminum alloy 7050 coupled to 304 stainless steel in a simulated fastener under droplets of NaCl solution. After 62 hours of NaCl exposure multiple fissures were revealed in the aluminum alloy in the region surrounding the stainless steel wire. These fissures were likely due to both the cathodic action of the stainless steel as well as local cathodic sites inherent in the aluminum alloy.¹³

An atmospheric study of an Al-Cu galvanic couple in a marine environment performed by Vera, Verdugo, Orellana, and Muñoz identified pitting corrosion and exfoliation of the aluminum when coupled to copper as well as crevice corrosion in the lap joint due to galvanic

action. The aluminum corrosion was increased in the presence of environmental copper and sulfur dioxide.¹⁴

In a study of pure aluminum coupled to pure magnesium by Lacroix, Blanc, Pébère, Tribollet, and Vivier, an increase in both the aluminum and the magnesium in the study was observed. Their findings stated that although aluminum is the cathode in an Al-Mg galvanic couple, the dissolution of Mg generating hydroxide ions subsequently led to an increase in pH in the Na₂SO₄ solution in which the couple was immersed, which aided in the degradation of the Al passive layer and thus increased corrosion in both species.¹⁵

Literature was scarce on galvanic corrosion studies of aluminum coupled to titanium, however a theoretical model study of Al coupled to Ti by Younan, Zhiqiang, Siping, and Hao was developed with the goal of mitigating galvanic corrosion on microchip bond pads. The authors proposed solutions to bond pad corrosion based on known reactions of aluminum and titanium corrosion, such as eliminating moisture to prevent oxygen reduction and maintaining aluminum passivation to slow corrosion.¹⁶

Chapter 3: Preliminary Experiments

3.1. Observation of pH change in galvanic couples

One indication of galvanic corrosion is the change in pH on either side of the galvanic cell. As galvanic current passes from the cathode to anode in the presence of an electrolytic solution, the reduction at the cathode facilitates the oxygen reduction reaction, generating hydroxide ions and increasing the pH of the environment surrounding the cathode. Simultaneously, the oxidation of the anode generates metal cations that become hydrated thereby generating hydrogen ions and decreasing the pH of the environment surrounding the anode. This principle is particularly significant in the corrosion of the anode, as the buildup of H^+ ions attracts the anions of the electrolyte solution; the increased presence of aggressive anions (e.g. Cl^-) in the region surrounding the anode may further accelerate corrosion. An experiment was conducted in order to visually observe this effect in the galvanic couple types to be researched in this work.

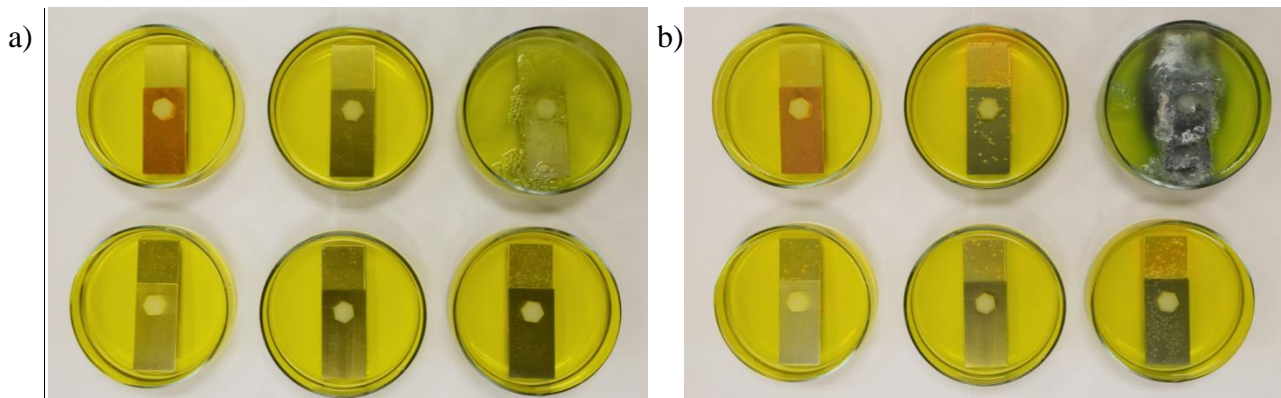
Galvanic couples consisting of Al-Ag, Al-Cu, Al-Ti, Al-stainless steel, Al-mild steel, and Al-Mg were assembled with non-conductive fasteners. A molten agar electrolyte at neutral pH consisting of 3.15 wt% NaCl and a pH indicator solution containing phenolphthalein, bromthymol blue, methyl orange, alizarine yellow R, bromocresol green, and meta cresol purple was poured around each galvanic couple until the couples were enclosed in the solution. The specimens were then left undisturbed to allow for cooling and solidification of the agar and stored in the laboratory at 20°C. Observations were conducted over the 48 hours following the experimental setup.

Gas formation on the Mg side of the Al-Mg galvanic couple was visually apparent immediately (Fig. 2a). Upon addition of the electrolyte to the dish containing the Al-Mg couple,

bubbling of the solution indicated what was likely hydrogen evolution on the Mg surface. However, based on the extreme susceptibility of magnesium to hydrogen evolution, this observed effect may not be entirely attributed to the galvanic corrosion mechanism.² In addition to the immediate hydrogen evolution reaction a slight color change in the agar surrounding the Al coupon in the Al-Mg couple was visible.

Over a period of 4 hours, the dark purple color change of the electrolyte surrounding the Al coupon in the Al-Mg couple indicated a significant increase in alkalinity compared to the local area around the Mg (Fig. 2b). Slight light orange color change indicating acidity around the Al coupons of the Al-stainless steel and the Al-mild steel couples was also observed after 4 hours in the solid electrolyte. Gas formation for all couples was indicated by bubble formation in the agar, likely due to hydrogen formation at the cathodic sites.

After 24 hours, color differentials on the Al-Ag, Al-stainless steel, and the Al-mild steel couples were observed, demarking the anodic region and the cathodic regions wherein the Al side was anodic and the corresponding metal side was cathodic (Fig. 2c). After 48 hours all galvanic couples displayed gas formation and a pH change in the local environment, albeit less pronounced in the Al-Cu and Al-Ti couples.



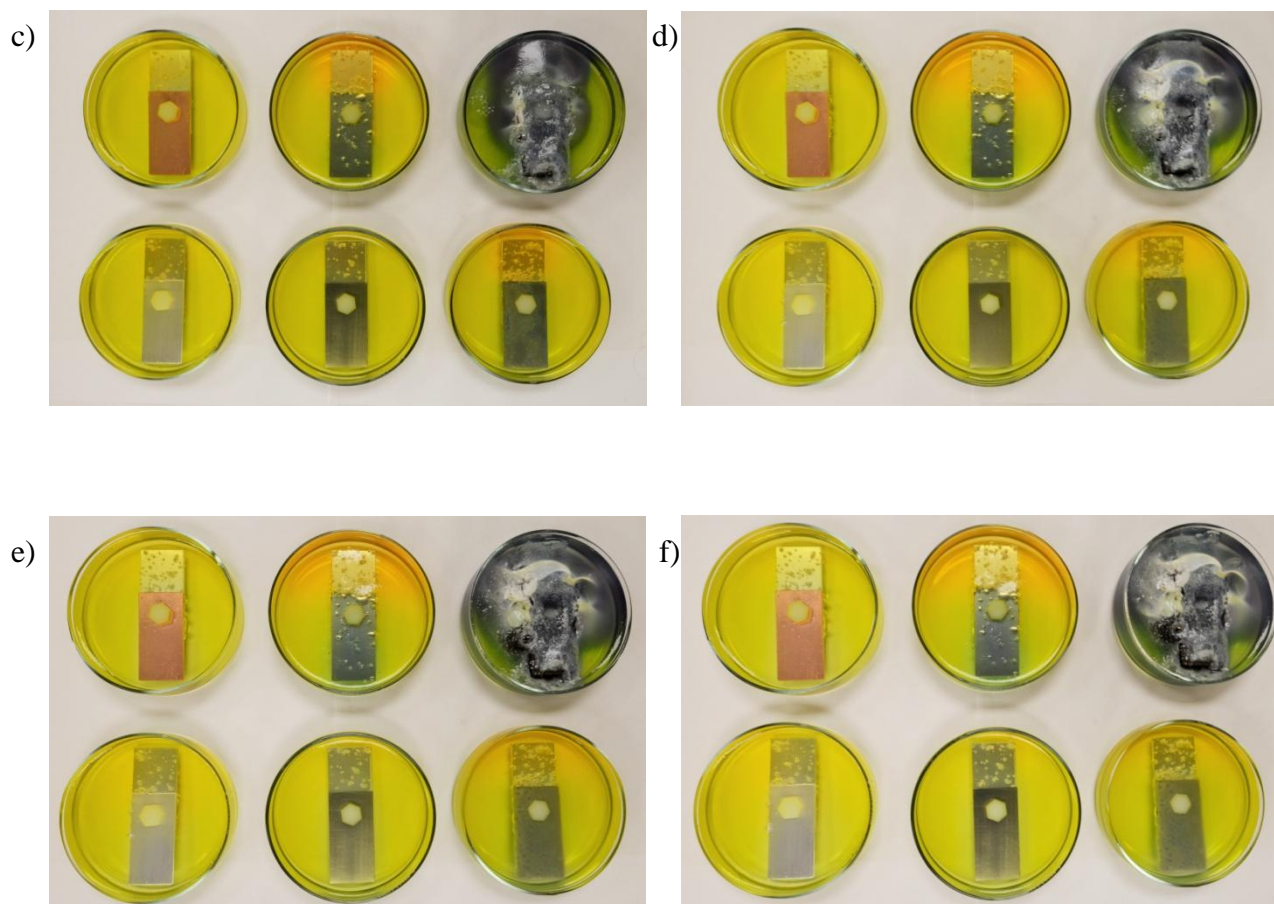


Fig. 2. Galvanic couples of (left to right, 1st row) Al-Cu, Al-stainless steel, Al-Mg, and (left to right, 2nd row) Al-Ag, Al-Ti, and Al-mild steel after a) 0 hours (5-minutes exposure), b) 4 hours, c) 12 hours, d) 24 hours, e) 36 hours, and f) 48 hours.

3.2. Potentiodynamic polarization

Potentiodynamic polarization experiments were performed using the Parstat 2273 Advanced Potentiostat with 1-cm. x 1-cm. electrodes in aerated solutions of 3.15 wt% NaCl and 0.5 M Na₂SO₄ against a Saturated Calomel Electrode (SCE) with KCl. First, open-circuit potentials (OCP) were obtained over a one-hour period for Al, Ag, Cu, Ti, stainless steel, and mild steel, and over a 30-minute period for Mg. The aerated solutions were sparged with air at a volumetric rate of 320-370 mL/min at a pressure of 1 atm. This rate was held constant for all of

the polarization tests. The average OCP values for each metal in the NaCl and Na₂SO₄ solutions are displayed in Table 2.

Table 2: Open circuit potentials for all experimental metals.

Metal	Average OCP in aerated 3.15 wt% NaCl (V vs. SCE)	Average OCP in aerated 0.5 M Na ₂ SO ₄ (V vs. SCE)
AA6061-T6	-0.790	-0.482
Silver	-0.0880	0.0943
Copper	-0.253	-0.0722
Ti 6Al-4V	-0.459	-0.303
316 Stainless Steel	-0.148	-0.221
1018 Mild Steel	-0.582	-0.628
Mg AZ31B	-1.60	-1.60

The OCP values of Al, Ag, Cu, Ti, stainless steel, and mild steel in NaCl indicate these metals as the cathode when coupled to Al, as the Al has a lower potential than all values listed for the aforementioned metals. However, in Na₂SO₄ solution the OCP for mild steel was higher than that of Al. This indicates that in an Al-mild steel galvanic couple, the designation of the anode and cathode may switch depending on the ions in the surrounding environment. Al has a higher potential than Mg in both solutions, indicating Al as the cathode in both cases.

The OCP values for Al, Ag, Cu, Ti, were lower in NaCl solution than in Na₂SO₄ solution while the stainless steel and mild steel displayed lower OCP values in the Na₂SO₄ solution than in the NaCl solution.

Thus, in NaCl solution cathodic polarization curves for Ag, Cu, Ti, stainless steel, and mild steel were obtained, and anodic polarization curves for Mg were obtained (Figs. 3-8). In Na₂SO₄ solution, cathodic polarization curves for Ag, Cu, Ti, and stainless steel were obtained, as well as anodic polarization curves for mild steel and Mg (Figs. 9-14). These polarization

curves were overlain with the corresponding anodic or cathodic curve for Al. Figs. 15 and 16 display overlays of all polarization curves obtained in NaCl and Na₂SO₄ solution, respectively.

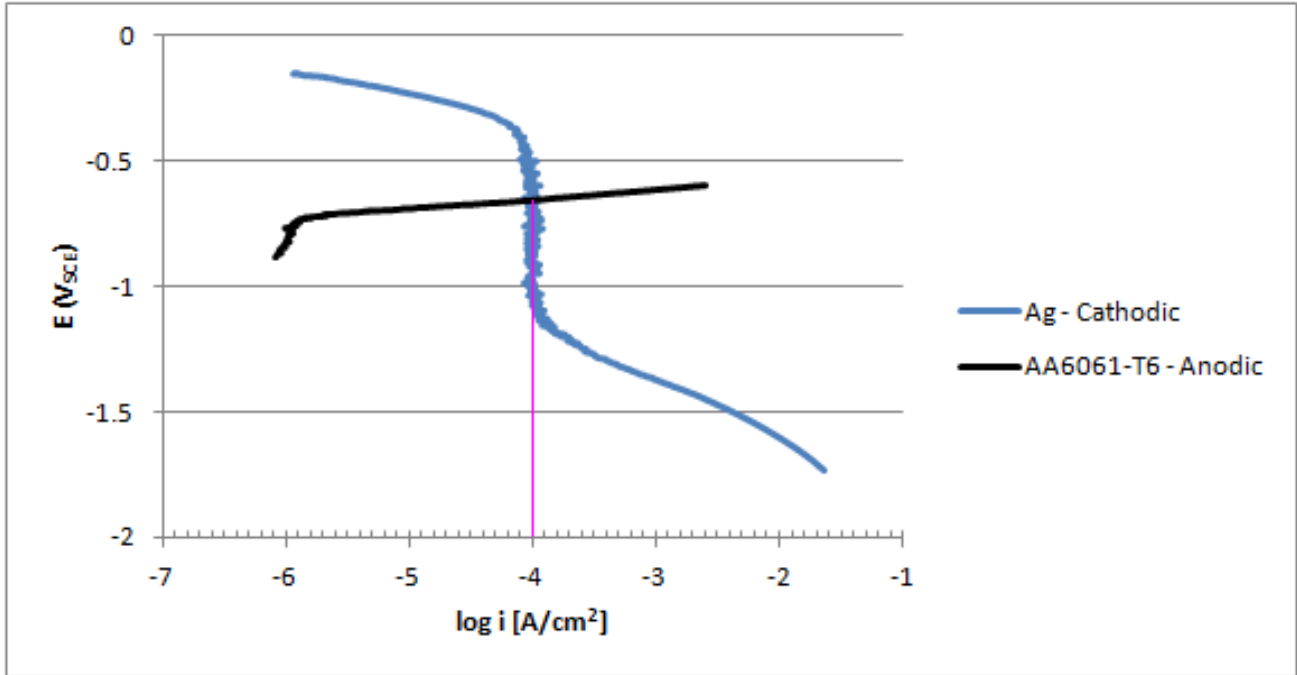


Fig. 3. Cathodic Ag and anodic Al polarization in 3.15 wt% NaCl solution.

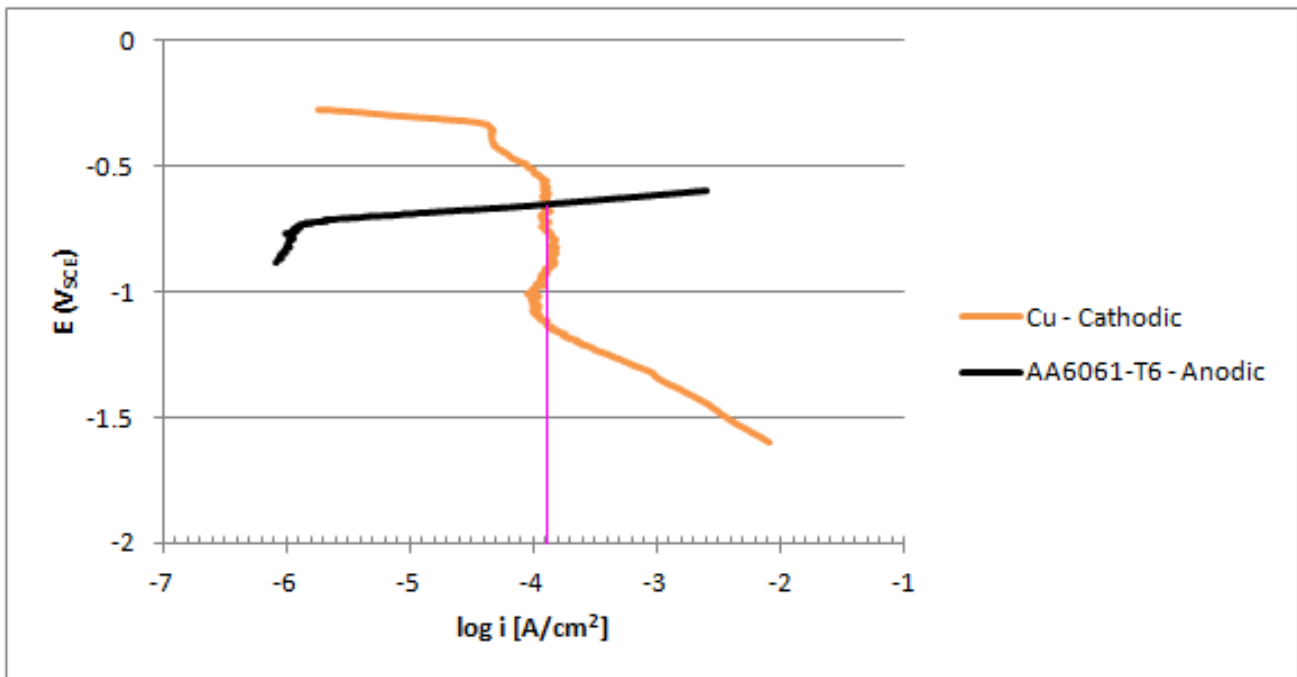


Fig. 4. Cathodic Cu and anodic Al polarization in 3.15 wt% NaCl solution.

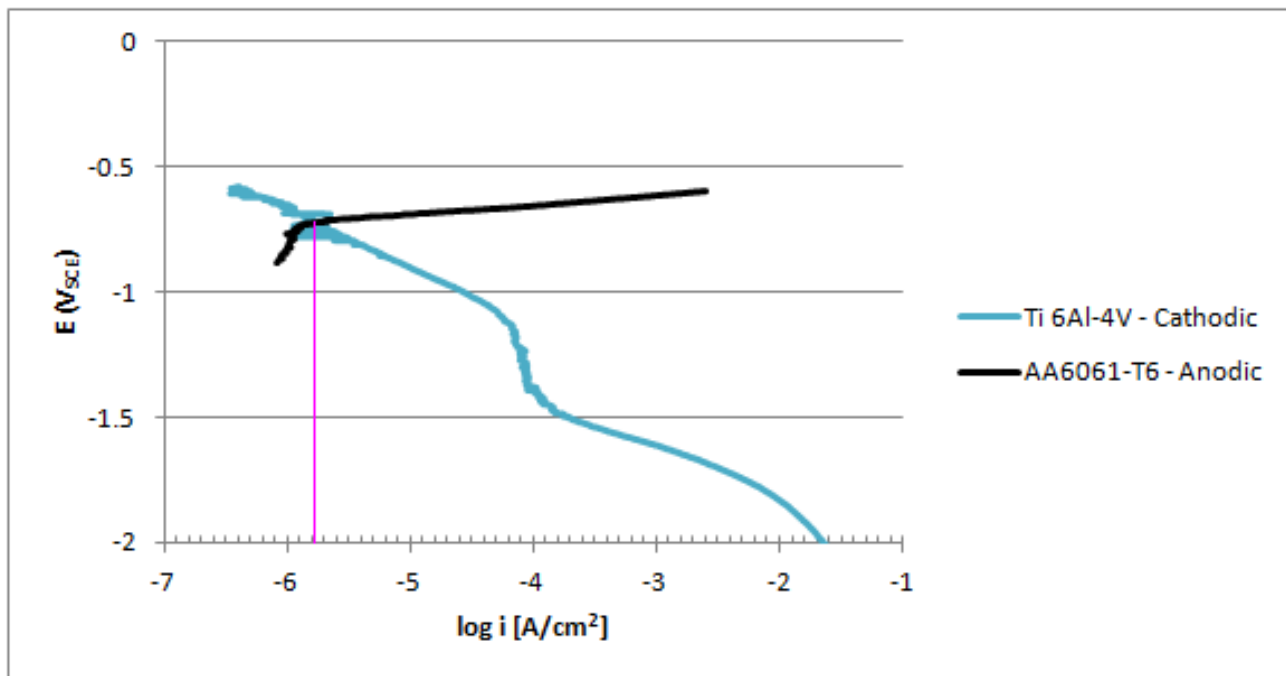


Fig. 5. Cathodic Ti and anodic Al polarization in 3.15 wt% NaCl solution.

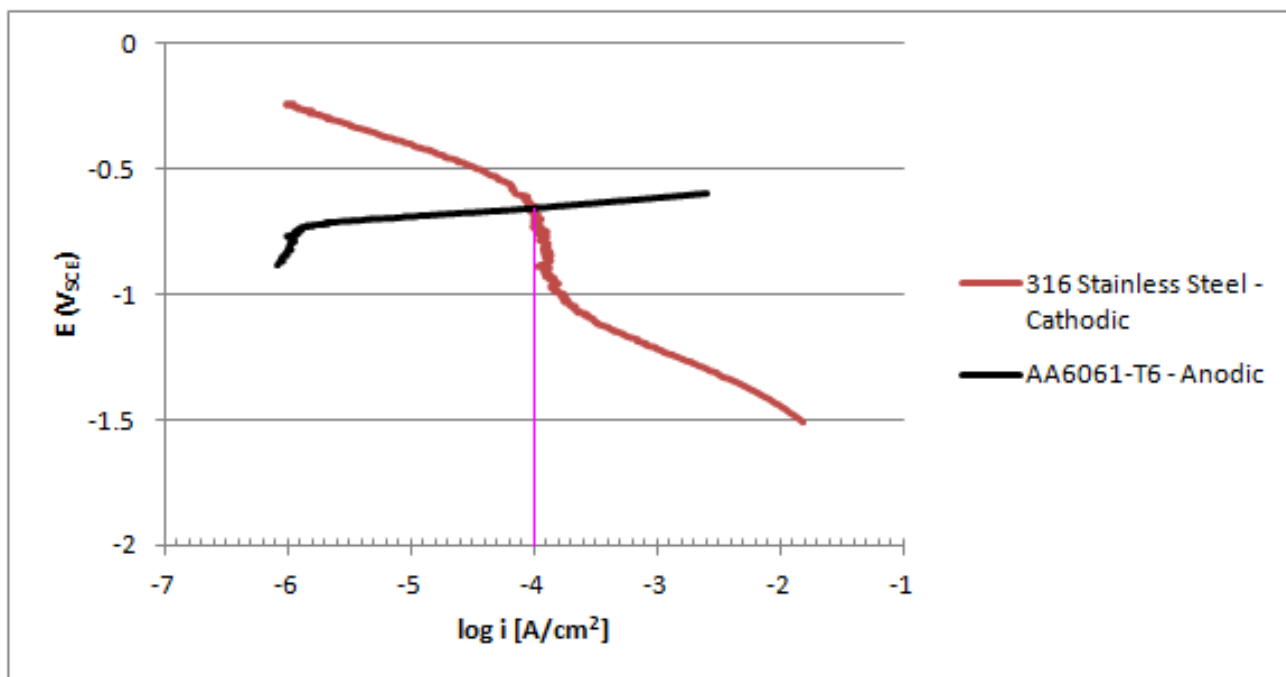


Fig. 6. Cathodic stainless steel and anodic Al polarization in 3.15 wt% NaCl solution.

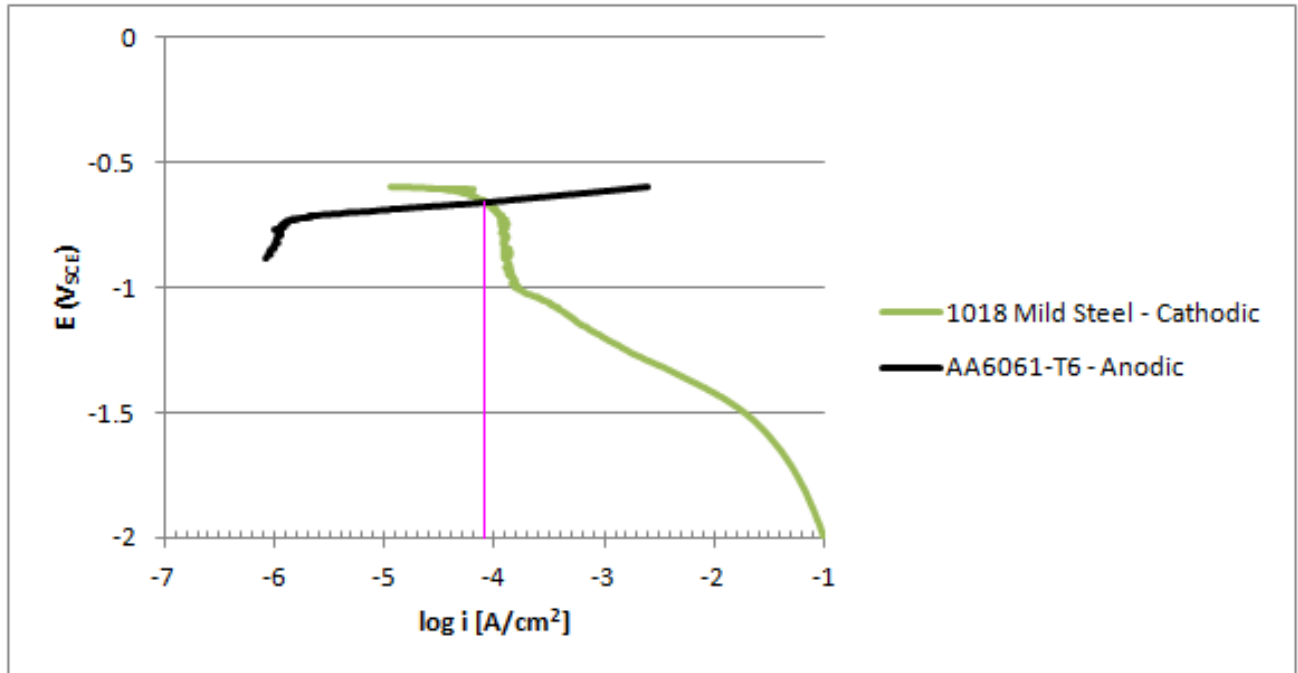


Fig. 7. Cathodic mild steel and anodic Al polarization in 3.15 wt% NaCl solution.

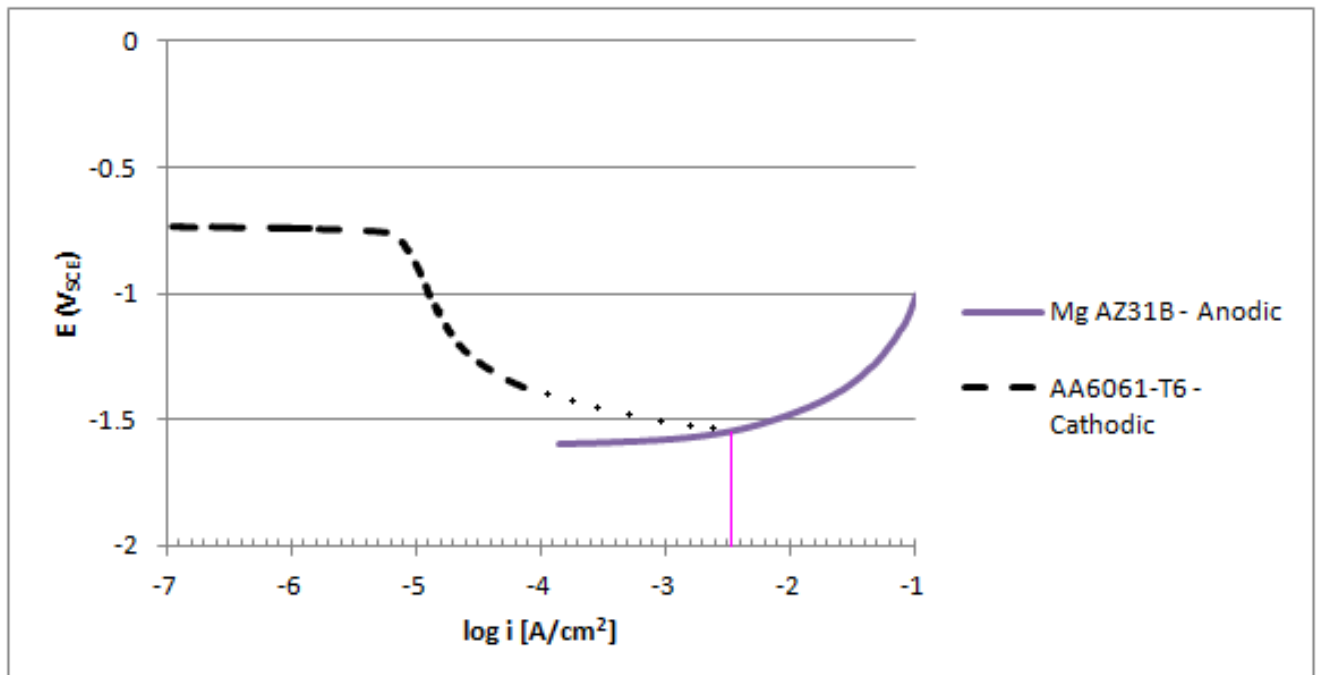


Fig. 8. Cathodic Al and anodic Mg polarization in 3.15 wt% NaCl solution.

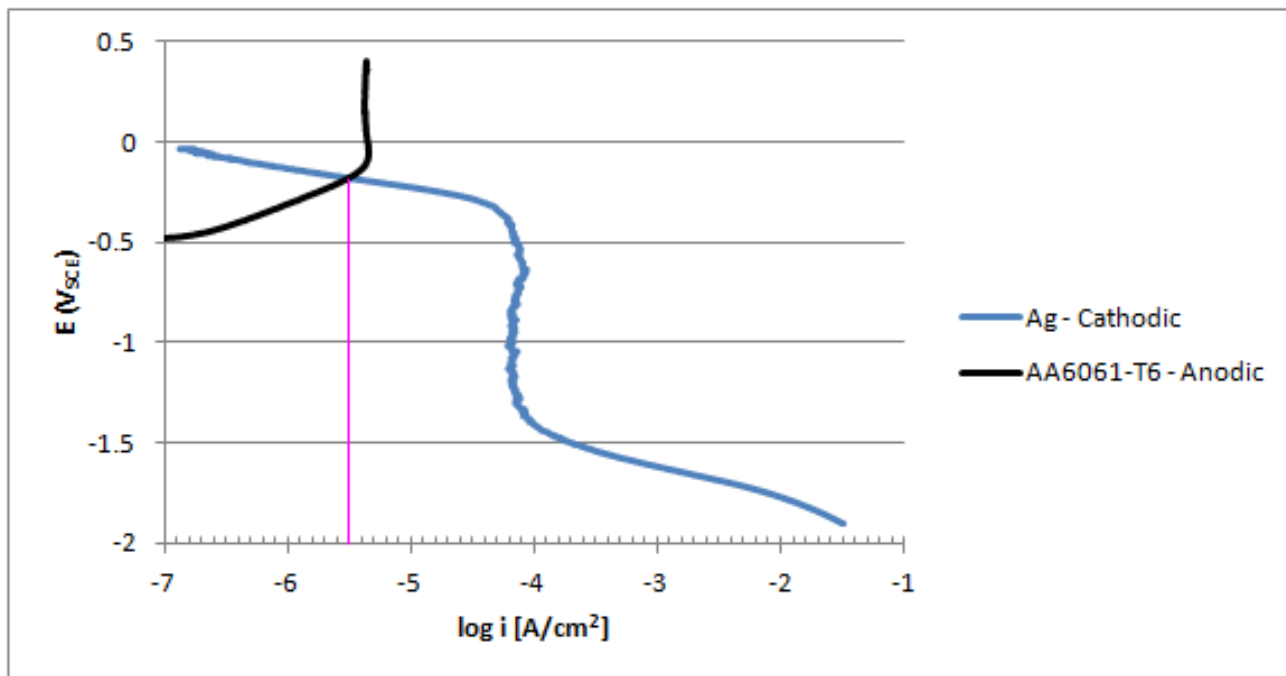


Fig. 9. Cathodic Ag and anodic Al polarization in 0.5 M Na₂SO₄ solution.

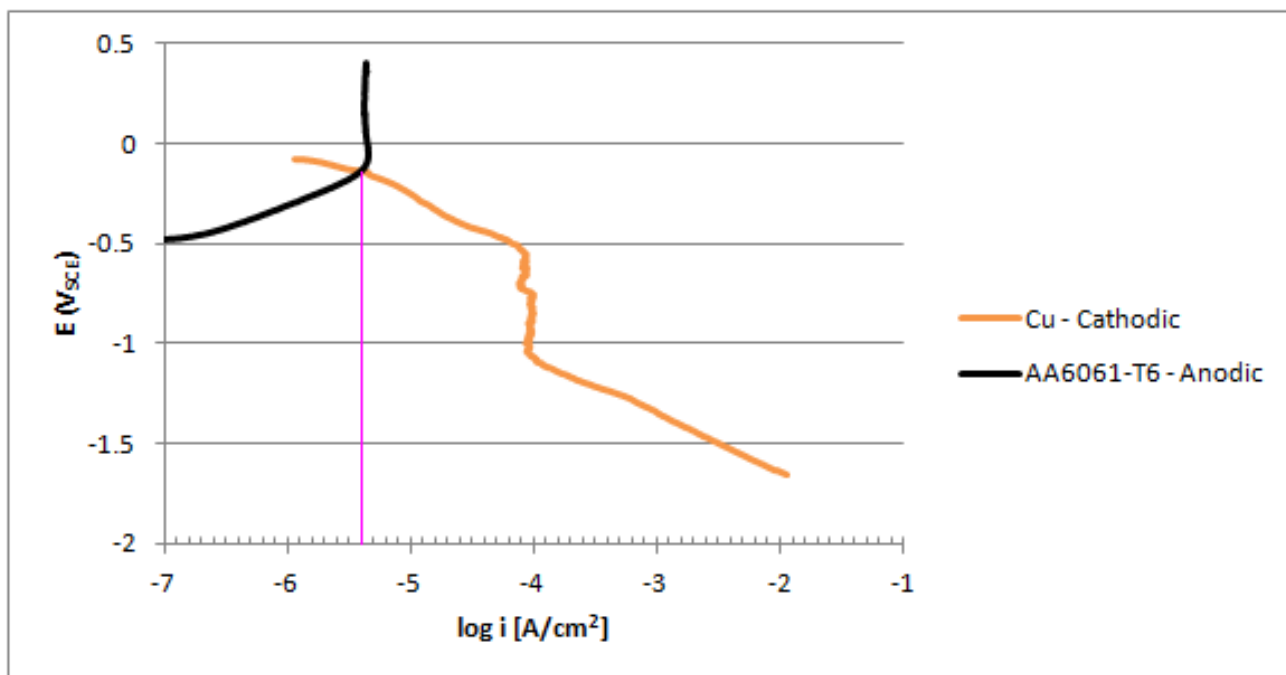


Fig. 10. Cathodic Cu and anodic Al polarization in 0.5 M Na₂SO₄ solution.

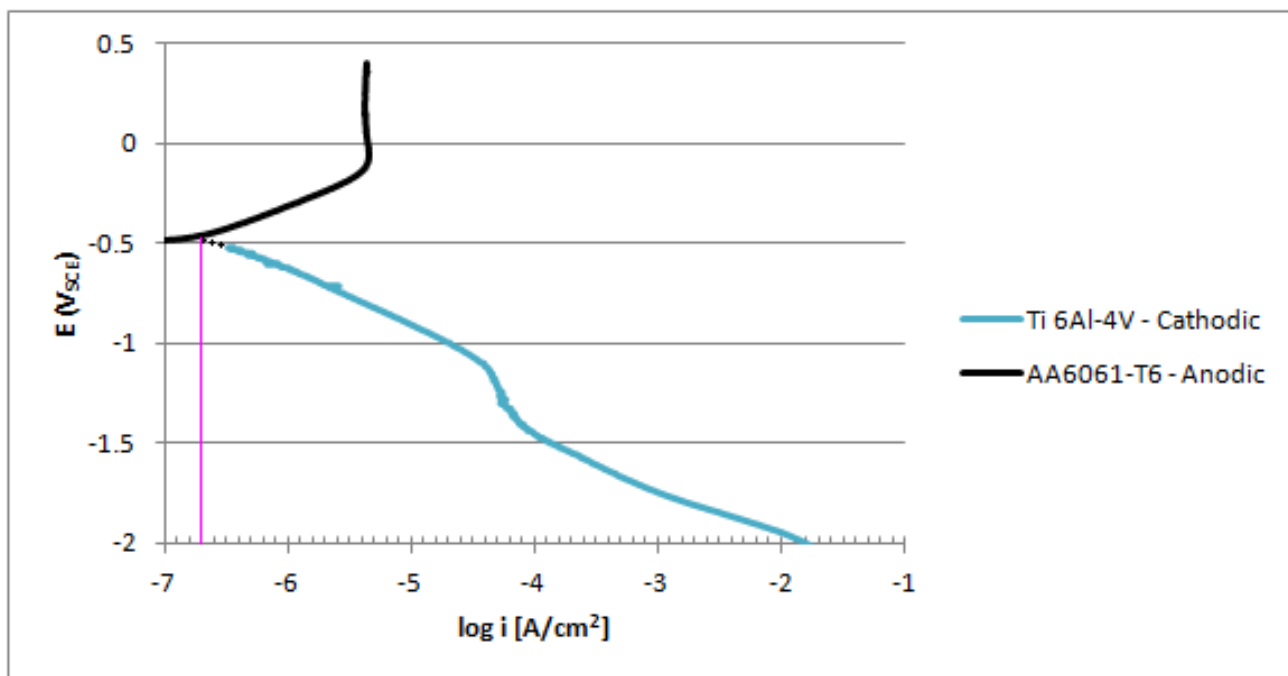


Fig. 11. Cathodic Ti and anodic Al polarization in 0.5 M Na₂SO₄ solution.

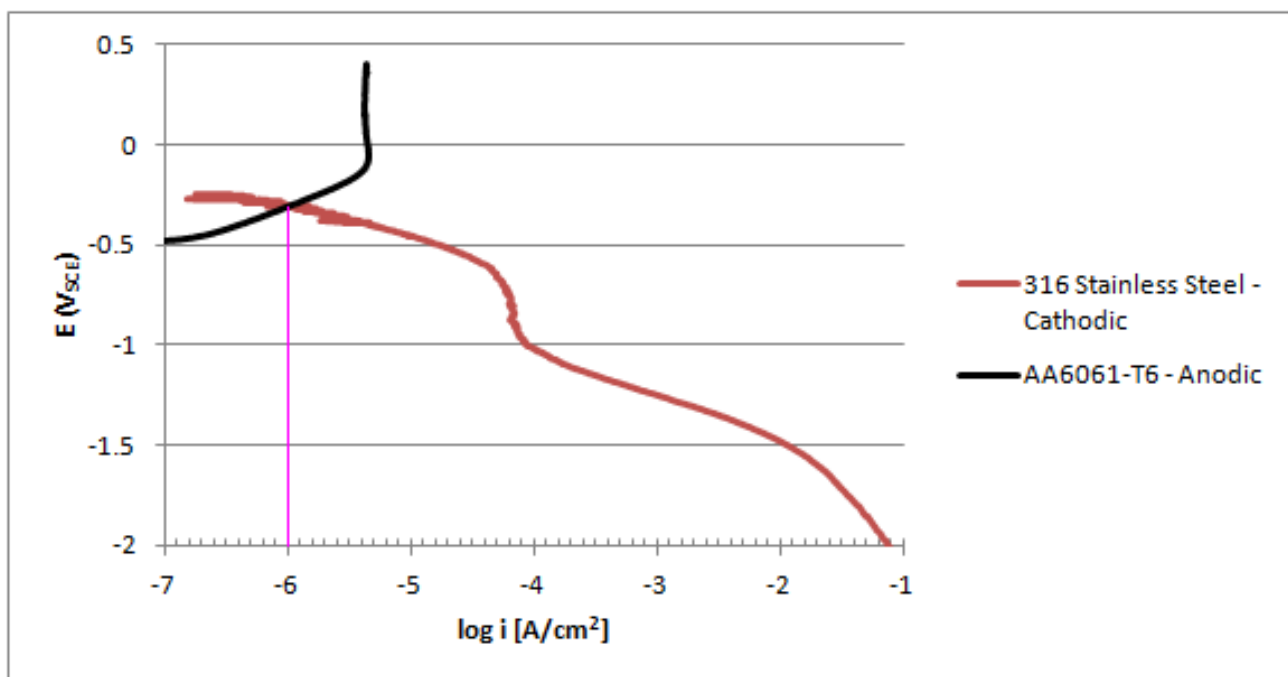


Fig. 12. Cathodic stainless steel and anodic Al polarization in 0.5 M Na₂SO₄ solution.

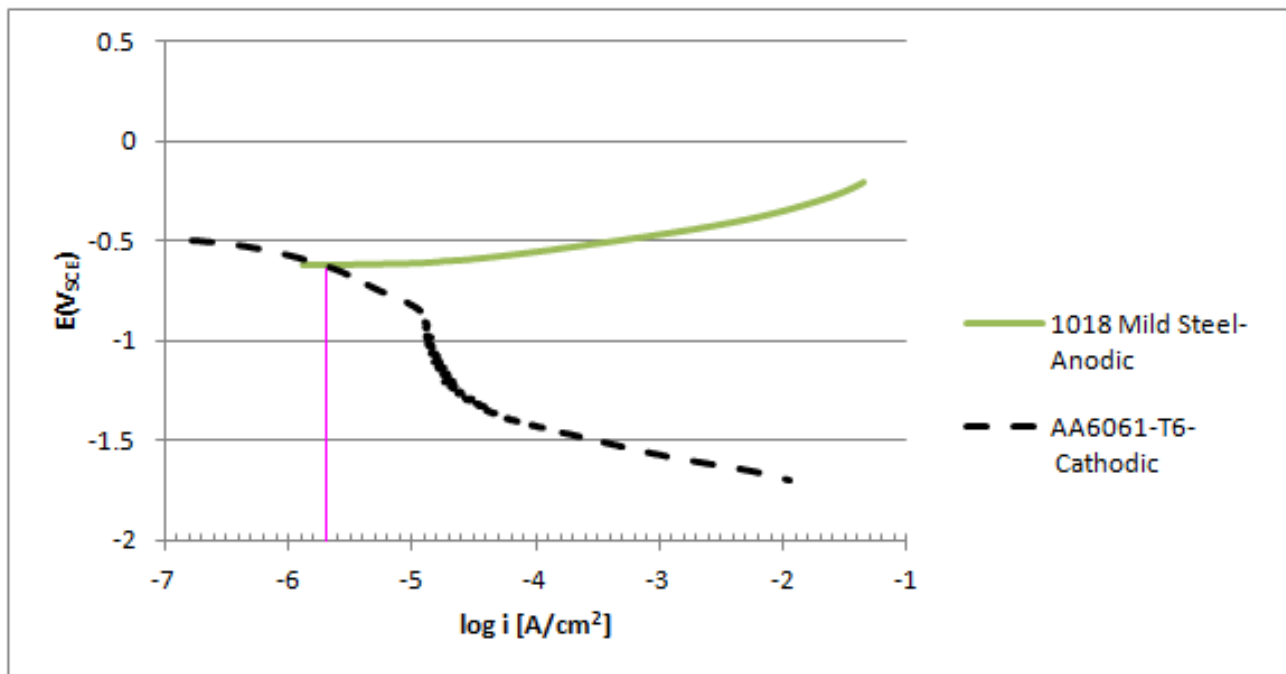


Fig. 13. Cathodic Al and anodic mild steel polarization in 0.5 M Na₂SO₄ solution.

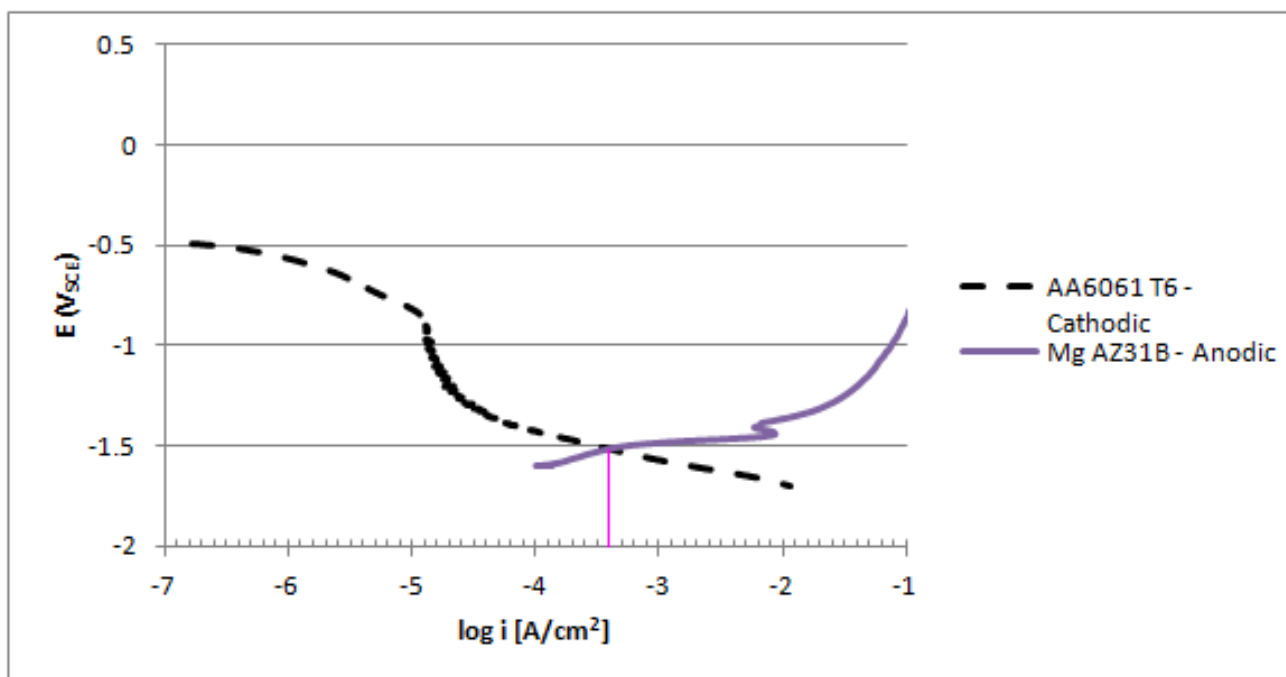


Fig. 14. Cathodic Al and anodic Mg polarization in 0.5 M Na₂SO₄ solution.

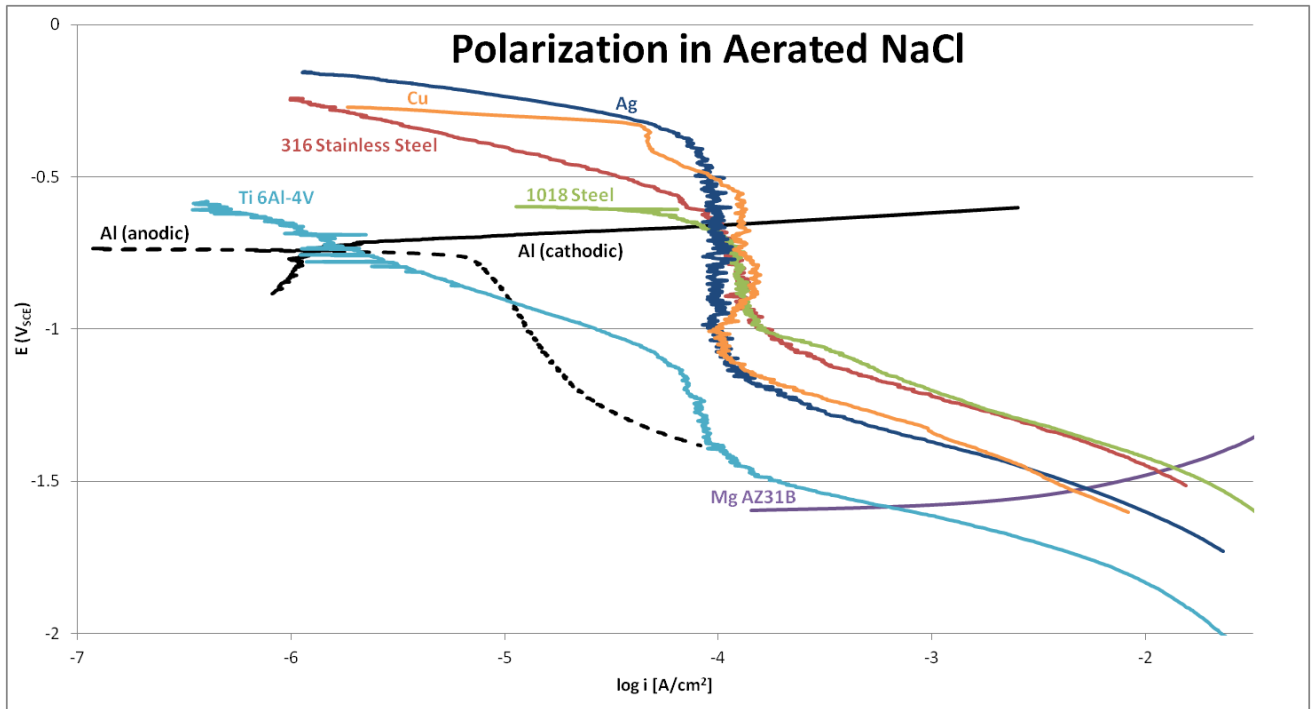


Fig. 15. Overlay of anodic and cathodic polarization curves in 3.15 wt% NaCl solution.

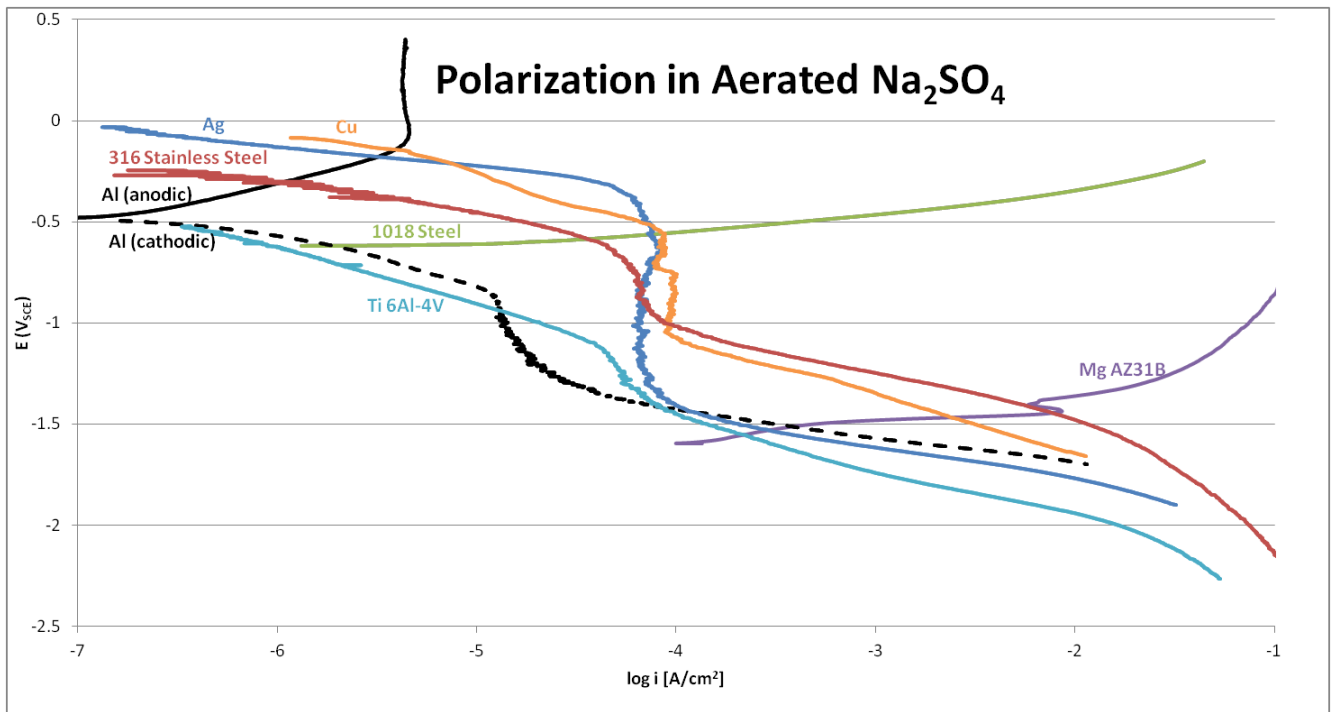


Fig. 16. Overlay of anodic and cathodic polarization curves in 0.5 M Na_2SO_4 solution.

The point of intersection of the anodic and cathodic curve of each metal type represents the galvanic current (i_{galv}), or the contribution of galvanic current to galvanic corrosion of the anode.¹ The extrapolated i_{galv} values for each metal coupled to Al in NaCl solution and Na₂SO₄ solution are listed in Table 3.

Table 3: Extrapolated i_{galv} values.

Metal	$\log i_{galv}$ [A/cm ²] in 3.15 wt% NaCl	$\log i_{galv}$ [A/cm ²] in 0.5 M Na ₂ SO ₄
Ag	-4.0	-5.5
Cu	-3.9	-5.4
Ti	-5.8	-6.7
Stainless Steel	-4.0	-6.0
Mild Steel	-4.1	-5.7*
Mg	-2.5*	-3.4*

*The $\log i_{galv}$ values represent the galvanic contribution of aluminum to these metals, as aluminum is indicated as the cathode when coupled to these metals in the presence of the stated electrolyte.

In the NaCl solution, the anodic Al curve shows a rapid increase in current density at around 10^{-6} A/cm², indicating a breakdown of the passive film on the Al surface. Most cathodic curves experience a sharp decrease in potential around a current density of 10^{-4} A/cm² which is the diffusion-limited oxygen reduction current density in the polarization cell. Oxygen reduction is often the primary cathodic reaction when metals corrode in aerated solutions.² Mg is an exception where the predominant cathodic reaction is hydrogen evolution in both aerated and deaerated solutions. It is around the diffusion-limited oxygen reduction current density that i_{galv} is obtained for Ag, Cu, stainless steel, and mild steel, with a slightly higher current density value for Cu. This may have been due to slight fluctuation in the air sparge rate or more active cathodic sites on the copper versus the other metals. The polarization behavior of the metals indicated the

galvanic corrosion rate is under cathodic control by oxygen reduction when Al (the anode) is galvanically coupled to these metals. However, in the case of Ti, the cathodic curve intersects the anodic Al curve at a much lower current density, indicating a much smaller galvanic contribution when Al is coupled to Ti. The Ti still experiences a slight decrease in potential at 10^{-4} A/cm². The initial current density for the anodic Mg curve is much higher than that of the other metals and increases rapidly, providing a relatively high i_{galv} value for Mg with cathodic Al.

In the Na₂SO₄ solution, a sharp increase in the Al potential indicated that the layer of passivation on the Al was maintained throughout polarization. The passive layer of aluminum is not as susceptible to degradation by sulfate ions as is the case with chloride ions.⁷ Passivation of the Al significantly decreases the i_{galv} value for each metal. For the couples in which Al is the anode, the i_{galv} values for Cu and Ag are the highest with a slightly higher value for Cu, followed by stainless steel, then Ti. The i_{galv} value for Mg coupled to Al is again relatively high compared to that of the other couples.

Chapter 4: Experimental Procedures for Environmental Exposure

4.1. Galvanic couple specimen assembly

Couples were assembled using 2-in. x 1-in. coupons of Ag, Cu, Ti, stainless steel, mild steel, and Mg mechanically coupled to 2-in. x 1-in. Al coupons using non-conductive, glass-reinforced polyurethane fasteners tightened to the maximum working torque of 10 in.-lbs. A non-conductive sheet of G10 fiberglass was inserted between the metals in all couples for which galvanic current was to be measured; couples that were not being measured for galvanic corrosion did not contain the insulating sheet and were included in the experiment in quadruplicate. Non-coupled coupons of each metal were also included in the experiment in quadruplicate. Non-conductive, inert insulators and fasteners were used to mount the coupled and uncoupled metals onto powder-coated aluminum face plates.

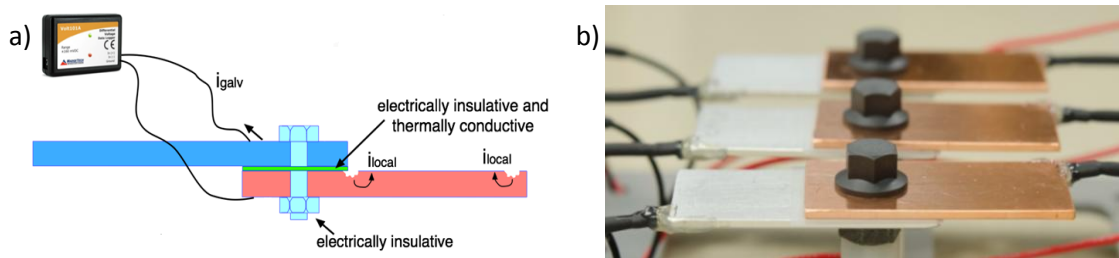


Fig. 17. Assembled galvanic couple a) Schematic b) Assembled and mounted Al-Cu couple pre-environmental exposure

4.2. Support system

The galvanic couples and corresponding uncoupled metals were grouped by metal type and mounted on their designated face plate and position. The face plates were separated by acrylic barriers to prevent cross-contamination and were then mounted onto fiberglass struts (Fig. 19). The entire unit was then placed flat (0-degree angle from the horizontal) onto the test rack.

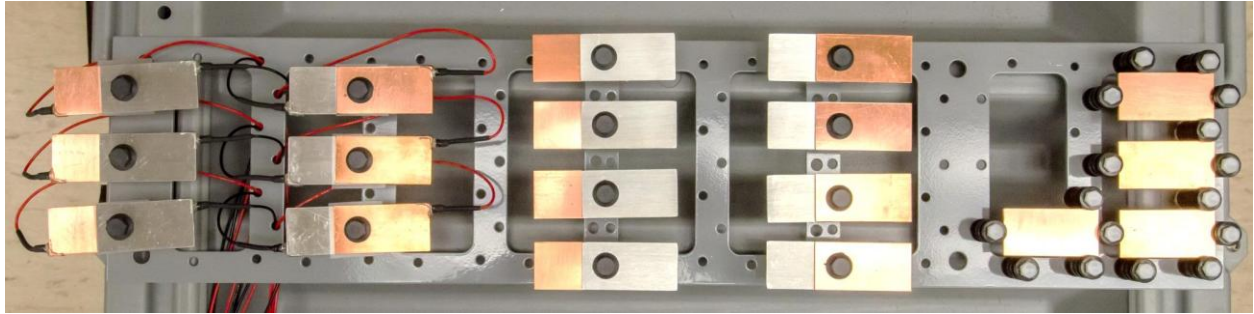


Fig. 18. Face plate containing Al-Cu galvanic couples and uncoupled Cu.

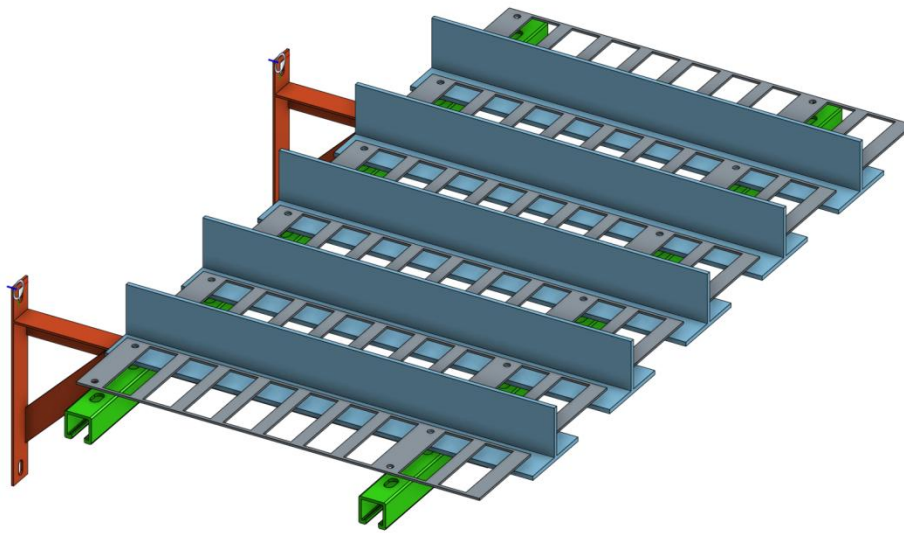


Fig. 19. Illustration of support system.

4.3. Data logger configuration

Galvanic current was measured using differential voltage loggers and resistors. Triplicate couples of each type were connected to either a Madgetech QuadVolt, a Madgetech OctVolt, or a Madgetech Volt101A voltage data logger via TCL 4-wire cables and epoxied weather-resistant connectors. Resistor magnitude was $1\ \Omega$ for the samples in the cyclic corrosion testing chamber (CCTC) and $10\ \Omega$ for the outdoor exposure tests. Data loggers were kept in a water resistant, lockable enclosure fortified with desiccant. With the preparation of an extra set of data loggers

and a color-coded cable joint system, the logger sets were able to be readily exchanged at the test site with minimal data loss to allow for data downloading and logger inspection in the laboratory.

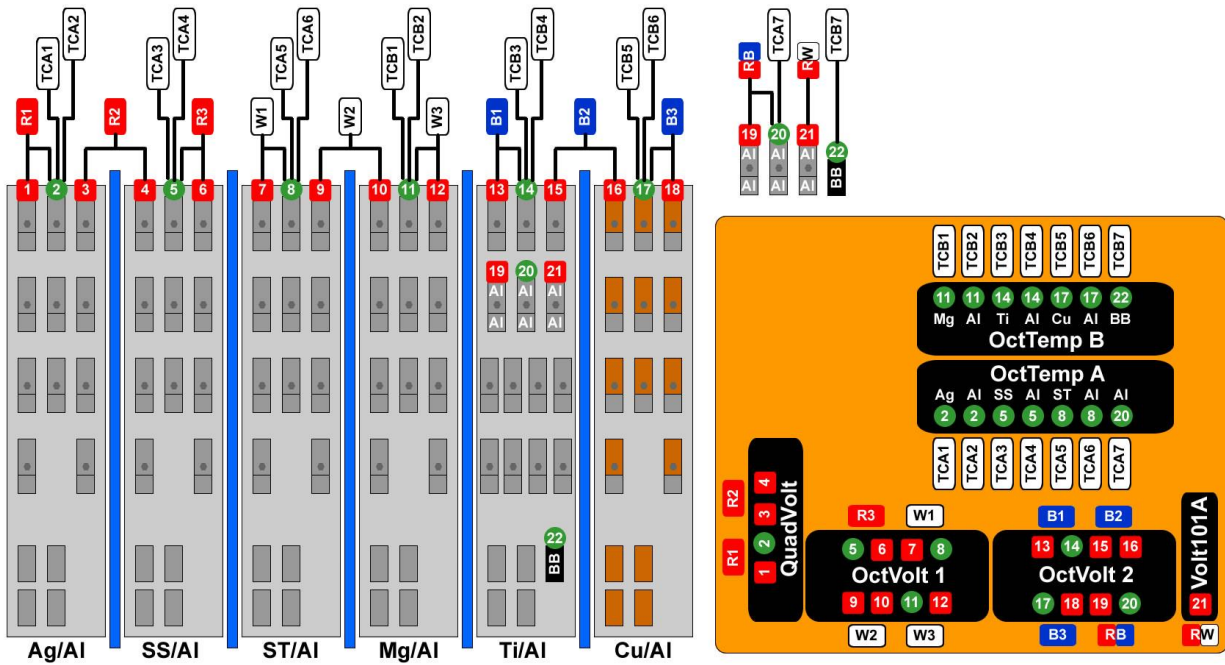


Fig. 20. Wiring schematic of voltage data loggers.

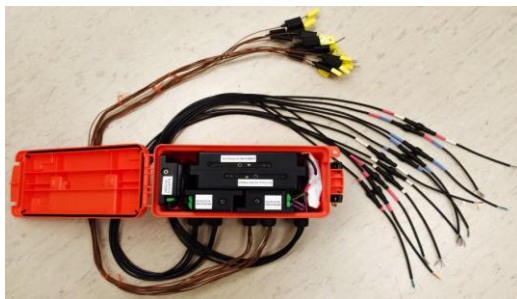


Fig. 21. Top view of enclosed data loggers.



Fig. 22. Color-coded cable joints outside of logger box.

4.4. Specimen exposure

Four sets of experimental galvanic couples and uncoupled metals were assembled and deployed to four different testing sites for environmental exposure. These sites included the CCTC, MCBH, Kilauea, and Lyon Arboretum (Fig. 23).



Fig. 23. Experimental specimens at a) CCTC, b) MCBH, c) Kilauea, d) Lyon Arboretum.

The specimens in the CCTC were subjected to the experimental conditions standardized in the GM-9540P accelerated corrosion test. A single modification was made in the angle of placement of the specimens which was set at 0 degrees from the horizontal. A cycle of the GM-9540P test is 24 hours long and involves a series of salt solution spray containing NaCl, CaCl₂, and NaHCO₃ at room temperature, followed by a period of 100% relative humidity at 49°C, and

finally a dry-off period of high heat at 60°C (Figure 24). The specimens were exposed in the CCTC for 30 cycles. Voltage data was logged every 1 minute and was downloaded roughly once a week throughout the exposure period.

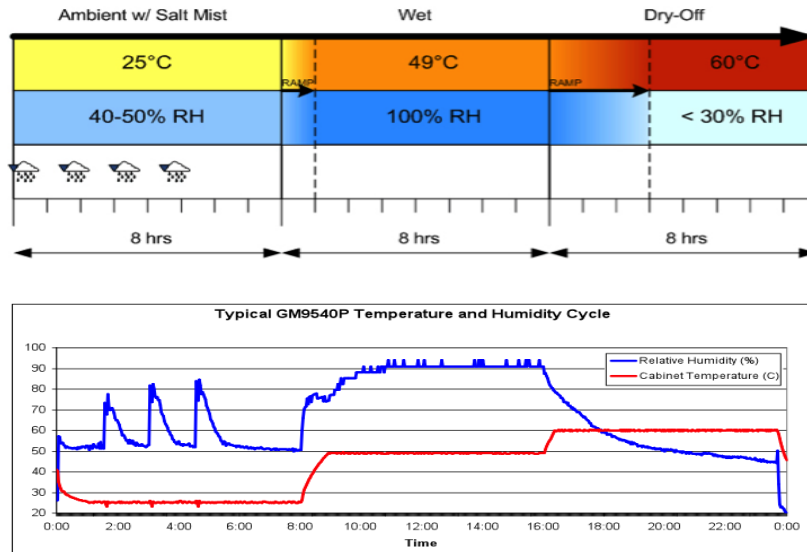
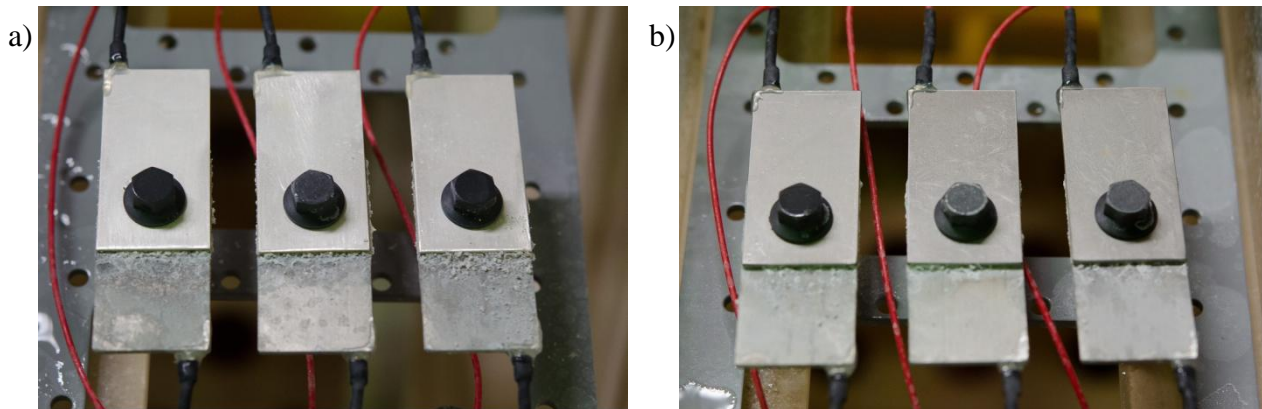


Fig. 24. Environmental conditions of the GM-9540P accelerated corrosion test. Courtesy of Daniel P. Schmidt of Army Research Office.



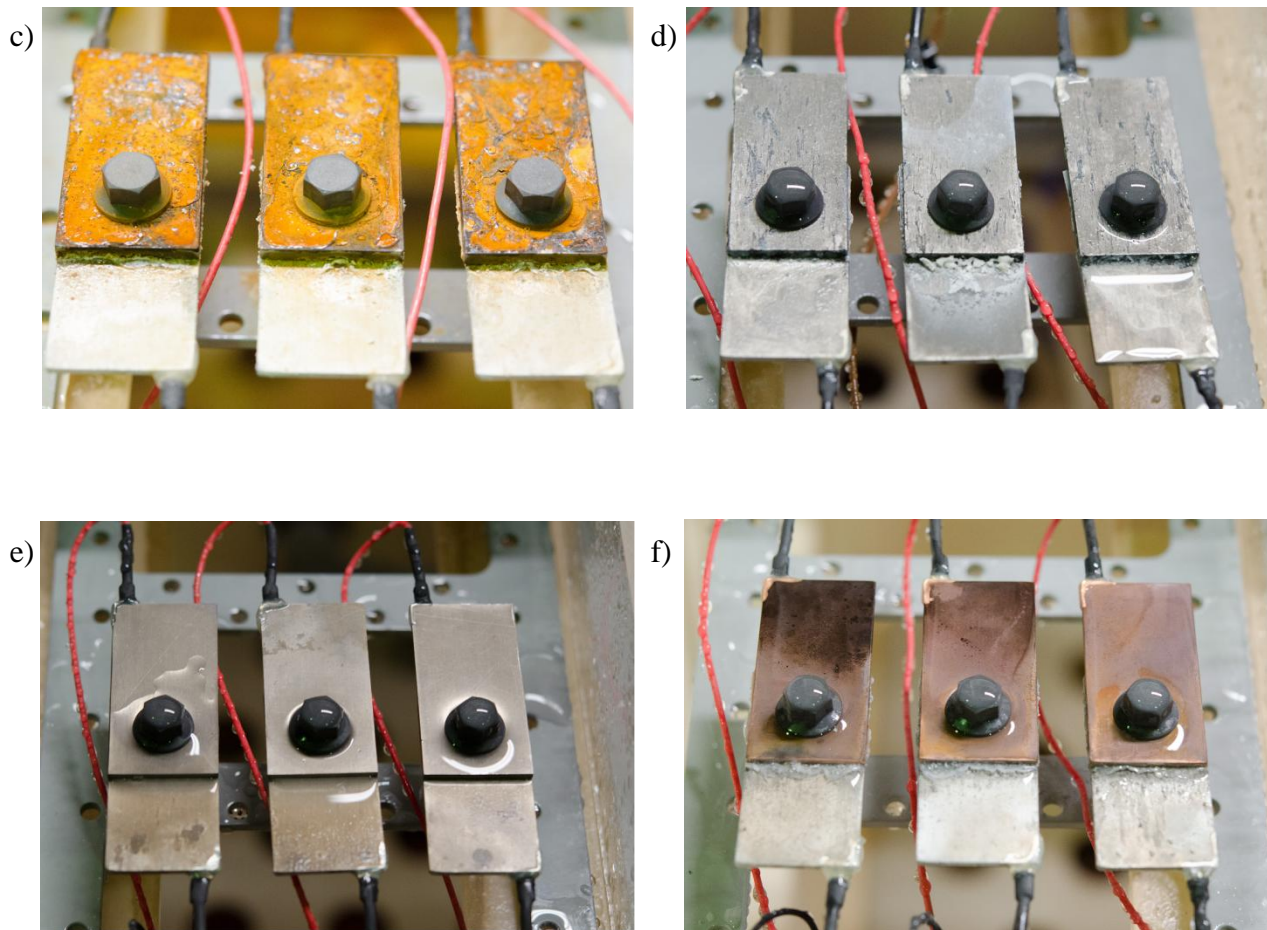


Fig. 25. Galvanic couples following four cycles of the GM-9540P test consisting of a) Al and Ag, b) Al and stainless steel, c) Al and mild steel, d) Al and Mg, e) Al and Ti, and f) Al and Cu.

The outdoor exposure specimens were deployed for a period of 4 months. Voltage data was logged every 5 minutes and was downloaded roughly once a month, wherein the voltage logger box was disconnected and exchanged throughout each outdoor test site. The experimental specimens themselves were undisturbed by laboratory members during each data logger box exchange. Figs. 26-28 show the galvanic couples at each test site following one month exposure.

All specimens were returned to the laboratory and removed from the support mounts following exposure. The couples were disassembled and separated for analysis.

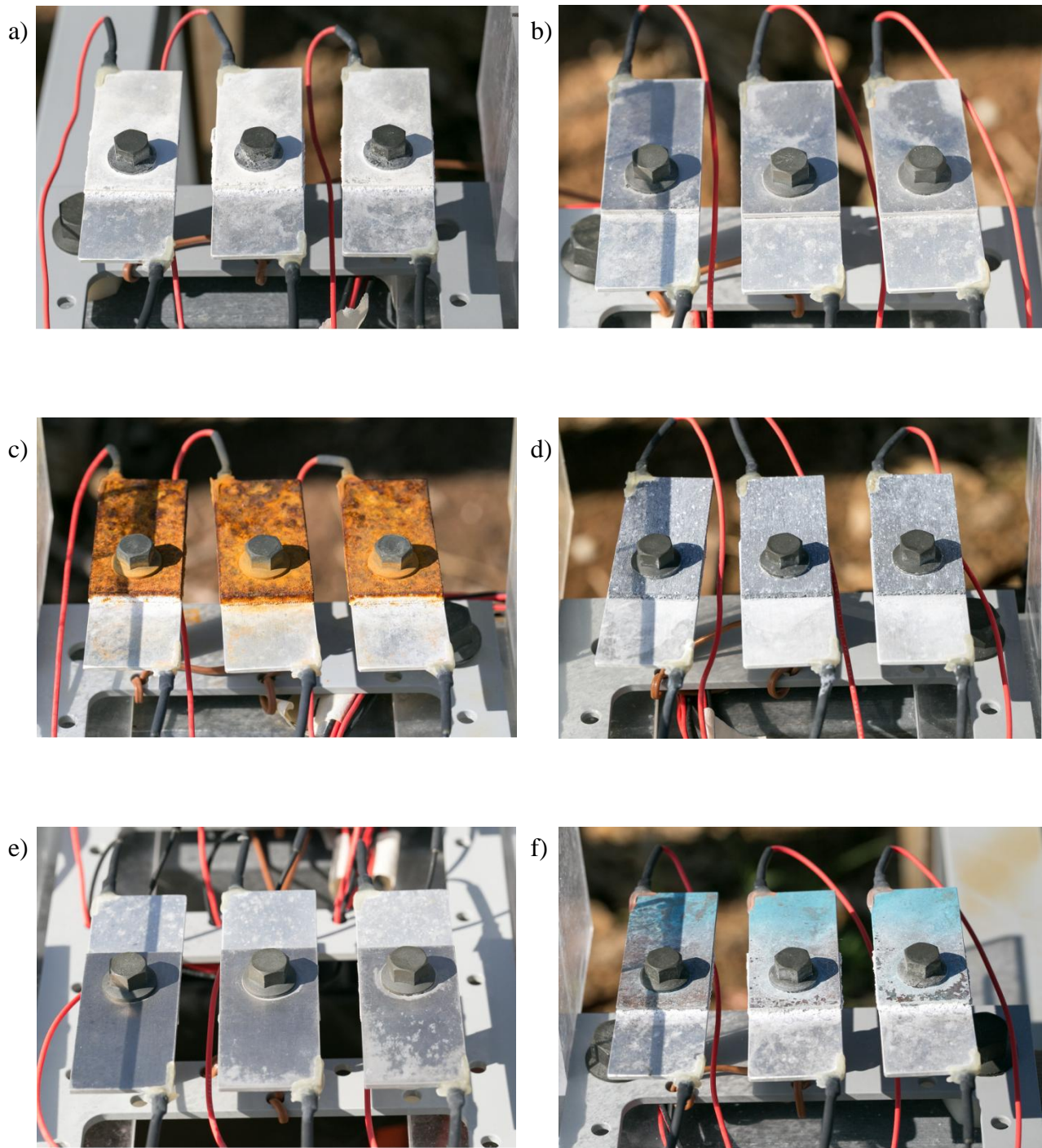


Fig. 26. Galvanic couples after one month of exposure at MCBH consisting of a) Al and Ag, b) Al and stainless steel, c) Al and mild steel, d) Al and Mg, e) Al and Ti, and f) Al and Cu.

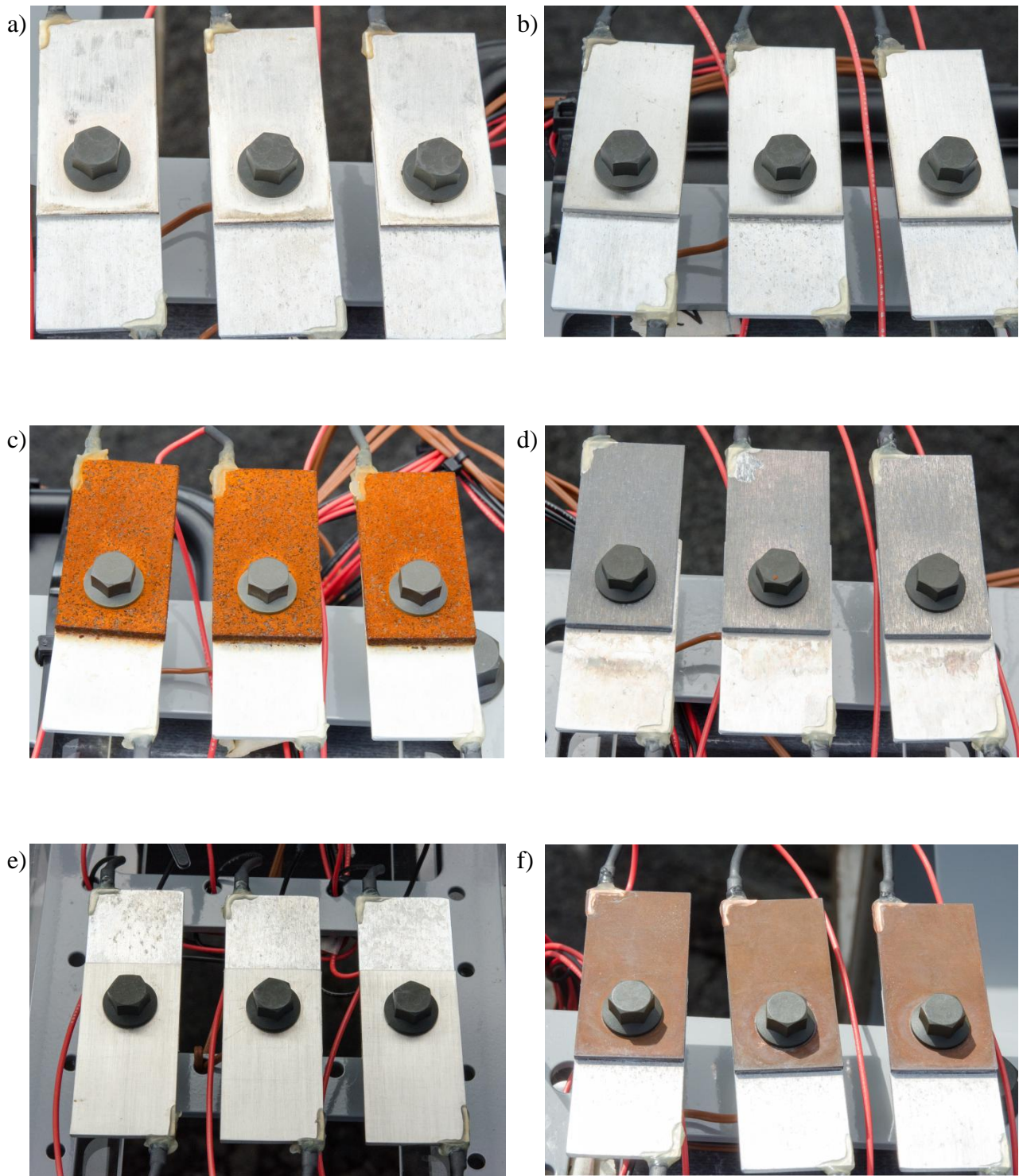


Fig. 27. Galvanic couples after one month of exposure at Kilauea consisting of a) Al and Ag, b) Al and stainless steel, c) Al and mild steel, d) Al and Mg, e) Al and Ti, and f) Al and Cu.

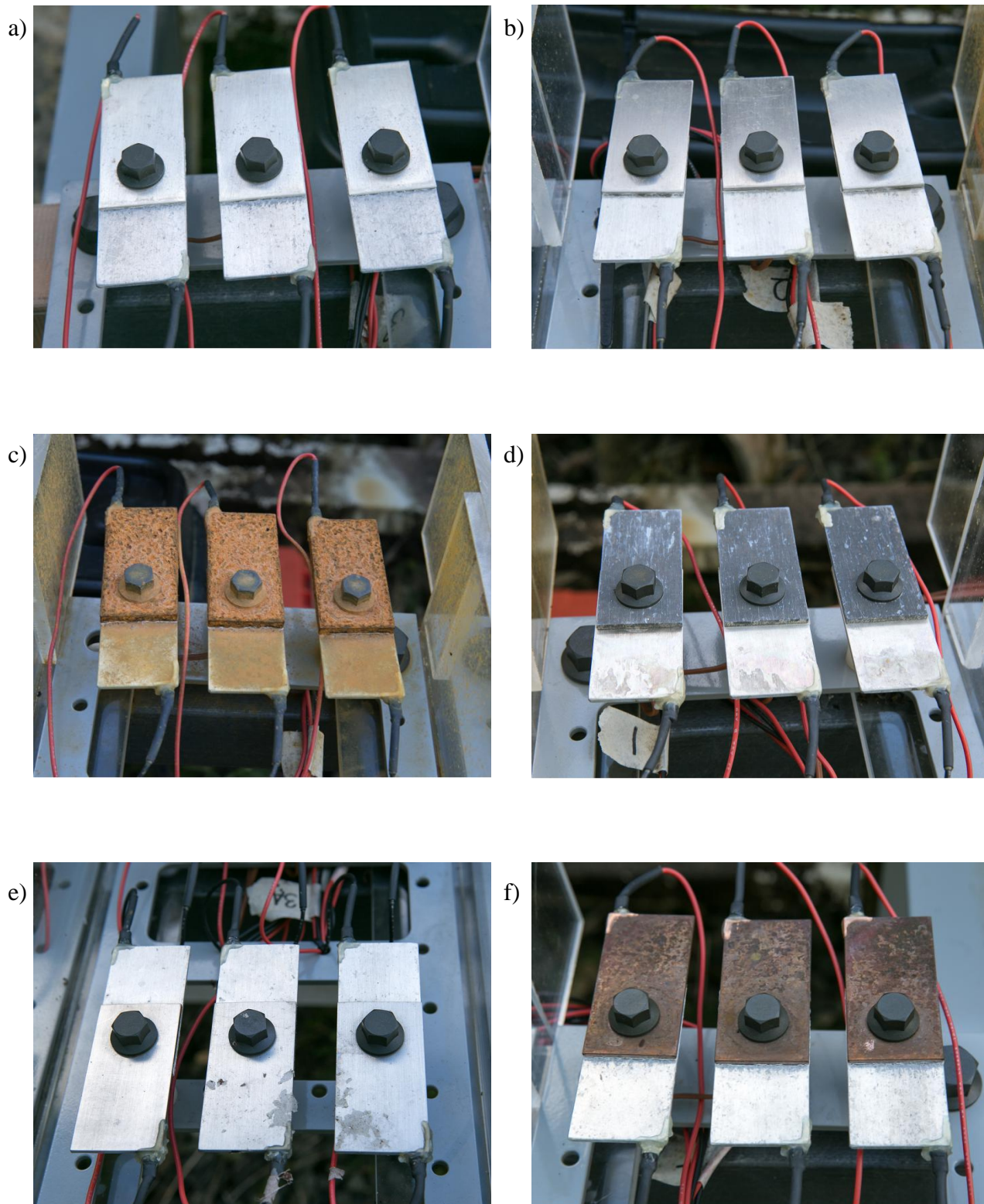


Fig. 28. Galvanic couples after one month of exposure at Lyon Arboretum consisting of a) Al and Ag, b) Al and stainless steel, c) Al and mild steel, d) Al and Mg, e) Al and Ti, and f) Al and Cu.

Chapter 5: Determination of Corrosion Rate

5.1. Penetration rate and mass loss

The corroded Al coupons were subjected to a chemical cleaning procedure for corrosion product removal in order to determine the total mass loss of the specimens. The Al cleaning solution consisted of 2% chromium trioxide and 5% phosphoric acid following International Standard ISO 8407: 1991 (E) C.1.1. Because Mg is anodic to Al in the Al-Mg galvanic couple, the mass loss of Mg was also of interest. The Mg coupons were also subjected to corrosion product removal and cleaned in a solution containing 20% chromium trioxide, 2% barium nitrate, and 1% silver nitrate following the standard ASTM G1 C.5.2 cleaning procedure. The final mass of each cleaned specimen was recorded and subtracted from the initial mass to determine the total mass loss.

The average penetration rate was calculated for the uncoupled Al and each position of coupled Al (i.e. Al-on-top or X-on-top position where X is the corresponding Al-coupled metal) at each exposure site. The penetration rate of the coupled Al were further separated by the set of Al couples with a voltage data logger attached and the set of those without a logger attached. The test samples subjected to exposure in the CCTC included two sets of galvanic couples attached to data loggers in both the Al-on-top and X-on-top orientation; all couples attached to data loggers at the outdoor exposure sites (i.e. MCBH, Lyon Arboretum [LA], and Kilauea [KIL]) were in the X-on-top orientation only. All sites contained sets of galvanic couples without a data logger attached in both orientations. The average penetration rates for each set of exposed Al are listed in Tables 4-9.

Table 4: Average penetration rate of Al coupled to Ag in mm per year.

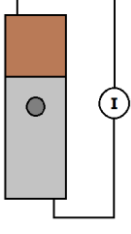
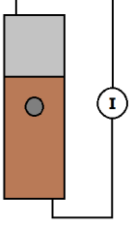
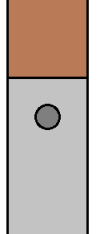
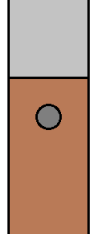
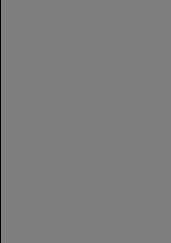
Exposure site	Uncoupled	Coupled with logger		Coupled without logger	
		Al on top	Ag on top	Al on top	Ag on top
CCTC	2.73E-02				
MCBH	6.27E-04		6.42E-02	5.74E-02	4.55E-02
LA	2.13E-04		9.89E-03	2.46E-02	2.16E-02
KIL	8.28E-04		8.57E-03	1.86E-02	1.66E-02

Table 5: Average penetration rate of Al coupled to Cu in mm per year.

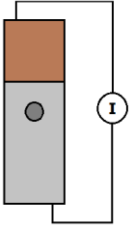
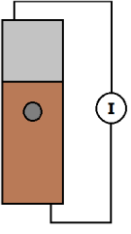
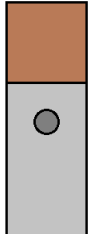
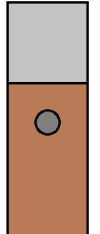
Exposure site	Uncoupled	Coupled with logger		Coupled without logger	
		Al on top	Cu on top	Al on top	Cu on top
CCTC	2.73E-02				
MCBH	6.27E-04		5.52E-02	7.45E-02	6.71E-02
LA	2.13E-04		7.37E-03	2.42E-02	2.05E-02
KIL	8.28E-04		7.19E-03	1.74E-02	1.85E-02

Table 6: Average penetration rate of Al coupled to Ti in mm per year.

Exposure site	Uncoupled	Coupled with logger		Coupled without logger	
		Al on top	Ti on top	Al on top	Ti on top
CCTC	2.73E-02	4.65E-02	4.38E-02	2.91E-02	3.32E-02
MCBH	6.27E-04		1.40E-02	6.20E-03	9.57E-03
LA	2.13E-04		1.76E-03	3.52E-03	1.67E-03
KIL	8.28E-04		1.74E-03	2.71E-03	2.41E-03

Table 7: Average penetration rate of Al coupled to stainless steel in mm per year.

Exposure site	Uncoupled	Coupled with logger		Coupled without logger	
		Al on top	Stainless steel on top	Al on top	Stainless steel on top
CCTC	2.73E-02	2.33E-01	2.63E-01	1.34E-01	8.16E-02
MCBH	6.27E-04		2.04E-02	2.78E-02	2.03E-02
LA	2.13E-04		5.22E-03	7.76E-03	5.61E-03
KIL	8.28E-04		3.77E-03	2.41E-03	2.88E-03

Table 8: Average penetration rate of Al coupled to mild steel in mm per year.

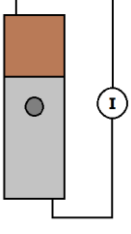
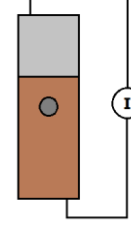
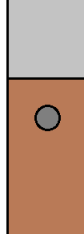
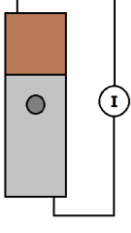
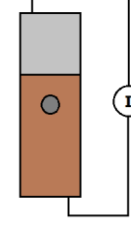
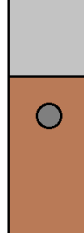
Exposure site	Uncoupled	Coupled with logger		Coupled without logger	
		Al on top	Mild steel on top	Al on top	Mild steel on top
CCTC	2.73E-02				
MCBH	6.27E-04			4.10E-02	5.03E-02
LA	2.13E-04			7.77E-03	1.44E-02
KIL	8.28E-04			1.54E-02	1.18E-02
				2.13E-01	2.33E-01

Table 9: Average penetration rate of Al coupled to Mg in mm per year.

Exposure site	Uncoupled	Coupled with logger		Coupled without logger	
		Al on top	Mg on top	Al on top	Mg on top
CCTC	2.73E-02				
MCBH	6.27E-04			4.81E-03	5.51E-03
LA	2.13E-04			5.91E-04	6.27E-04
KIL	8.28E-04			5.28E-04	4.56E-04
				6.07E-02	7.97E-02

The average penetration rate was also calculated for Al coupons coupled to other Al coupons attached to ammeter loggers. Ideally, no sustained galvanic current should pass between two metals of the same type, thus Al-Al coupons were fabricated in order to obtain baseline data for crevice-induced corrosion in the absence of a galvanic couple. The current data showed that small currents often alternated between positive and negative values. The average penetration rate of the Al coupons in the Al-Al couples compared to the uncoupled Al is listed in Table 10.

Table 10: Average penetration rate of Al coupled to Al in mm per year.

Exposure site	Uncoupled Al	Al coupled to Al
CCTC	2.73E-02	2.63E-02
MCBH	6.27E-04	9.45E-03
LA	2.13E-04	5.97E-04
KIL	8.28E-04	6.78E-04

The average penetration rates for Mg were calculated in a similar manner to those of Al for all test sites. These values are listed in Table 11.

Table 11: Average penetration rate of Mg coupled to Al in mm per year.

Exposure site	Uncoupled	Coupled with logger		Coupled without logger	
		Al on top	Mg on top	Al on top	Mg on top
CCTC	1.93E-02	6.31E-02	7.75E-02	4.49E-02	5.43E-02

MCBH	5.58E-02		9.65E-02	6.88E-02	7.59E-02
LA	3.38E-02		4.14E-02	3.24E-02	3.98E-02
KIL	2.73E-02		3.33E-02	2.29E-02	3.24E-02

In viewing the average penetration rate data, it is apparent that the corrosion rate differed depending on the orientation in which the Al was exposed, even among Al coupled to the same type of metal. In addition to the mass loss percentages, the ratios of average mass loss were calculated between each orientation of exposed Al; the ratios include the coupled Al with logger to the uncoupled Al, the coupled Al without logger to the uncoupled Al, and the coupled Al with logger to the coupled Al without logger. For the latter ratios in which both compared sets are coupled Al, the ratio was calculated with the corresponding Al-on-top or X-on-top orientation. Calculated ratios are listed in Tables 12-17.

Table 12: Average mass loss ratios between different orientations of Al coupled to Ag.

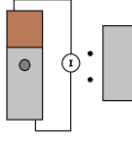
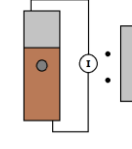
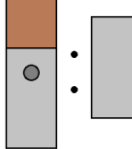
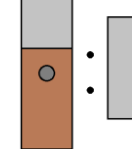
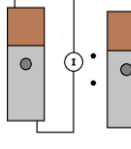
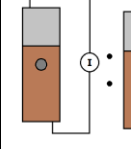
Exposure site	Coupled Al w/ logger to Uncoupled Al		Coupled Al w/o logger to Uncoupled Al		Coupled Al w/ logger to Coupled Al w/o logger	
	Al on top	Ag on top	Al on top	Ag on top	Al on top	Ag on top
CCTC						
	16.3	19.7	11.3	8.73	1.45	2.26
MCBH		102.	92.0	72.7		1.41
LA		46.4	115.	101.		0.459
KIL		10.3	22.4	20.0		0.516

Table 13: Average mass loss ratios between different orientations of Al coupled to Cu.

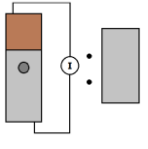
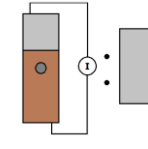
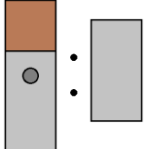
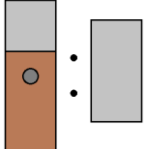
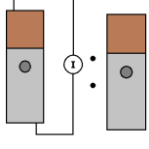
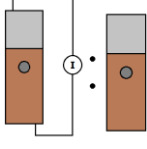
Exposure site	Coupled Al w/ logger to Uncoupled Al		Coupled Al w/o logger to Uncoupled Al		Coupled Al w/ logger to Coupled Al w/o logger	
	Al on top	Cu on top	Al on top	Cu on top	Al on top	Cu on top
						
CCTC	16.7	20.5	16.1	16.0	1.04	1.28
MCBH		88.1	119.	107.		0.823
LA		34.6	114.	96.5		0.356
KIL		8.68	21.0	22.3		0.389

Table 14: Average mass loss ratios different orientations of Al coupled to Ti.

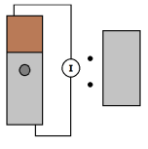
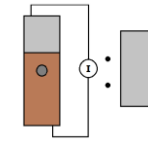
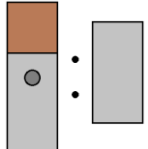
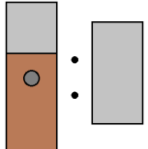
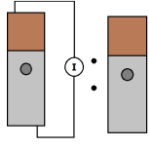
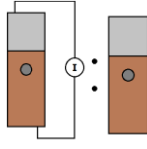
Exposure site	Coupled Al w/ logger to Uncoupled Al		Coupled Al w/o logger to Uncoupled Al		Coupled Al w/ logger to Coupled Al w/o logger	
	Al on top	Ti on top	Al on top	Ti on top	Al on top	Ti on top
						
CCTC	1.70	1.60	1.07	1.22	1.60	1.32
MCBH		22.3	9.89	15.3		1.46
LA		8.28	16.6	7.83		1.06
KIL		2.10	3.28	2.91		0.721

Table 15: Average mass loss ratios between different orientations of Al coupled to stainless steel.

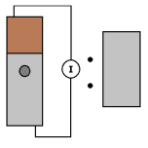
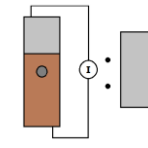
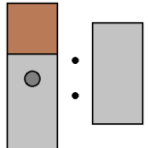
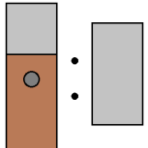
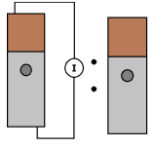
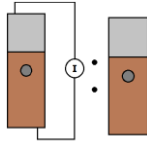
Exposure site	Coupled Al w/ logger to Uncoupled Al		Coupled Al w/o logger to Uncoupled Al		Coupled Al w/ logger to Coupled Al w/o logger	
	Al on top 	Stainless steel on top 	Al on top 	Stainless steel on top 	Al on top 	Stainless steel on top 
CCTC	8.54	9.62	4.91	2.99	1.74	3.22
MCBH		32.6	44.3	32.4		1.01
LA		24.5	36.4	26.3		0.930
KIL		4.55	2.91	3.48		1.31

Table 16: Average mass loss ratios different orientations of Al coupled to mild steel.

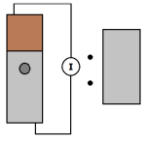
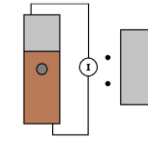
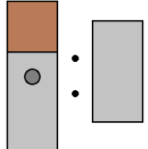
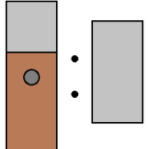
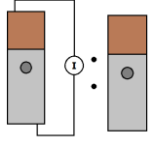
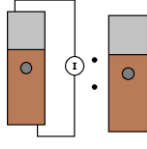
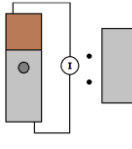
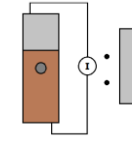
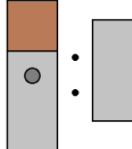
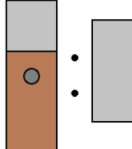
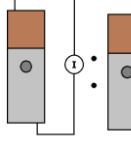
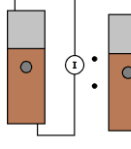
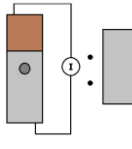
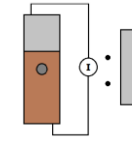
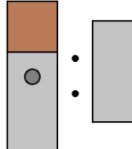
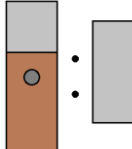
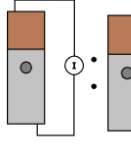
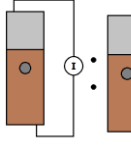
Exposure site	Coupled Al w/ logger to Uncoupled Al		Coupled Al w/o logger to Uncoupled Al		Coupled Al w/ logger to Coupled Al w/o logger	
	Al on top 	Mild steel on top 	Al on top 	Mild steel on top 	Al on top 	Mild steel on top 
CCTC	23.5	15.6	7.79	8.53	3.01	1.83
MCBH		64.1	65.4	80.3		0.798
LA		36.5	74.4	67.8		0.538
KIL		18.7	11.7	14.2		1.31

Table 17: Average mass loss ratios between different orientations of Al coupled to Mg.

Exposure site	Coupled Al w/ logger to Uncoupled Al		Coupled Al w/o logger to Uncoupled Al		Coupled Al w/ logger to Coupled Al w/o logger	
	Al on top	Mg on top	Al on top	Mg on top	Al on top	Mg on top
						
CCTC	2.22	2.92	2.25	5.54	0.988	0.527
MCBH		4.60	7.68	8.79		0.524
LA		2.78	2.67	2.94		0.943
KIL		0.638	0.536	0.551		1.16

The average mass loss ratios for Mg were calculated in a similar manner to those of Al for all test sites. These values are listed in Table 18.

Table 18: Average mass loss ratios between different orientations of Mg coupled to Al.

Exposure site	Coupled Mg w/ logger to Uncoupled Mg		Coupled Mg w/o logger to Uncoupled Mg		Coupled Mg w/ logger to Coupled Mg w/o logger	
	Al on top	Mg on top	Al on top	Mg on top	Al on top	Mg on top
						
CCTC	3.27	4.02	2.33	2.82	1.41	1.43
MCBH		1.73	1.23	1.36		1.27
LA		1.23	0.960	1.18		1.04
KIL		1.22	0.837	1.18		1.03

5.2. Galvanic corrosion rate

Mass loss and penetration rate of the anode due to galvanic current were calculated using (Eq. 2) and (Eq. 3). The voltage values recorded using the data loggers and the known resistance values were used to calculate the summation of galvanic current. The parameters used to calculate mass loss and penetration rate due to galvanic current are as listed in Table 19.

Table 19: Parameters used to calculate mass loss and penetration rate due to galvanic current for each anode.

	Al	Mg
n	3	2
W [g/mole]	27	24.305
α [cm ²]	28.22575	28.22575
ρ [g/cm ³]	2.7	1.74
$t_{\text{exp,CCTC}}$ [days]	30	30
$t_{\text{exp,KIL}}$ [days]	133	133
$t_{\text{exp,LA/MCBH}}$ [days]	135	135
R_{CCTC} [Ω]	1	1
R_{outdoor} [Ω]	10	10

The logged voltage for Al coupled to Ag, Cu, Ti, stainless steel, and mild steel was positive for all test sites and negative when coupled to Mg at all test sites. Thus, the galvanic mass loss δm was calculated for Al coupled to Ag, Cu, Ti, stainless steel, and mild steel; the galvanic mass loss was calculated for Mg coupled to Al. The calculated values for Al mass loss

due to galvanic current and Mg mass loss due to galvanic current are listed in Table 20 and 21, respectively.

Table 20: Calculated penetration rate of Al due to galvanic current.

Metal coupled to Al	Average calculated δm [g]				
	CCTC Al on top	CCTC X on top	MCBH	LA	KIL
Ag	5.75E-02	7.63E-02	4.30E-02	6.31E-03	5.26E-03
Cu	8.47E-02	1.24E-01	2.06E-02	5.91E-03	4.26E-03
Ti	3.77E-03	4.36E-03	1.65E-03	4.39E-04	3.94E-04
Stainless steel	2.49E-02	2.77E-02	5.29E-03	2.14E-03	1.33E-03
Mild steel	9.59E-02	5.40E-02	1.39E-02	6.18E-03	5.20E-03

Table 21: Calculated penetration rate of Mg due to galvanic current.

Metal coupled to Mg	Average calculated δm [g]				
	CCTC Al on top	CCTC Mg on top	MCBH	LA	KIL
Al	6.67E-03	1.86E-02	9.69E-03	5.27E-03	3.81E-03

Penetration rate was calculated using the calculated δm values. The average penetration rates for Al in each couple types and for Mg coupled to Al are listed in Tables 22 and 23, respectively.

Table 22: Calculated penetration rate of Al due to galvanic current.

Metal coupled to Al	Average calculated PR [mm/year]				
	CCTC Al on top	CCTC X on top	MCBH	LA	KIL
Ag	8.72E-02	1.16E-01	1.53E-02	2.59E-03	1.92E-03
Cu	1.28E-01	1.87E-01	7.33E-03	2.10E-03	1.56E-03
Ti	5.72E-03	6.60E-03	5.88E-04	1.56E-04	1.44E-04
Stainless steel	3.77E-02	4.19E-02	1.88E-03	7.61E-04	4.87E-04
Mild steel	1.45E-01	8.17E-02	6.42E-03	2.20E-03	1.90E-03

Table 23: Calculated penetration rate of Mg due to galvanic current.

Metal coupled to Mg	Average calculated PR [mm/year]				
	CCTC Al on top	CCTC Mg on top	MCBH	LA	KIL
Al	1.57E-02	4.37E-02	5.35E-03	2.91E-03	2.16E-03

In order to quantify the galvanic corrosion rate in terms of the total corrosion rate, the penetration rate due to galvanic current was calculated as a percentage of the total mass loss of the coupon post-exposure; in other words, this value is the contribution of galvanic corrosion to total corrosion. These values are listed in Table 24 and 25 for Al corrosion and Mg corrosion, respectively.

Table 24: Percent of total Al corrosion due to calculated galvanic corrosion.

Metal coupled to Al	Average % of total corrosion due to galvanic corrosion				
	CCTC Al on top	CCTC X on top	MCBH	LA	KIL
Ag	19.5%	21.5%	23.8%	26.2%	22.4%
Cu	28.2%	33.5%	13.3%	28.5%	21.7%
Ti	12.3%	15.1%	4.21%	8.85%	8.26%
Stainless steel	16.2%	16.0%	9.22%	14.6%	12.9%
Mild steel	22.7%	19.2%	16.0%	28.3%	12.3%

Table 25: Percent of total Mg corrosion due to calculated galvanic corrosion.

Metal coupled to Mg	Average % of total corrosion due to galvanic corrosion				
	CCTC Al on top	CCTC Mg on top	MCBH	LA	KIL
Al	24.8%	56.5%	5.54%	7.02%	6.48%

5.3. Discussion of corrosion rate

Average penetration rate was nearly universally higher for samples exposed in the CCTC. The direct and regular administration of the salt spray to the test specimens in the CCTC was likely the cause of the vastly accelerated corrosion, and was not a factor present in the outdoor test sites which relied on uncontrolled environmental conditions. The environment in which most couples corroded at the second highest rate was at MCBH. The marine environment mimics the accelerated corrosion test performed in the CCTC most closely due to the presence of atmospheric chlorides and other salts found in seawater and the surrounding ocean front. In general, the couples experienced the third highest amount of corrosion in the rainforest environment at Lyon Arboretum, followed lastly by the volcanic environment at Kilauea. The combination of regular rainfall and high humidity at Lyon Arboretum likely contributed to the higher corrosion rate of Al than at Kilauea; however, both sites produced relatively low corrosion rates than the Al specimens in the CCTC and at MCBH.

The total corrosion was generally highest in Al when coupled to either Ag or Cu, with slightly more corrosion when coupled to Ag at the CCTC and MCBH sites, and roughly the same amount of corrosion when coupled to either Ag or Cu at the Lyon Arboretum and Kilauea sites. The next most corroded set of Al is the Al which was coupled to mild steel, followed by stainless steel, then Ti, and lastly Mg. Although stainless steel and Ti are both passivating metals, Al when coupled to stainless steel corroded two to three times the amount as those coupled to Ti at every test site except for Kilauea, where the Al only corroded slightly higher when coupled to stainless steel than to Ti. Notable exceptions to the stated order of corrosion by coupled metal are the Al samples coupled to either mild steel or Mg in the CCTC. The Al coupled to mild steel and attached to data loggers in the Al-on-top orientation had a higher mass loss percentage than the Al coupled to Ag and Cu in the same orientation. Additionally, all Al samples coupled to Mg had

a higher mass loss percentage than the Al coupled to Ti, which for the other test sites showed a higher corrosion rate than those coupled to Mg. A possible explanation for the increased corrosion in Al coupled to mild steel and Mg is their location in the CCTC—these particular specimens were positioned adjacent to each other and directly under a nozzle in which the salt spray was deployed; thus, these particular specimens likely received a larger amount of salt spray than other specimens in the chamber leading to further accelerated corrosion.

The total corrosion percentage of the uncoupled Al at all outdoor test sites was minimal at less than 0.05%, thus the difference in the average mass loss between all uncoupled aluminum exposed in the outdoor test sites is taken to be negligible. However, the average mass loss percentage of uncoupled Al in the CCTC was much higher than in the outdoor sites at 0.316%. This is likely again due to the direct administration of salt spray to the Al, which subjects the passive layer on the Al to attack, lowering the passivity and increasing corrosion rate. In the outdoor field exposure, the airborne ions were insufficient to appreciably degrade the passive layer on the uncoupled Al as compared those exposed in the CCTC.

Amount of corrosion was relatively equal in the Al coupled to another Al coupon compared to the uncoupled Al, with one exception in the Al coupled to Al at MCBH which corroded at a considerably higher rate (i.e., 15.1 times higher) than the uncoupled Al at the same site. Because both metals in the couple were of the same type, this single increase in corrosion cannot be attributed to galvanic corrosion. One possible explanation could be the presence of a crevice in the Al coupled to Al—the interface between the Al coupons creates an anoxic environment wherein crevice corrosion may occur leading to breakdown of the passive layer and propagation of the corrosion by chloride ion attack.

The Mg specimens coupled to Al generally corroded at a higher rate at each site than the uncoupled Mg, except in the case of Lyon Arboretum and Kilauea for the specimens in the Al-on-top orientation where corrosion was actually less when coupled than uncoupled; these exceptions were likely due to these specimens' position in which protection of half the top surface of the Mg coupon was lent by the Al coupon. Interestingly, the Mg experienced more corrosion overall at MCBH than in the CCTC. A possible explanation for this is that since Mg does not have the passivating ability as Al does, the chlorides present in the atmosphere at MCBH initiated corrosion of Mg immediately and was sustained for the four-month duration of exposure. Since the chloride concentration at MCBH is so high, the Mg specimens never dry out due to the hygroscopic properties of the chloride deposits. In the CCTC, the specimens are in the dry-cycle for 1/3 of the exposure time. Also, since Mg corrodes by hydrogen evolution rather than oxygen reduction, the second phase of the GM-9540P test that induces high diffusion-limited oxygen reduction rates due to the formation of a thin electrolyte layer at 100% RH does not enhance the rate of Mg corrosion.

The mass loss ratios highlight the differences in Al corrosion depending on the manner in which it was exposed. Al corrosion was considerably higher when coupled to another metal versus the uncoupled Al, with the lowest ratios ranging from 1.07-20.5 times the corrosion in the CCTC and the highest ratios ranging from 15.3-119 times the corrosion at MCBH. The low ratios from the Al samples in the CCTC may again be attributed to the higher corrosion overall of the uncoupled Al in the CCTC compared to the other sites. The only scenario in which the Al ratio was lower than one for the coupled Al to the uncoupled Al was in coupling with Mg at Kilauea. In these coupled samples, corrosion rate actually decreased compared to the uncoupled

Al, suggesting that the Al coupons not only retained their passive layer but were afforded cathodic protection from Mg.

The ratios between coupled Al with the logger attached to the coupled Al without the logger attached were calculated due to the presence of the electrically insulating sheet between the metals in the couples attached to the logger. There was no noticeable trend in these ratios across the Al couples corresponding to each metal; however, for the Ag-Al and Cu-Al couples at Lyon Arboretum and Kilauea, the Al without the logger attached corroded at a higher rate than the Al with the logger attached. These two sites yielded the lowest corrosion rates, yet the highest amount of corrosion that occurred at these sites was for the Al specimens in direct contact with the noble active metals.

The ratios for Mg are less dramatic than those of Al. The general trend was that coupled Mg corroded more than uncoupled Mg with some exceptions in the couples where Al was positioned on top of the Mg in the less corrosive environments. The ratio of coupled Mg with a logger attached to coupled Mg without a logger showed that more Mg corrosion occurred when attached to a logger and in direct contact with the Al at the CCTC and MCBH sites, and close to equal at Lyon Arboretum and Kilauea. For the Mg samples in direct contact with the Al, corrosion products in the interface can electrically decouple the Mg from the Al and break the galvanic couple, which is likely more pronounced in the CCTC and at MCBH where corrosion rates were higher. The samples connected to the logger are electrically connected through the wire leads and hence, the galvanic couple cannot be broken for the entire exposure period.

The mass loss data and ratios clearly display that Al in a galvanic couple corrodes more than uncoupled Al, and similarly with Mg in a couple versus uncoupled. However, the contribution of galvanic current to corrosion was a small fraction in most cases to the total

corrosion of the specimen. With the exception of one set of Al coupled to Cu in the CCTC, all calculated galvanic components of corrosion were less than 30% of the total corrosion that was determined by mass loss. Furthermore, for all Al coupled to Ti or stainless steel, the galvanic component made up less than 20% of the total corrosion. Thus, the total corrosion could not have been quantified using the calculated mass loss due to the galvanic current in addition to the amount of local corrosion on the uncoupled Al. As previously stated, crevice corrosion could account for the increase in Al corrosion when coupled to another metal. Another explanation is the local contamination of the Al by the coupled metal—ions from the cathodic metal may transfer to the surface of the Al and create local cathodic sites which would induce corrosion. These processes may lead to accelerated corrosion wherein the alloying elements of the Al may be exposed, creating cathodic sites due to its own composition. In addition, the separation of the cathode and anode can lead to enhanced alkalinity on the cathodic metal and enhanced acidity on and chloride migration to the anodic metal, leading to accelerated corrosion.

The calculated galvanic contribution to total Mg corrosion was considerably higher in the CCTC than in the outdoor field sites, with 24.8% and 56.5% of total corrosion due to galvanic current in the CCTC and less than 8% contribution for all outdoor sites. Accordingly, in the outdoor field sites there was no extreme difference in corrosion of Mg in a couple versus uncoupled Mg, whereas the galvanically-coupled Mg in the CCTC corroded between two to four times as much as the uncoupled Mg depending on its orientation. Thus, the discrepancy in the contribution of galvanic current may be due to the samples in the CCTC being in continuous electrical contact throughout the one-month exposure period; whereas, in the four-month outdoor exposure period, contact between the two metals was possibly weakly maintained due to severe corrosion over time.

Chapter 6: Surface Analysis

6.1. Scanning electron microscopy and energy-dispersive X-ray analysis

An Al coupon from each type of couple was examined by scanning electron microscopy (SEM) using a Hitachi S-4800 Field Emission Scanning Electron Microscope and energy-dispersive X-ray analysis (EDXA) using Oxford INCA software for corrosion morphology and corrosion product composition analysis. The analyzed Al was taken from the set of couples in the X-on-top orientation. An uncoupled Al sample from each test site was also analyzed. Specimens were analyzed with the corrosion product and environmental products intact and were not subjected to the cleaning procedure discussed in Section 5.1.

6.1.1. Test specimens at Marine Corps Base Hawaii

The uncoupled Al was analyzed first in order to obtain the composition of the environmental products present on the surface of the Al samples. A micrograph of a region on the surface of an uncoupled Al coupon at MCBH was taken (Fig. 29). A subsection containing a pit shown in Fig. 29 was magnified for further analysis.

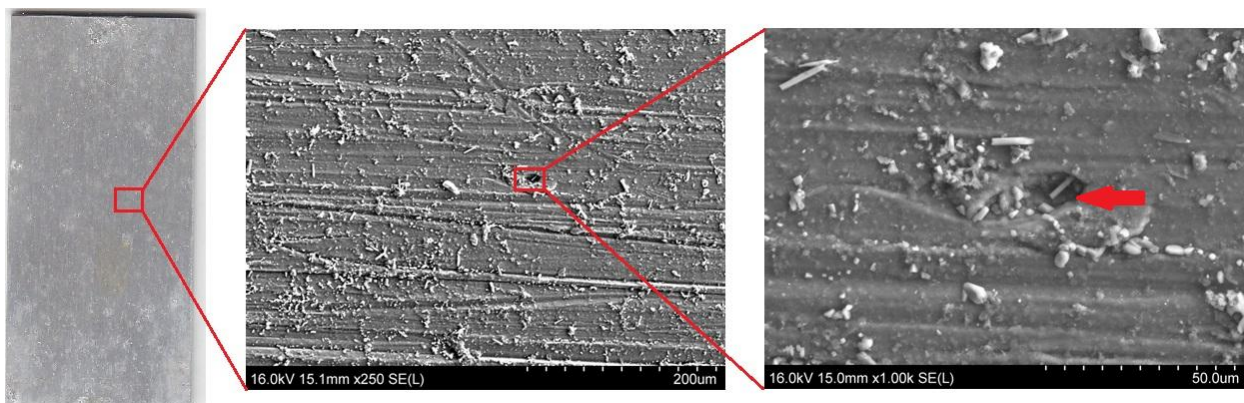


Fig. 29. SEM of uncoupled Al exposed at MCBH.

The corresponding composition for the entire region of the initial micrograph shown in Fig. 29 (left) is listed in Table 25. Pointwise composition analysis was performed in the magnified pit shown in Fig. 29 (right); elemental composition of the pit is also listed in Table 26.

Table 26: Elemental composition of regions shown in Fig. 29.

Element		Al	O	C	Mg	Cl	Na	S	Si	Fe	K	Ca
Atomic %	Region	43.4	41.2	7.37	2.65	2.49	1.25	0.71	0.46	0.20	0.12	0.11
	Pit	78.5	13.8		2.20	2.79	0.40	1.72				0.64

For the pit, the high percentage of aluminum compared to the relatively low percentage of oxygen indicates a decreased presence of aluminum oxide corrosion product, which is likely due to the acidification inside of the pit where the oxide is not stable. Also present are chlorides and other elements typically found in seawater.¹⁷ The significantly higher concentration of Cl compared to Na indicated that chloride ions migrated into the pit. The high amount of magnesium in the pit and full region compared to the other sea water elements could be attributed both as an alloying element of Al and from the environment. In addition to the elements found in the analysis of the pit, carbon, silicon, iron, and potassium were also present in the full region. In addition, an increased presence of oxygen was found in the full region compared to the pit region. This increase along with the presence of carbon in the full region suggests the presence of aluminum oxide corrosion product and carbonates, a common compound found in a marine environment. Potassium is also a common element in sea water. Silicon and iron are alloying elements of Al which may form Al-Fe-Si inclusions in aluminum alloys containing these elements.¹⁸

As discussed in Section 5.2, the Al coupled to the Ag in the X-on-top orientation corroded 72.7 times that of uncoupled Al at MCBH. A typical region of the Al surface outside of the Al-Ag interface, i.e. not covered by the Ag coupon, is shown in Fig. 30.

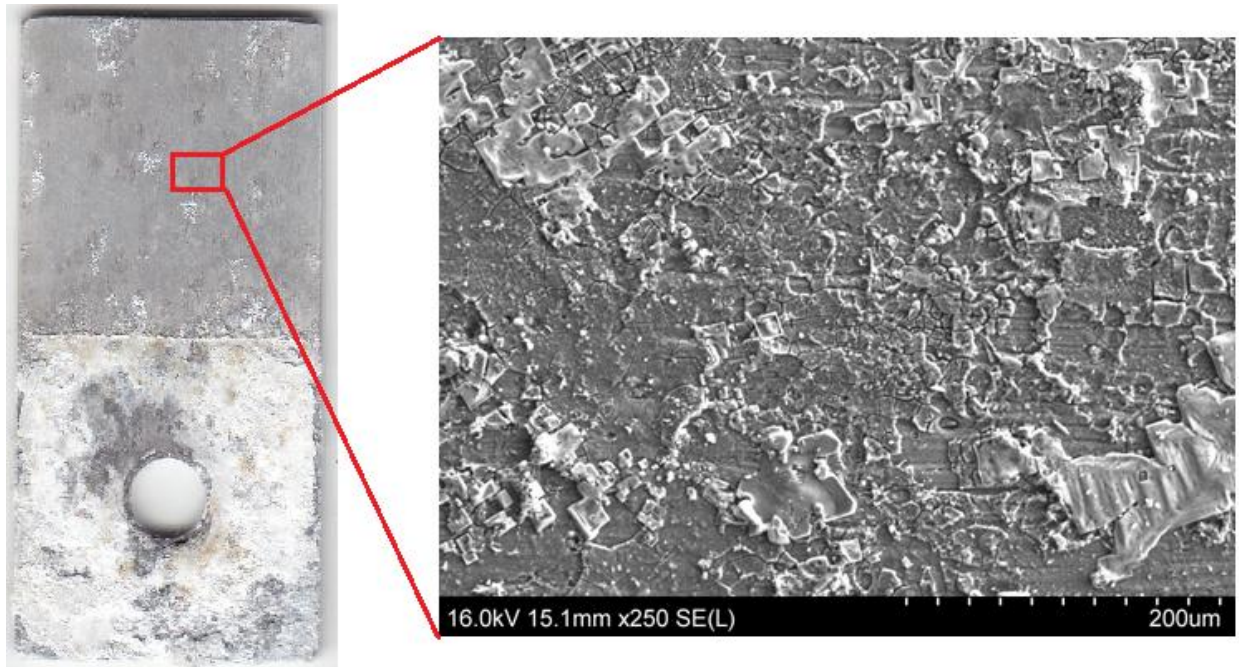


Fig. 30. SEM of uncovered region of Al coupled to Ag exposed at MCBH.

Analysis at the interface between the covered and uncovered area of Al was performed on either side (Fig. 31). The elemental compositions of the uncovered region and the covered region are shown in Table 27.

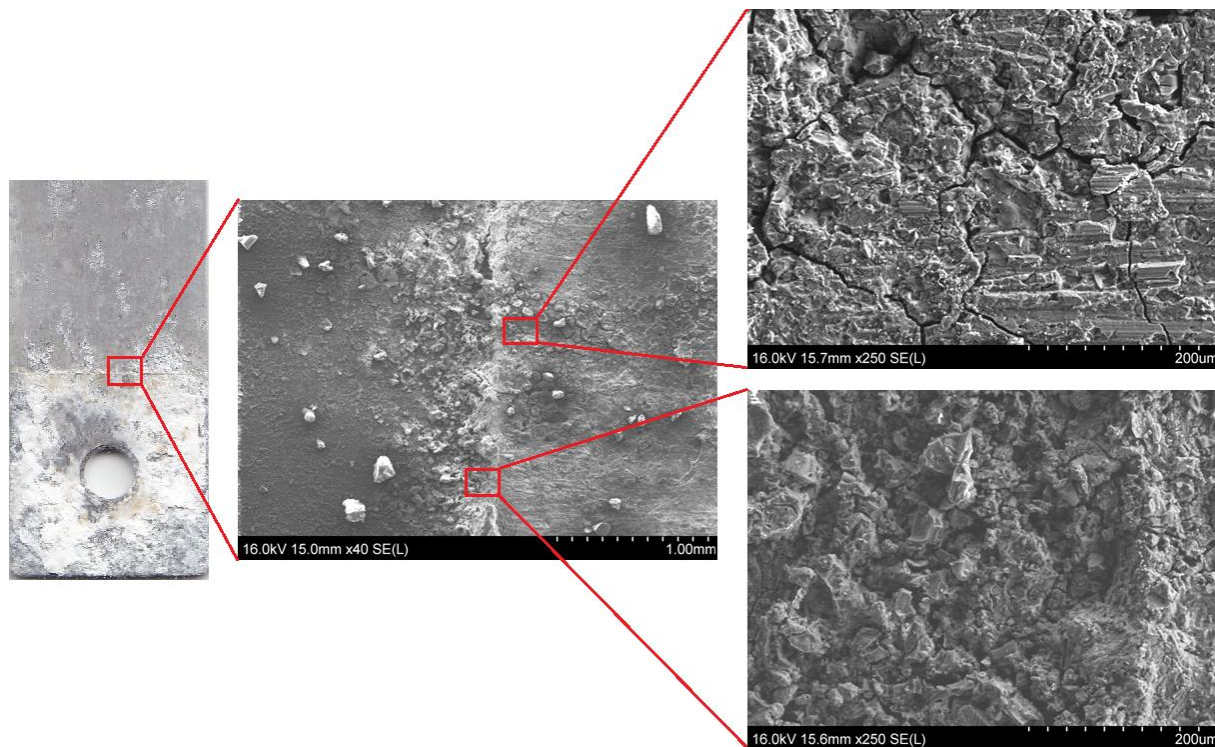


Fig. 31. SEM of interface between covered (top right) and uncovered (bottom right) regions of Al coupled to Ag at MCBH.

Table 27: Elemental composition of regions shown in Fig. 31.

Element		O	Al	C	Mg	Cl	Na	S	Ca	Ag	Si	Fe	K
Atomic %	Covered	70.1	13.0	6.42	6.42	1.7	1.25	0.63	0.62	0.16			
	Uncovered	72.1	9.87		10.1	2.40	1.79	0.78	0.70		1.50	0.73	0.11

For the uncovered region, the iron and silicon included in the composition analysis suggests that the Al oxide corrosion product did not completely shield the alloying elements. Oxygen was the most abundant element, primarily due to the formation of aluminum oxide. For the covered region, the presence of silver was detected in addition to the other common elements. This may be attributed to contamination of the Al by Ag which likely accelerated the corrosion of the Al coupon.

The sample that experienced the most corrosion at MCBH was the Al that was coupled to Cu. A typical region on the uncovered surface of Al coupled to Cu is shown in Fig. 32. An abundance of salt particles are visible in the micrograph; however, corrosion of the Al surface is less severe than that of the Al coupled to Ag.

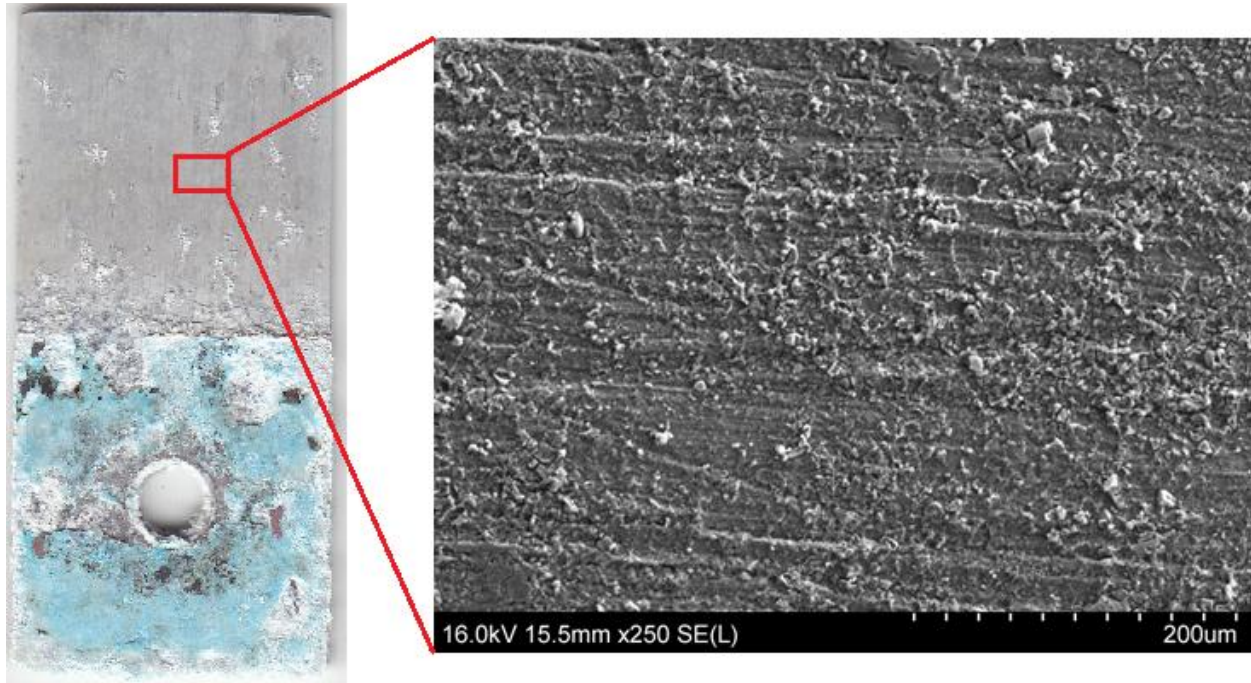


Fig. 32. SEM of uncovered region of Al coupled to Cu exposed at MCBH.

Compositional analysis was performed on the thick layer of product on the Al coupon in the region covered by Cu. Visual inspection indicates that elemental transfer from the Cu coupon occurred. A micrograph was taken of a typical part of this region (Fig. 33) and compositional analysis was performed in three areas: 1) the entire area of the micrograph, 2) pointwise on one of the spheres shown in the top region of the micrograph, and 3) pointwise on the thick crust layer on the bottom right of the micrograph. The results of this analysis are shown in Table 28.

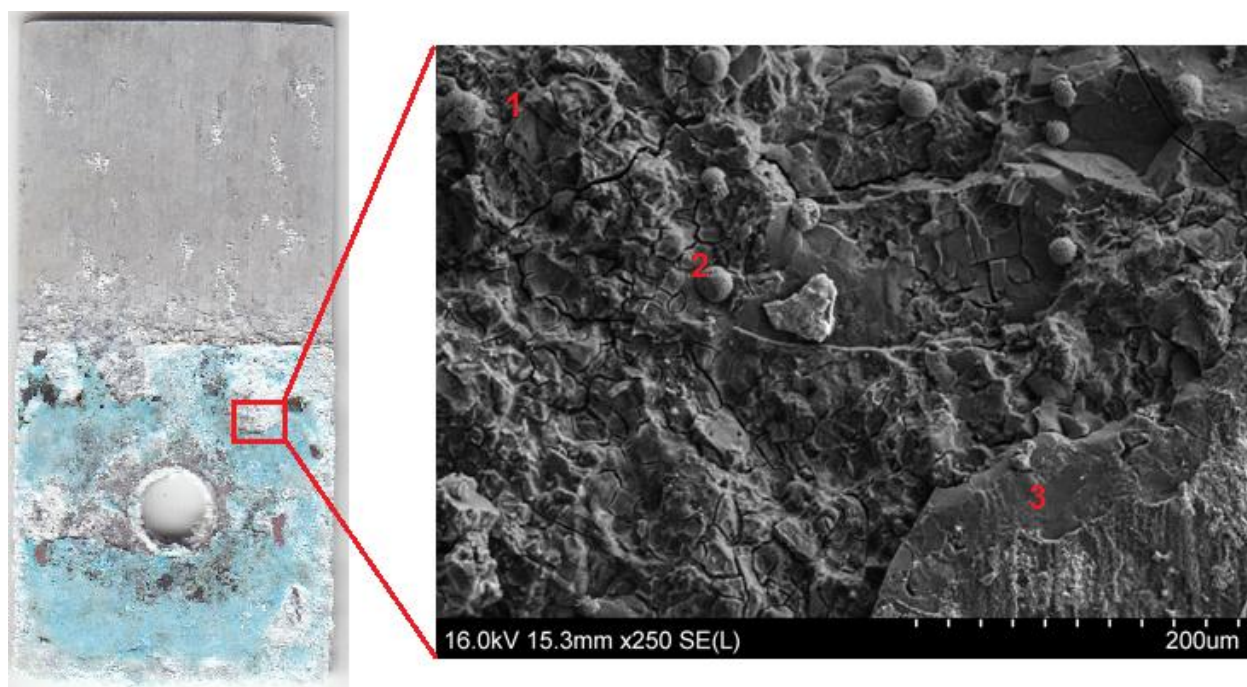


Fig. 33. SEM of covered region of Al coupled to Cu exposed at MCBH.

Table 28: Elemental composition of regions shown in Fig. 33.

Element		O	Al	C	Mg	Na	Cu	Cl	Ca	S
Atomic %	1 Region	68.5	12.4	9.55	4.09	1.47	2.06	1.01	0.51	0.47
	2 Sphere	64.4	0.86	17.4					17.3	
	3 Crust	57.5	5.57	10.7	3.19		22.5	0.56		

The analysis of the entire area shown in the micrograph is similar to that of the covered area of the Al coupled to Ag, with a notable exception that the presence of copper was detected instead of Ag. This also suggests that copper was deposited onto the surface of the Al and accelerated corrosion in this region. A pointwise analysis of one of the spheres shown in the micrograph identifies this as calcium carbonate. In the third analysis, the atomic percentage of copper increased significantly to 22.5%, indicating that some regions of the Al coupon were contaminated by the Cu coupon more heavily than others.

The Al coupon coupled to Ti corroded the least amount of all couples in which Al was the anode. The micrograph of the longitudinal end of the uncovered surface of Al shows minimal corrosion in addition to typical salt deposits (Fig. 34).

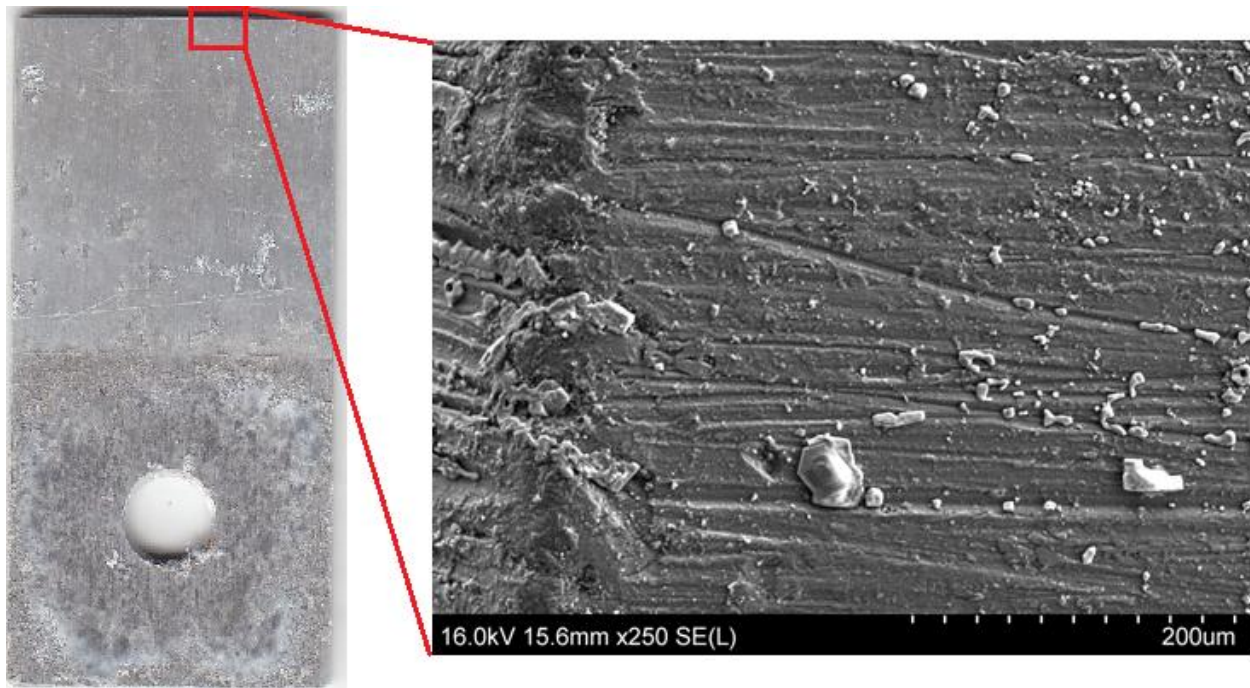


Fig. 34. SEM of uncovered region of Al coupled to Ti exposed at MCBH.

The uncovered surface of the Al coupled to stainless steel showed a surface morphology that was less corroded than that of Al coupled to Cu (Fig. 35). The surface analysis of the whole region shown in Fig. 35 (left SEM) did not show any atypical results. However, the dark flat deposits were magnified and examined in more detail.

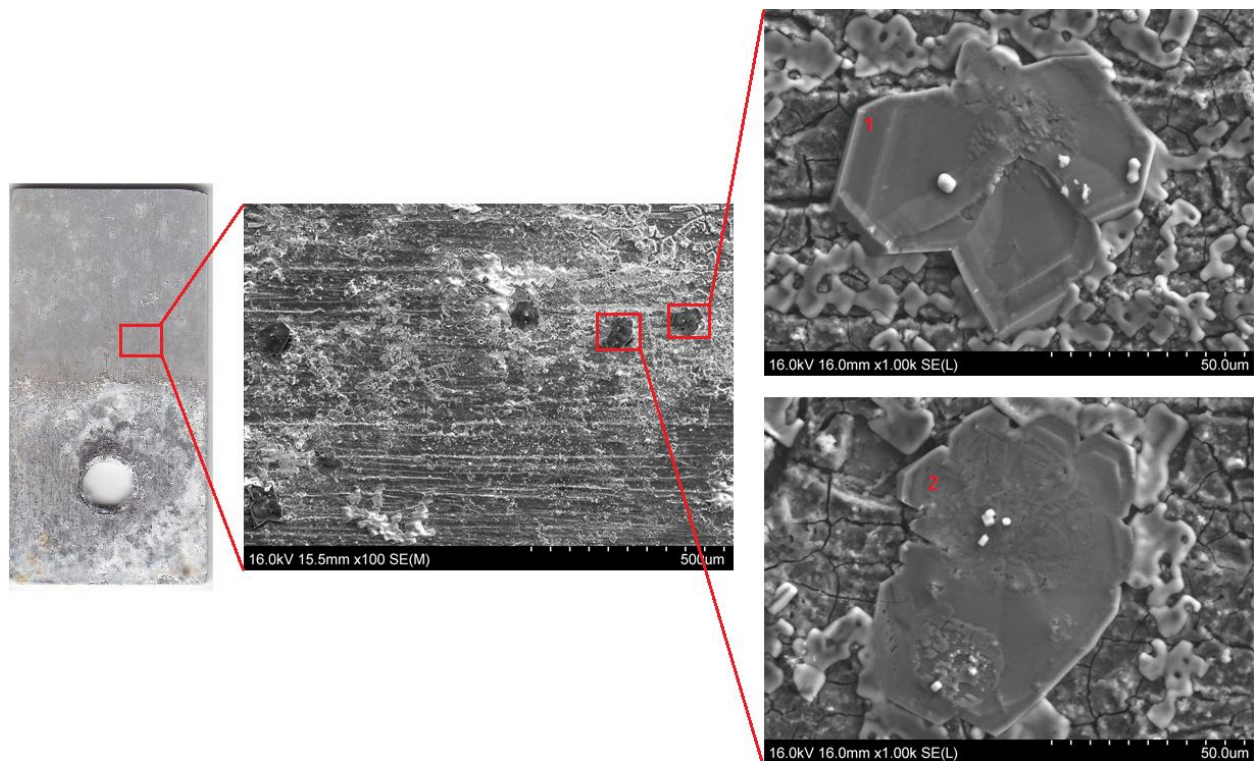


Fig. 35. SEM of uncovered region of Al coupled to stainless steel exposed at MCBH.

Table 29: Elemental composition of regions shown in Fig. 35.

Element		O	B	S	Ca	C	Na	Al
Atomic %	1	67.1	19.2	8.50	7.54	3.27	0.29	0.15
	2	58.4	16.5	10.9	10.0	3.89	0.31	

The elemental analysis identified these as boron salts (Table 29). More of these boron compounds were found upon further examination of the uncovered surface (Fig. 36). Boron is known to be present in seawater albeit in much smaller amounts than sodium, calcium, potassium, and many other elements. However, on this particular specimen it was present in large enough quantities to deposit in several areas on this Al surface.

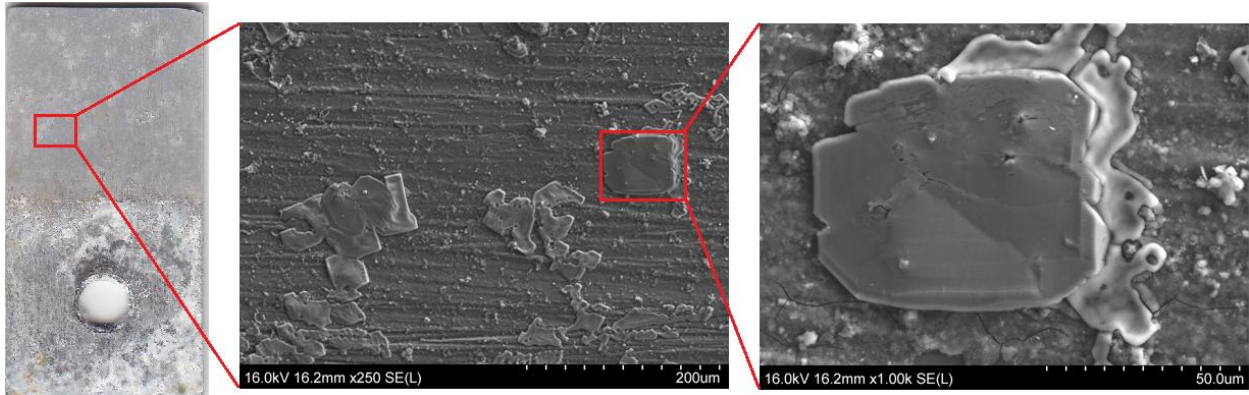


Fig. 36. SEM of boron salts found on Al coupled to stainless steel at MCBH.

The region of Al covered by stainless steel was also examined for corrosion morphology. Since stainless steels are extremely susceptible to crevice corrosion, the propagation of crevice corrosion in the interface of the two coupons could facilitate crevice corrosion on the Al as well. Fig. 37 is a micrograph of a region around the hole in the Al through which the fastener was placed. This region shows degradation of the passive layer on the Al surface.

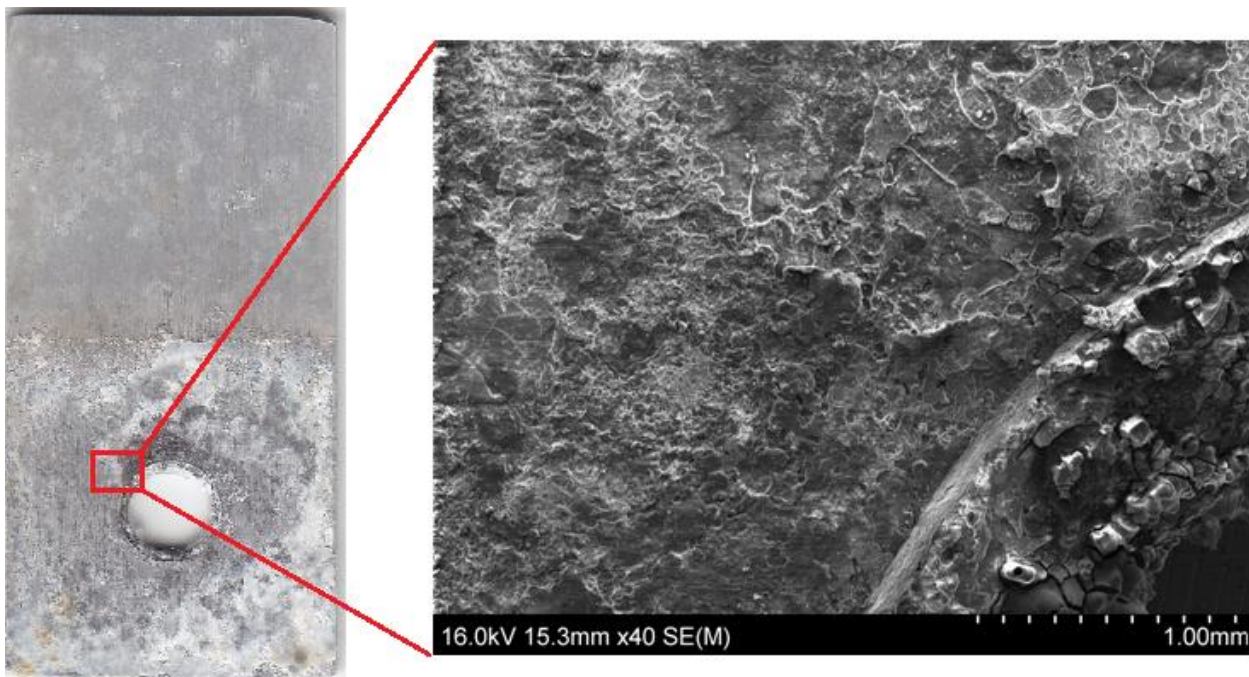


Fig. 37. SEM of covered region of Al coupled to stainless steel near the crevice mouth exposed at MCBH.

Although X-on-top orientation of Al coupled to mild steel had the second highest corrosion rate, a scan of a typical area of the uncovered surface did not show obvious signs of heavy corrosion (Fig. 38). Visual inspection of the coupon shows that rust from the mild steel readily adhered to the Al surface both in the covered region and the uncovered region closest to the mild steel.

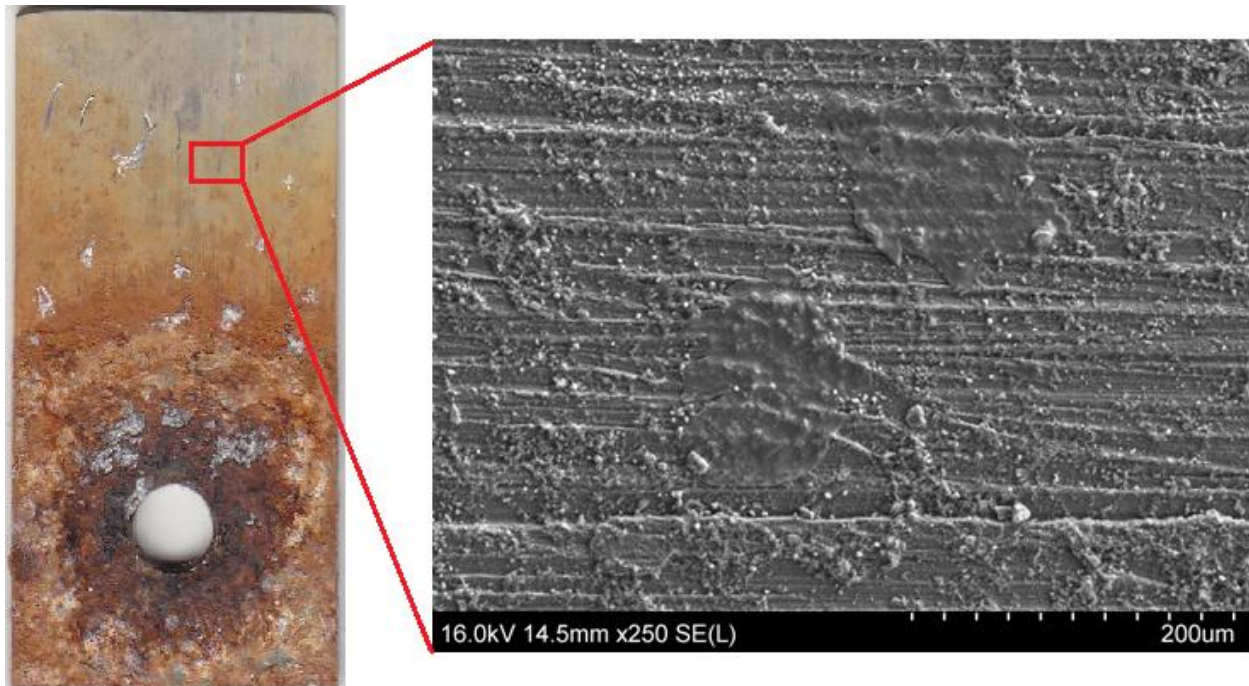


Fig. 38. SEM of uncovered region of Al coupled to mild steel exposed at MCBH.

The high amount of corrosion in the region covered by mild steel compared to the relatively uncorroded uncovered region suggests that most of the Al corrosion occurred in the interface between the mild steel and the Al. A micrograph of the interface of the uncovered and covered regions of the Al coupon coupled shows an extremely thick layer of product in the region covered by the mild steel (Fig. 39). Elemental composition of the covered region of the Al coupon is shown in Table 30. A high amount of iron is present due to the transfer of corrosion

product from the mild steel. The uncovered region closest to the Al-mild steel interface shows a heavy amount of blistering and corrosion initiation.

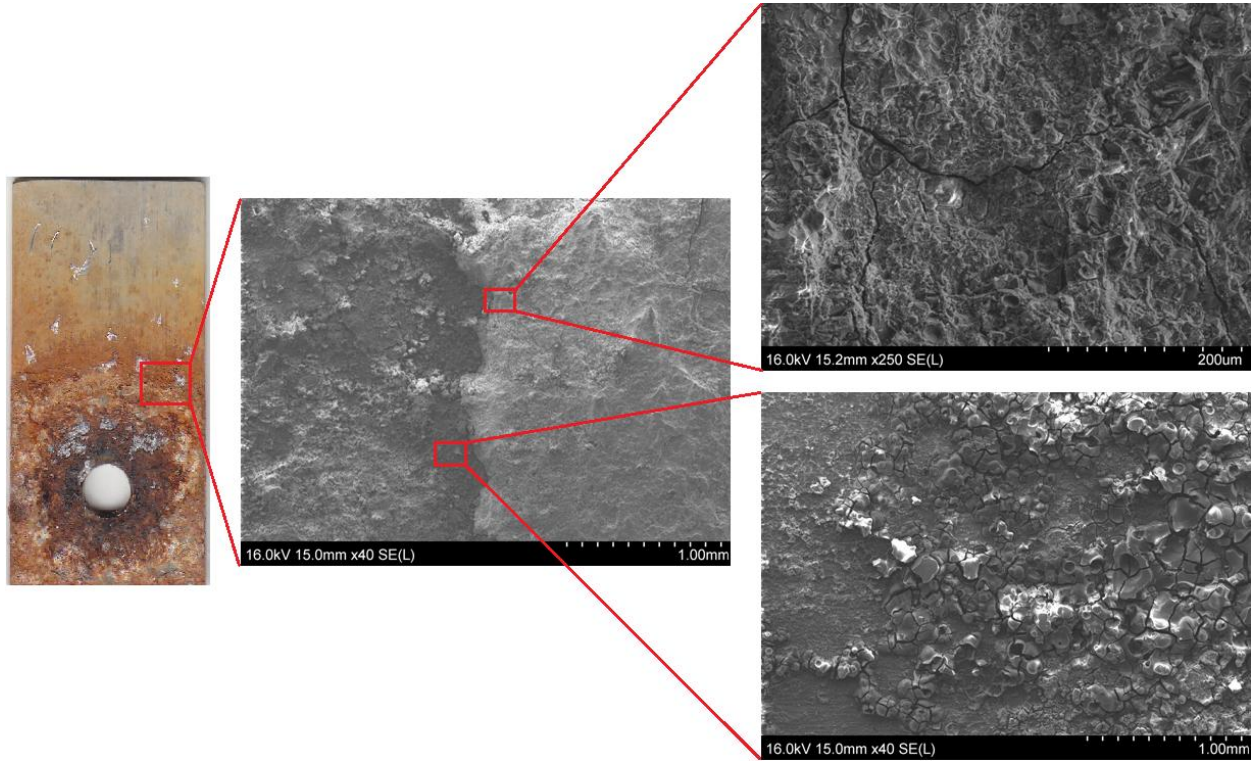


Fig. 39. SEM of the interface between covered (top right) and uncovered (bottom right) regions of Al coupled to mild steel at MCBH.

Table 30: Elemental composition of the covered region shown in Fig. 39.

Element	O	Al	Fe	C	Na
Atomic %	72.2	16.9	1.72	1.90	1.60

The Al coupons coupled to Mg had the lowest corrosion rate of all galvanic couples. Fig. 40 shows a micrograph of the longitudinal edge of the uncovered region of the Al in which minimal corrosion is shown.

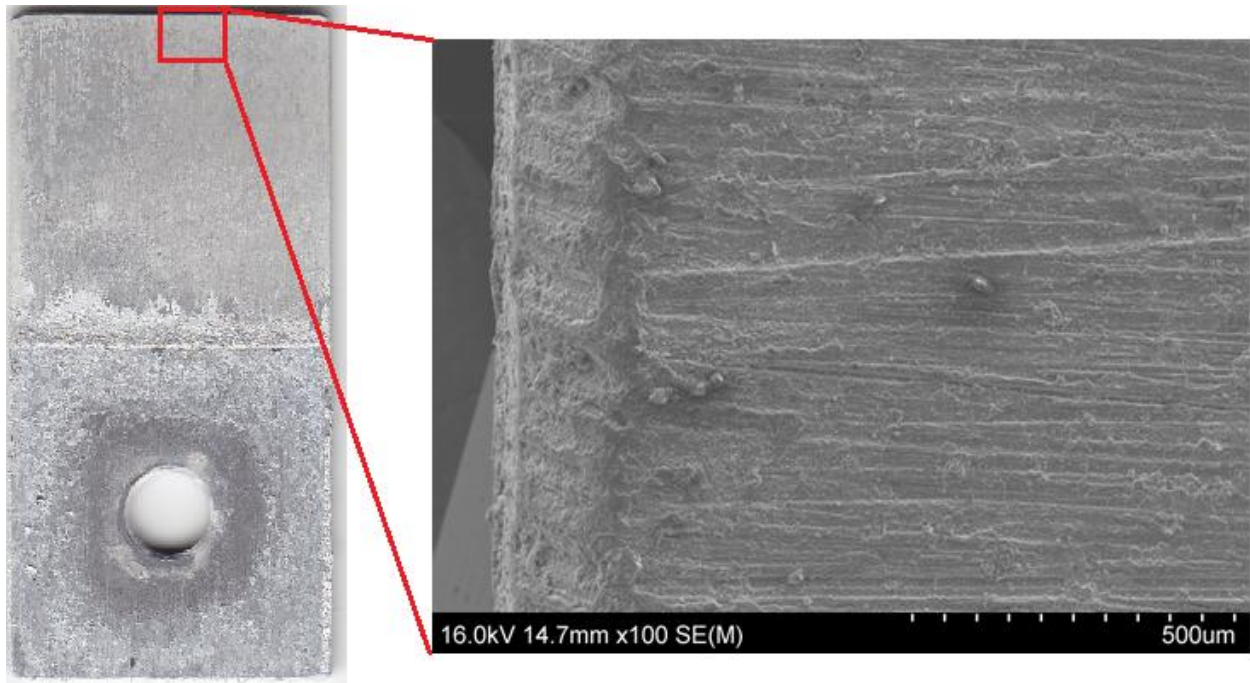


Fig. 40. SEM of uncovered region of Al coupled to Mg exposed at MCBH.

Most of the Al corrosion occurred in the interface of the two metals where Al was covered. Fig. 41 compares the difference in corrosion morphology in this interfacial region for the Al coupled to Mg, which had the lowest corrosion rate, compared to the Al coupled to Ag, which had a relatively high corrosion rate.

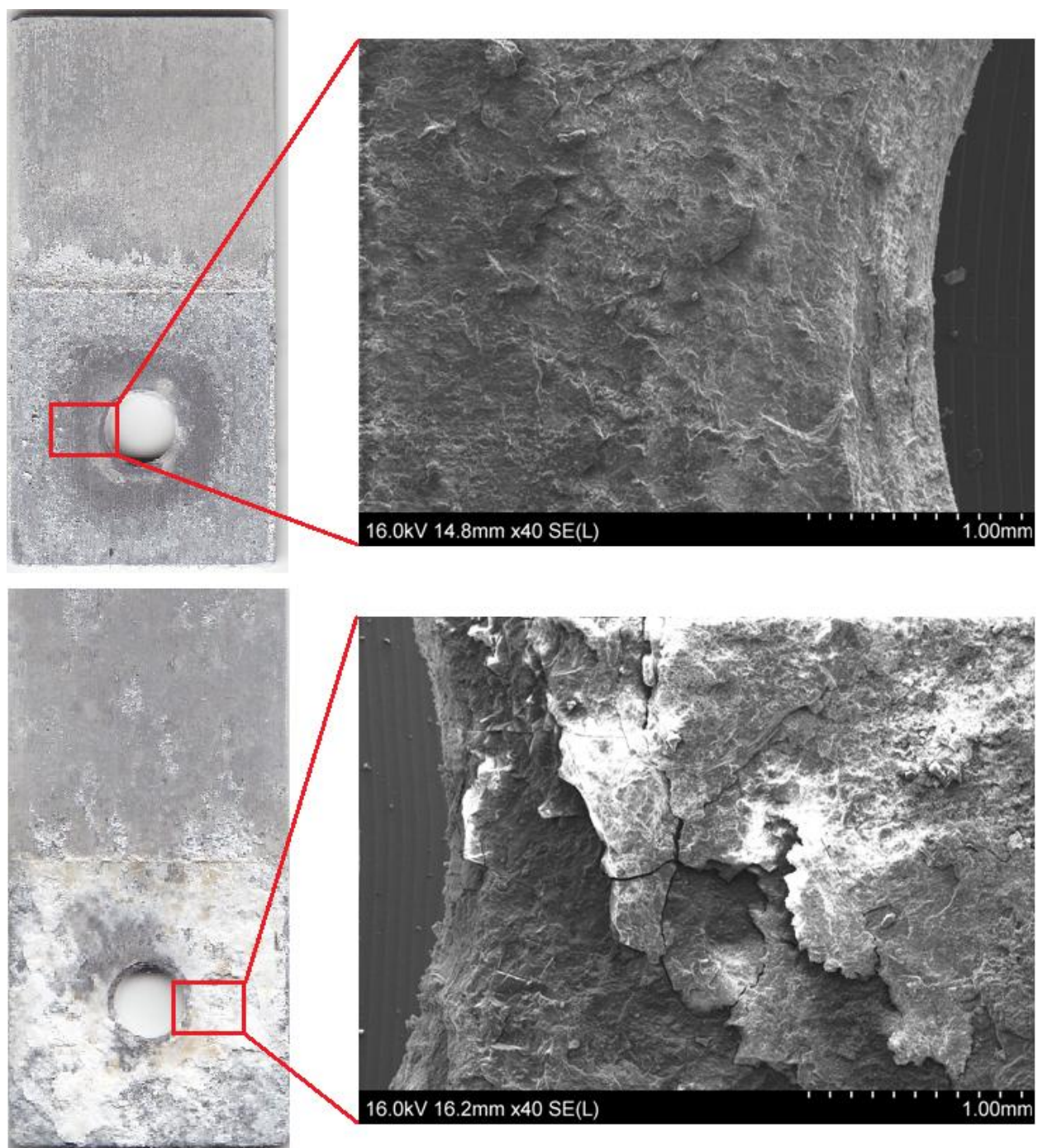


Fig. 41. SEM comparison of corrosion in covered regions of Al coupled to Mg (top) and Al coupled to Ag (bottom) exposed at MCBH.

6.1.2. Test specimens at Lyon Arboretum

The uncoupled Al exposed at Lyon Arboretum lacked the abundance of salts found on the uncoupled Al exposed at MCBH. The uncoupled Al at Lyon Arboretum experienced the lowest corrosion rate of all the test specimens and its morphology is shown in Fig. 42. Elemental analysis was again performed in order to identify the environmental products. Composition of the uncoupled coupon is shown in Table 31.

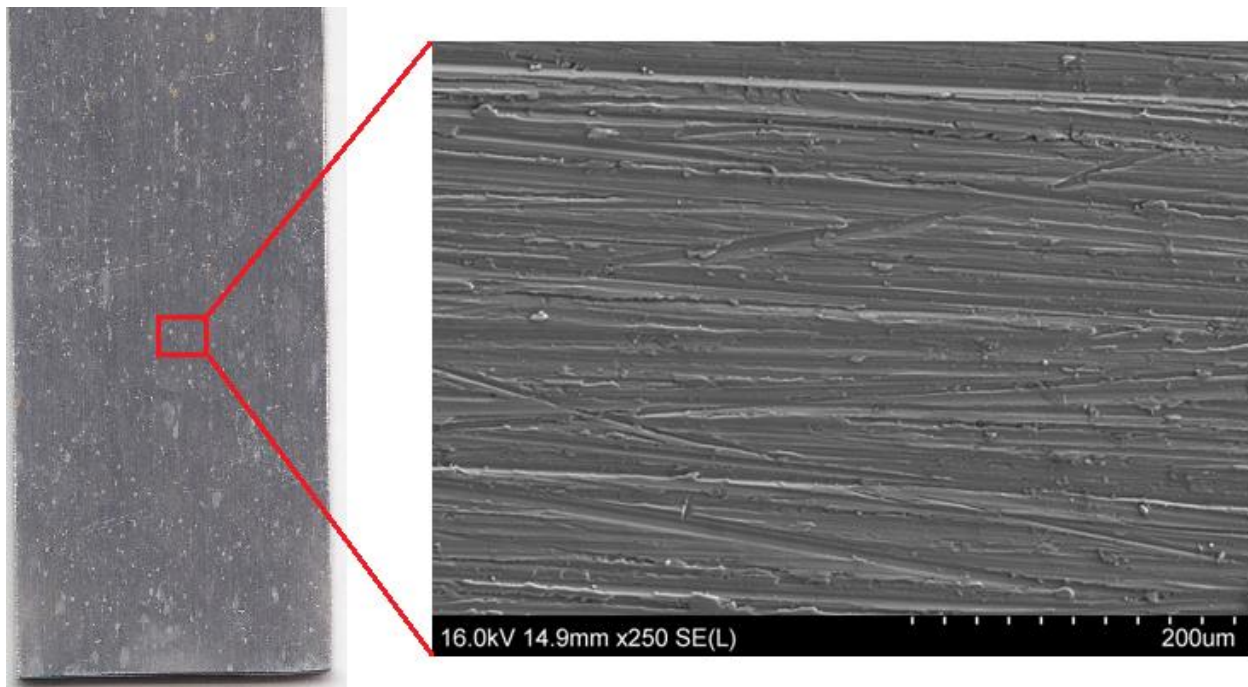


Fig. 42. SEM of uncoupled Al exposed at Lyon Arboretum.

Table 31: Elemental composition of region shown in Fig. 42.

Element	Al	O	C	Mg	Si	Fe	P	Cr
Atomic %	69.8	16.5	11.8	0.66	0.47	0.31	0.24	0.10

The elemental analysis shows that chromium and phosphorus were present in addition to the previously stated alloying elements. Chromium is also an alloying element and its presence is in

accordance with the composition of the alloy. The presence of phosphorous may be attributed to rain water or organic life found in the rainforest environment.

Al coupled to Ag at Lyon Arboretum had the highest corrosion rate at this test site; however, the corrosion rate was still much lower than that of the chloride-heavy environments (MCBH and in the CCTC). A micrograph of the uncovered surface of Al coupled to Mg is shown in Fig. 43.

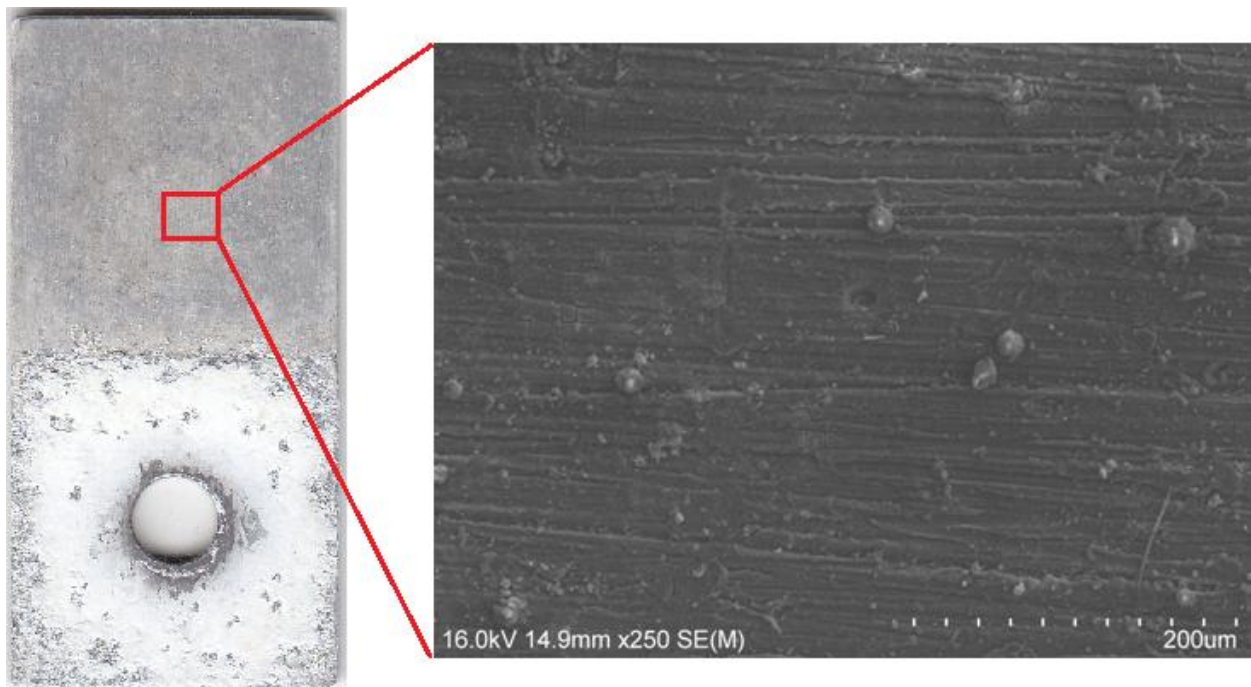


Fig. 43. SEM of uncovered region of Al coupled to Ag exposed at Lyon Arboretum.

Inspection for corroded areas of the uncovered region of the Al coupled to Cu were discovered and magnified to 1000x. Elemental analysis was performed in one such region where cracking of the oxide layer was apparent (Fig. 44). The composition of this region is shown in Table 32.

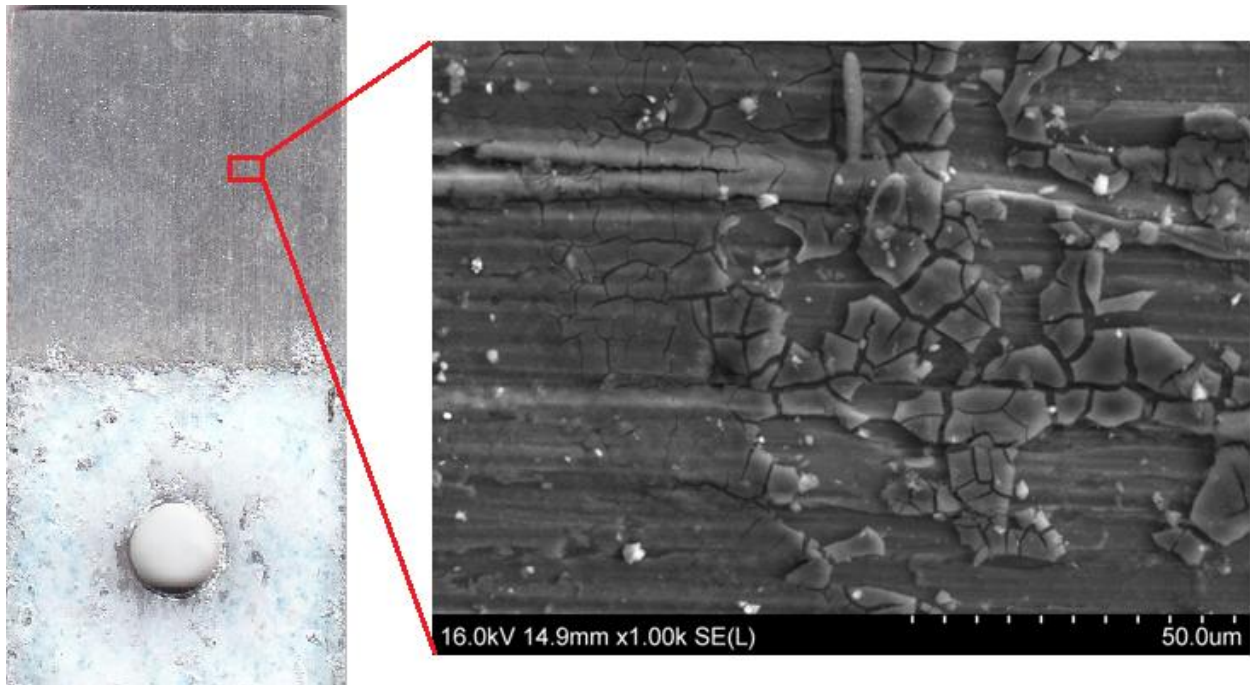


Fig. 44. SEM of surface cracking on the uncovered region of Al coupled to Cu at Lyon Arboretum.

Table 32: Elemental composition of region shown in Fig. 32.

Element	Al	O	C	Mg	Si	S	Fe	P	Cu
Atomic %	51.9	37.4	9.25	0.49	0.41	0.27	0.13	0.10	0.06

The composition includes copper though in such small quantities that its presence may be attributed to the composition of the Al alloy.

The presence of copper in the covered crevice region of the Al coupon was again visually apparent. Elemental analysis of the region covered by the Cu coupon confirms the presence of copper (Fig. 45 and Table 33).

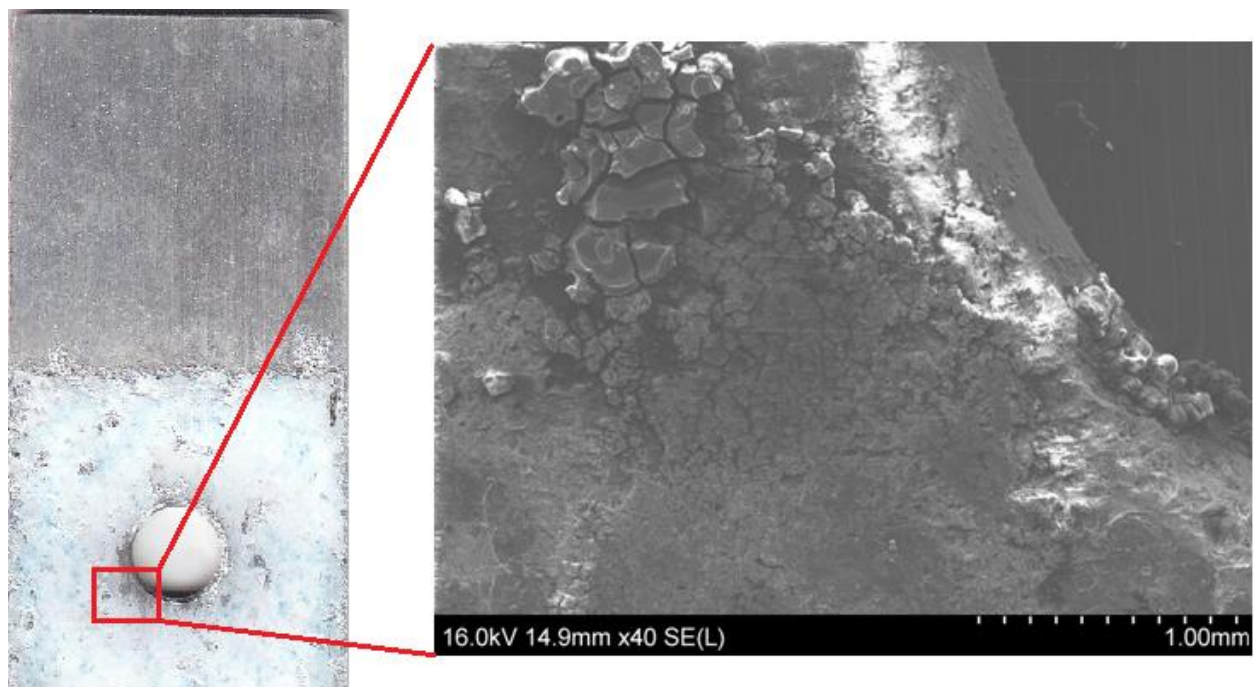


Fig. 45. SEM of covered region of Al coupled to Cu exposed at Lyon Arboretum.

Table 33: Elemental composition of region shown in Fig. 45.

Element	O	Al	C	Cu	Mg	Si
Atomic %	75.2	19.8	4.10	0.41	0.34	0.11

The corrosion product from the mild steel was again present on the surface of the Al to which it was coupled. Composition of an area of the covered region of Al close to the fastener hole (Fig. 46) is listed in Table 34.

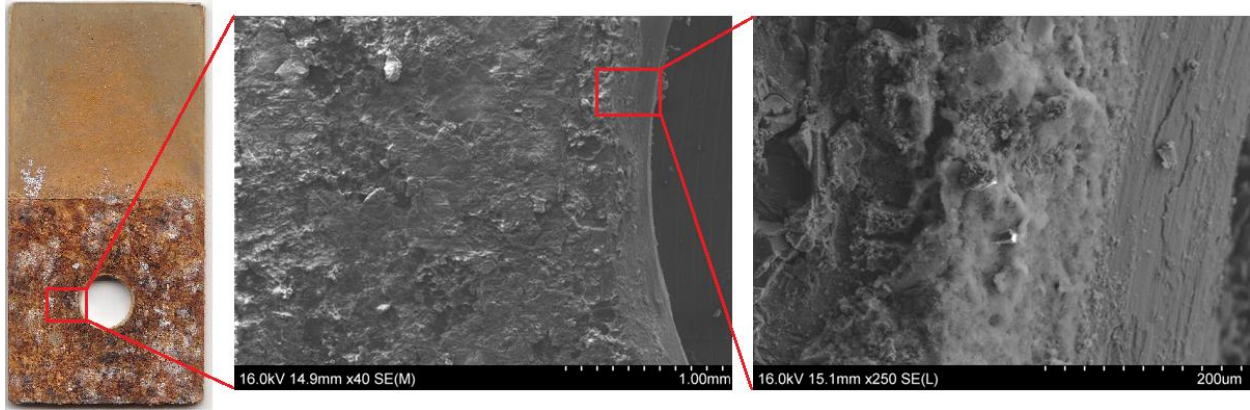


Fig. 46. SEM of covered region of Al coupled to mild steel exposed at Lyon Arboretum.

Table 34: Elemental composition of region shown in Fig. 46.

Element	O	Fe	Al	C	Mn
Atomic %	62.6	19.0	14.40	3.60	0.36

Iron was present in large amounts as expected. Manganese was also discovered in the analysis. Although manganese is an alloying element of Al, the amount present was higher than the composition of the alloy. The mild steel also contains Mn as an alloying element.

The Al with the lowest corrosion rates at Lyon Arboretum, i.e. those coupled to Ti, stainless steel, and Mg (Figs. 47-49), showed minimal signs of corrosion and no elements previously unseen during compositional analysis.

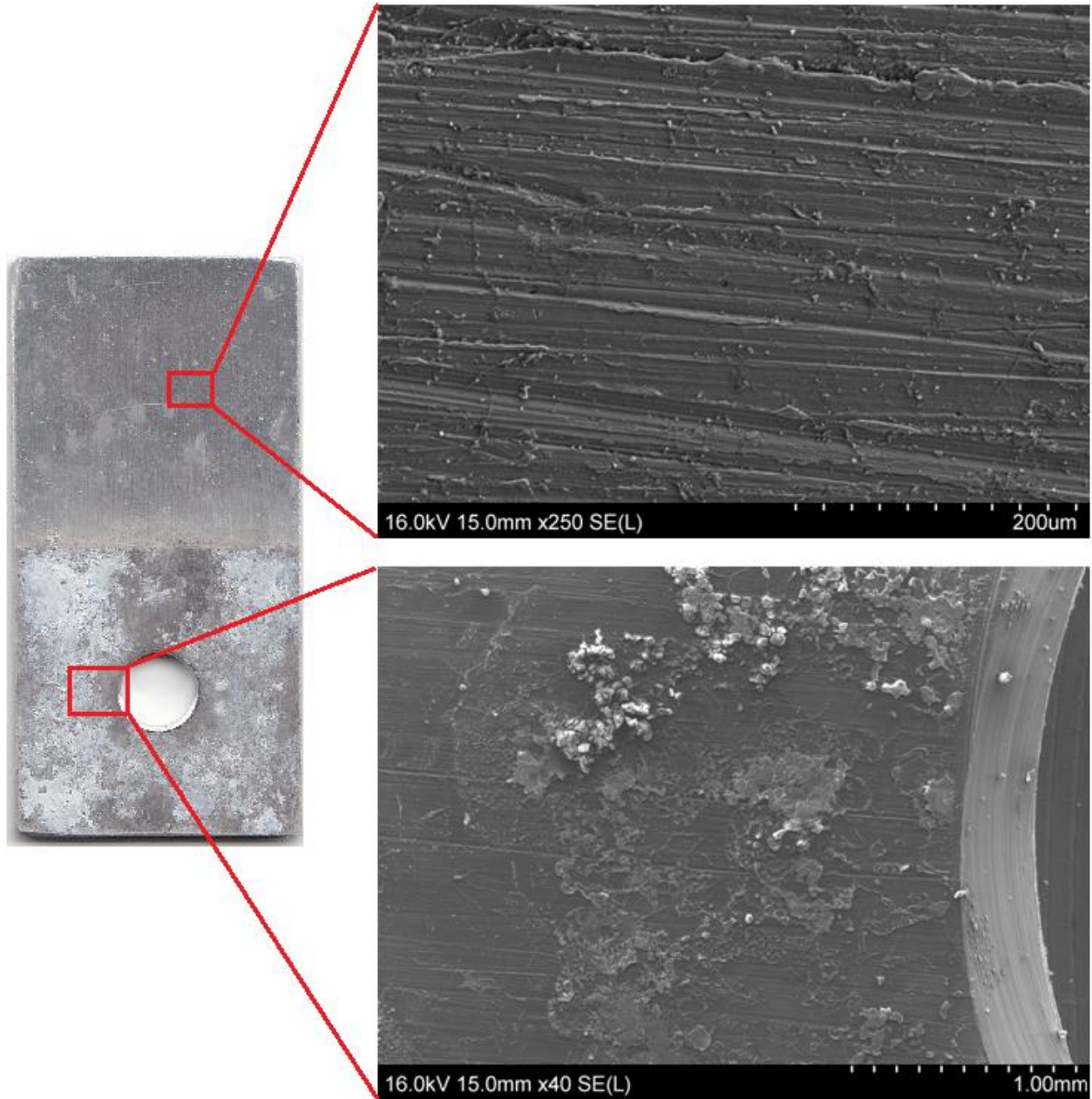


Fig. 47. SEM of covered and uncovered regions of Al coupled to Ti exposed at Lyon Arboretum.

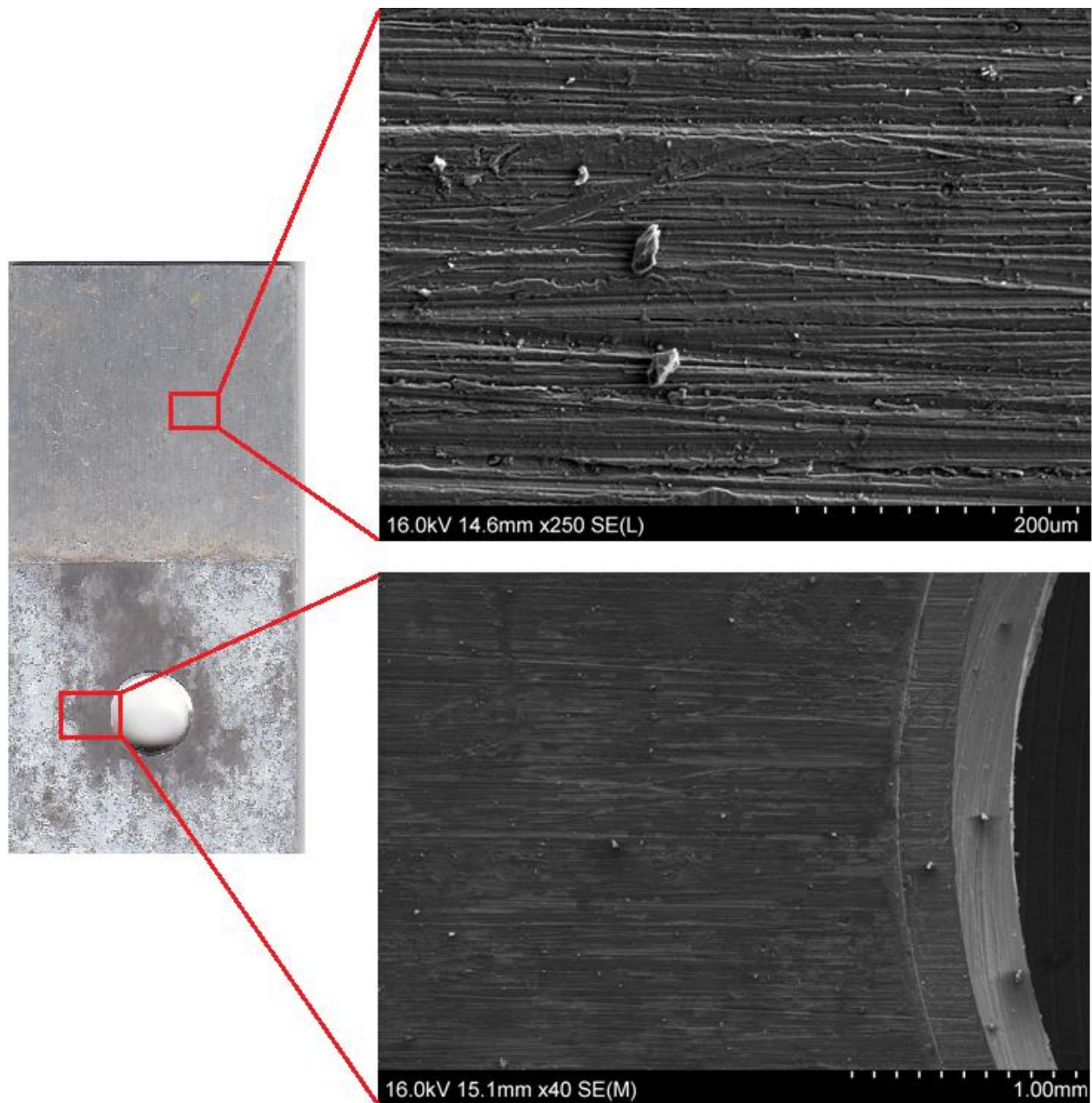


Fig. 48. SEM of covered and uncovered regions of Al coupled to stainless steel exposed at Lyon Arboretum.

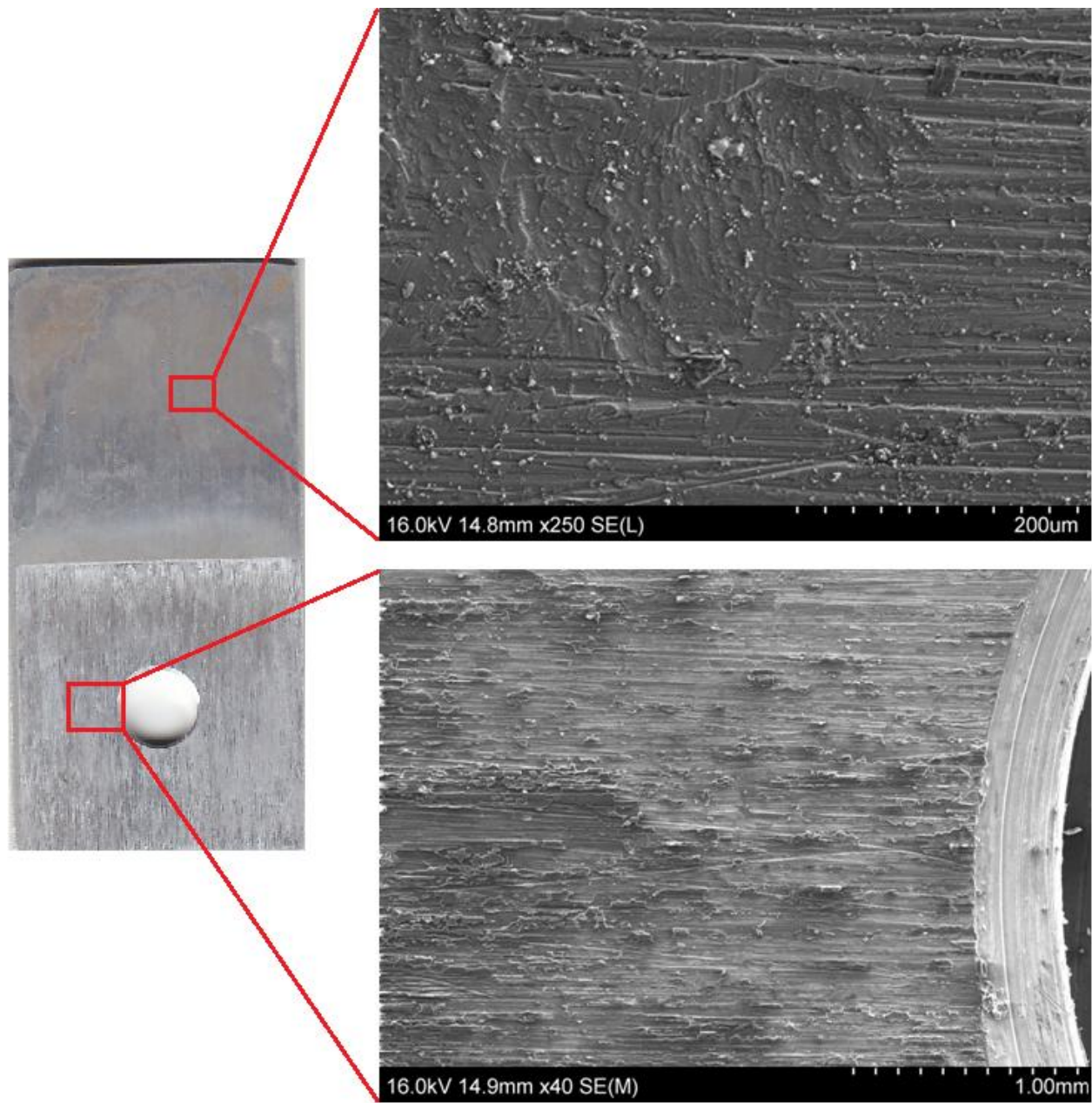


Fig. 49. SEM of covered and uncovered regions of Al coupled to Mg exposed at Lyon Arboretum.

6.1.3. Test specimens at Kilauea Volcanoes National Park

Surface analysis of the uncoupled Al exposed at Kilauea yielded unique results. While the corrosion rate was found to be comparable to the other outdoor test sites, the high atomic percentage of sulfur found in the pits on the surface of the uncoupled Al were exclusive to this test site (Table 35). In a volcanic environment, sulfur originates from sulfur dioxide which reacts with oxygen and water in the environment to form sulfuric acid. The sulfur detected using EDXA is likely in the form of a sulfate salt.

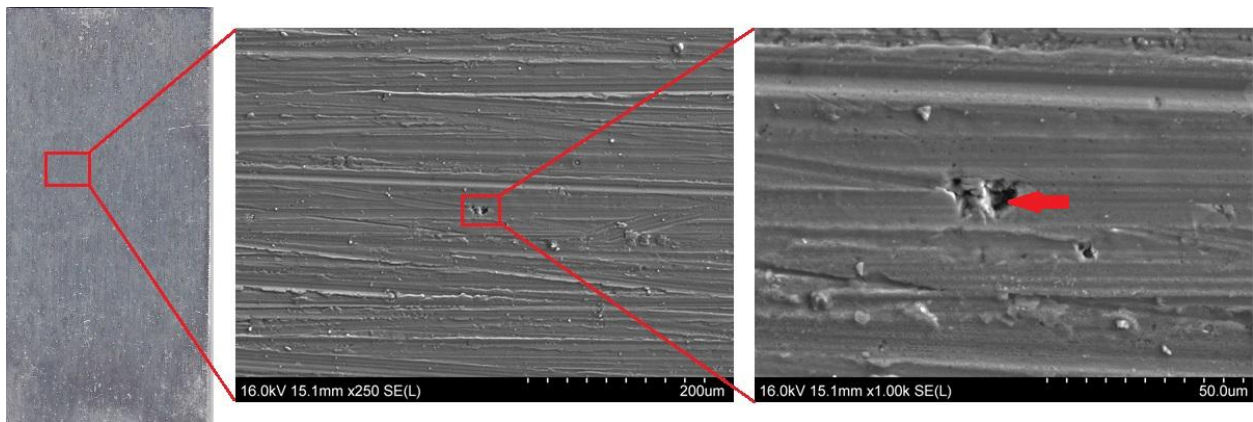


Fig. 50. SEM of uncoupled Al exposed at Kilauea.

Table 35: Elemental composition of regions shown in Fig. 50.

Element	Al	O	C	Mg	Si	S	Fe	Cr	Na
Region	78.9	15.0	4.17	0.76	0.5	0.32	0.22	0.12	0.29
Atomic % Pit	70.2	18.9		0.34	0.33	2.99	6.30	0.71	

Elemental analysis of corroded regions of Al coupled to Ag as well as the Al coupled to Cu showed contamination of the uncovered region by their respective coupled metals (Tables 36 and 37). Further analysis into a pit on the Al coupon coupled to Cu showed an increased amount of copper present in the pit. This suggests that the pitting was initiated or propagated by copper migration from the Cu coupon to the uncovered region of the Al coupon.

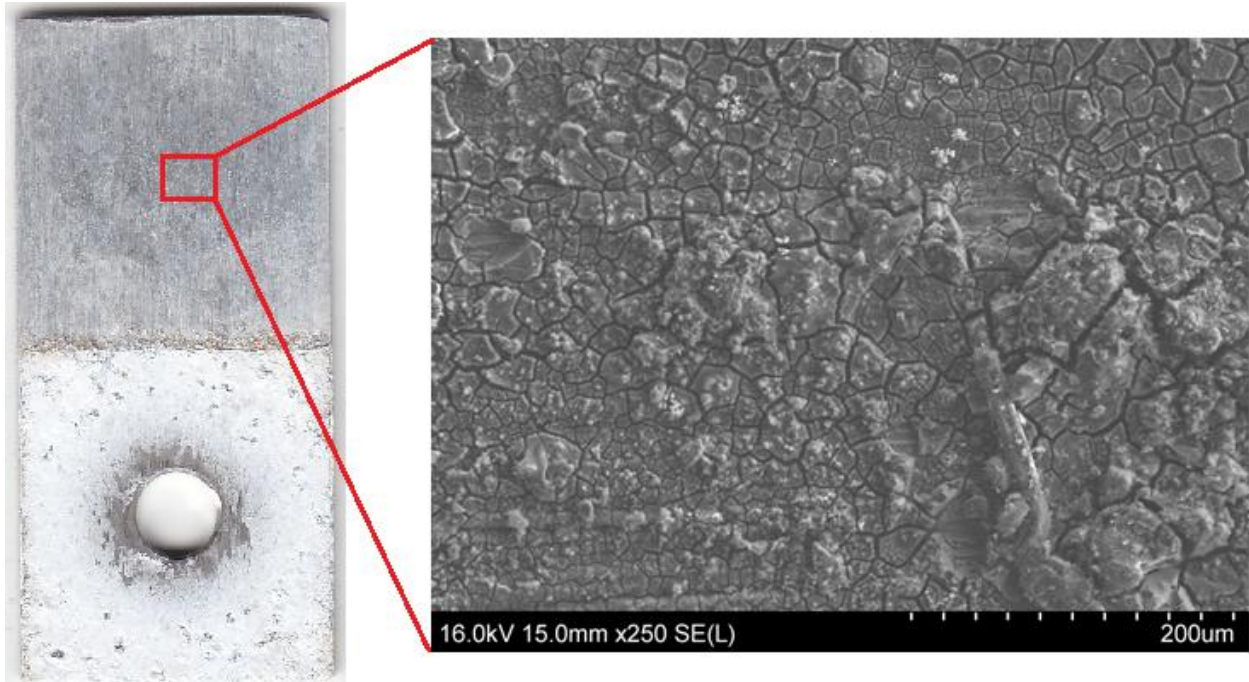


Fig. 51. SEM of uncovered region of Al coupled to Ag exposed at Kilauea.

Table 36: Elemental composition of region shown in Fig. 51.

Element	O	Al	S	C	Si	Ag
Atomic %	73.6	18.6	4.25	2.85	0.50	0.14

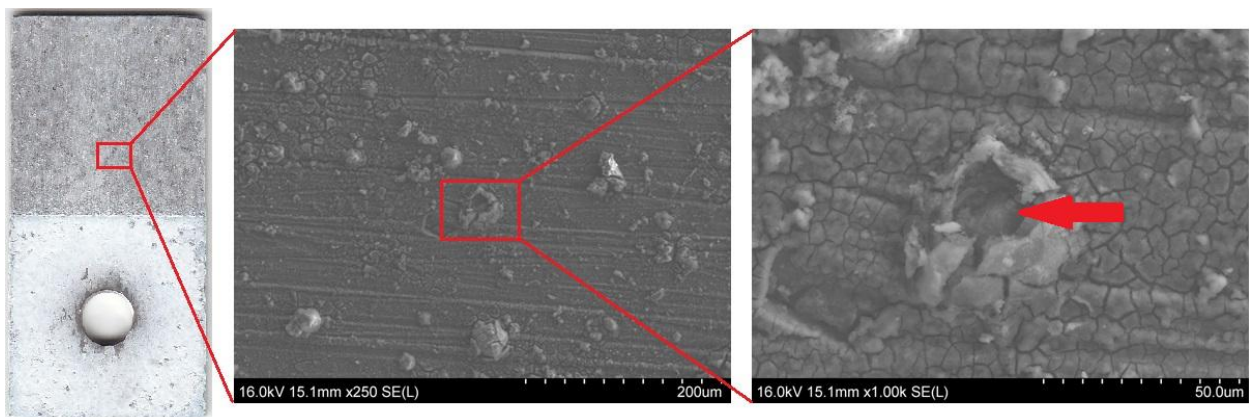


Fig. 52. SEM of uncovered region of Al coupled to Cu exposed at Kilauea.

Table 37: Elemental composition of regions shown in Fig. 52.

Element		O	Al	S	C	Mg	Si	Cu	Fe
Atomic %	Region	62.3	31.5	2.95	2.80	0.27	0.20	<0.00	
	Pit	45.1	48.4	3.71		0.65		1.81	0.32

The sets of Al coupled to either Ti or stainless steel had a roughly equal corrosion rate. The morphology of the surfaces of these Al coupons were similar (Figs. 53 and 54), as are their elemental compositions (Tables 38 and 39).

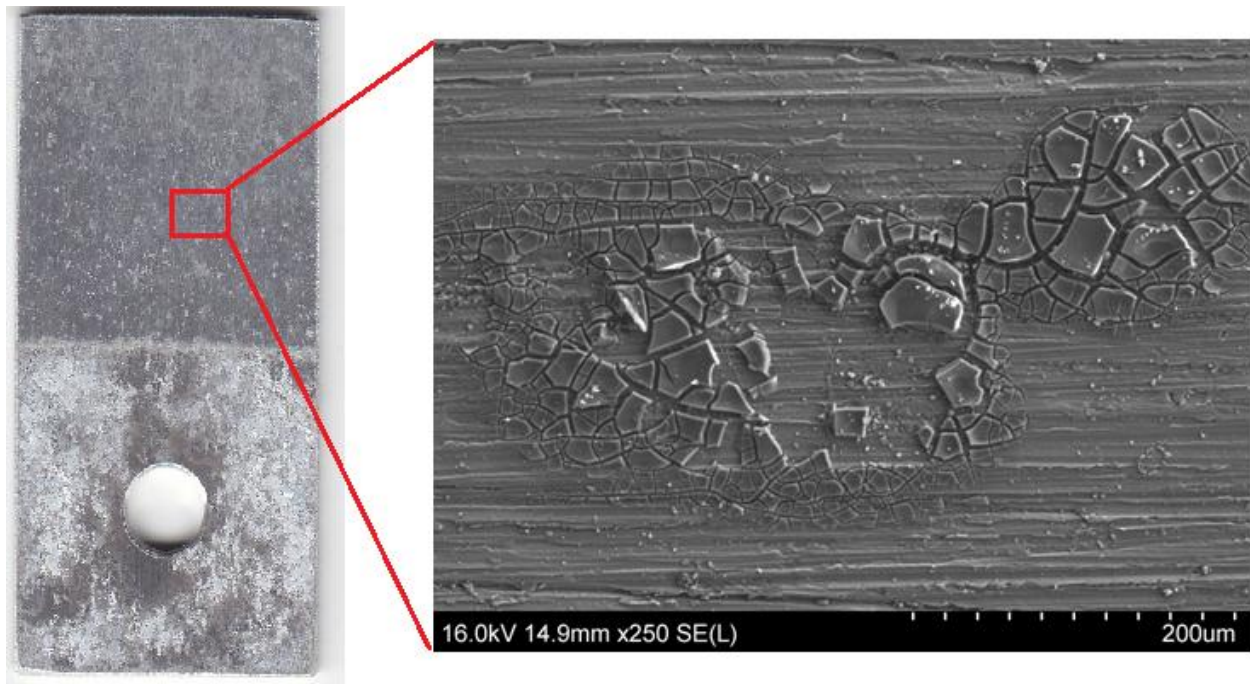


Fig. 53. SEM of uncovered region of Al coupled to Ti exposed at Kilauea.

Table 38: Elemental composition of region shown in Fig. 53.

Element	O	Al	C	S	Si	Mg	Na	Cl	Fe
Atomic %	54.7	35.6	5.95	2.5	0.47	0.29	0.19	0.26	0.11

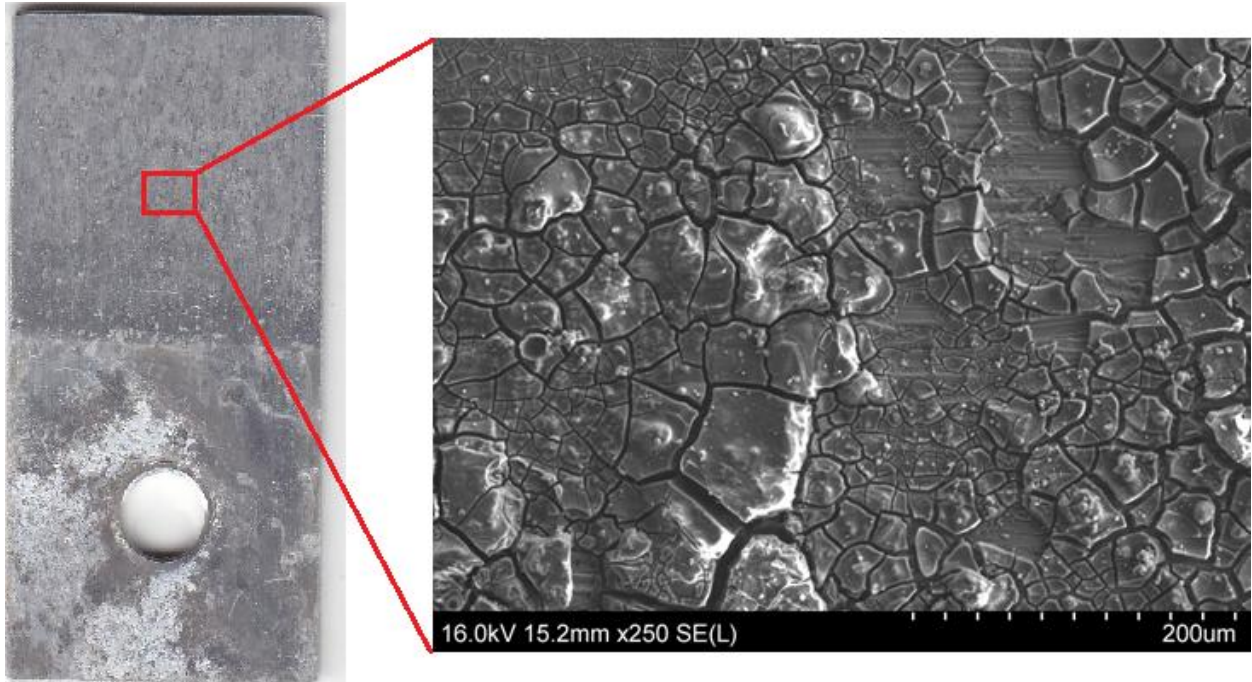


Fig. 54. SEM of uncovered region of Al coupled to stainless steel exposed at Kilauea.

Table 39: Elemental composition of region shown in Fig. 54.

Element	O	Al	S	C	Si	Na	Fe
Atomic %	70.3	22.2	3.62	3.24	0.39	0.20	0.12

On the uncovered surface of the Al coupled to stainless steel, a pit was magnified in order to obtain a pointwise elemental analysis of this corroded region (Fig. 55). At a magnification of 4000x an inclusion was found containing a high amount of silicon, a major alloying element. Other alloying elements were included in the elemental analysis such as iron and titanium. The composition inside this pit is shown in Table 40.

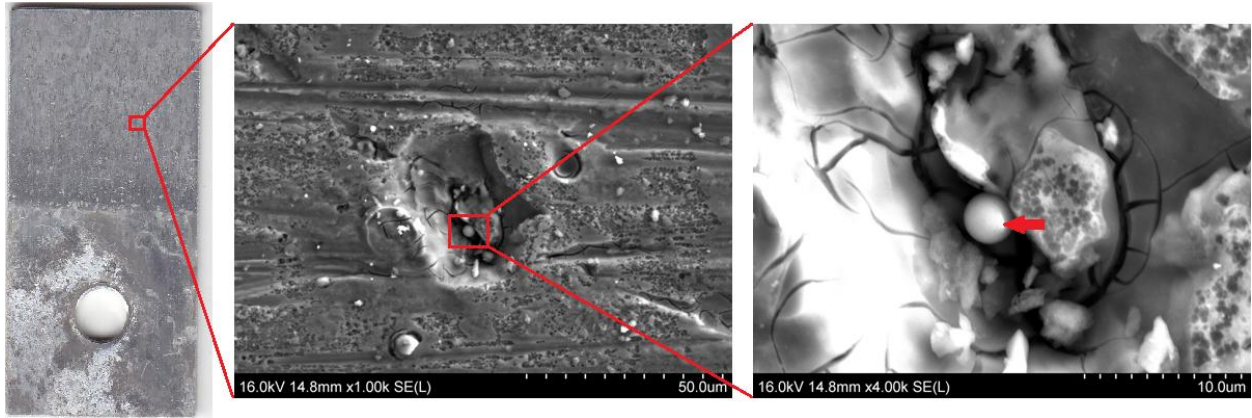


Fig. 55. SEM of pit on the uncovered region of Al coupled to stainless steel at Kilauea.

Table 40: Elemental composition of inclusion shown in Fig. 55.

Element	O	Si	Al	Ca	Mg	Fe	Na	Ti	K	S
Atomic %	67	14.8	8.16	2.87	2.87	2.33	1.1	0.52	0.27	0.16

A micrograph of Al coupled to mild steel was taken at the longitudinal edge of the uncovered surface (Fig. 56). The elemental analysis shows a high percentage of iron even at the furthest point from the actual mild steel coupon (Table 41). The migration of the corrosion product from the mild steel may have contributed to the relatively high corrosion rate compared to the Al coupled to the passivating metals.

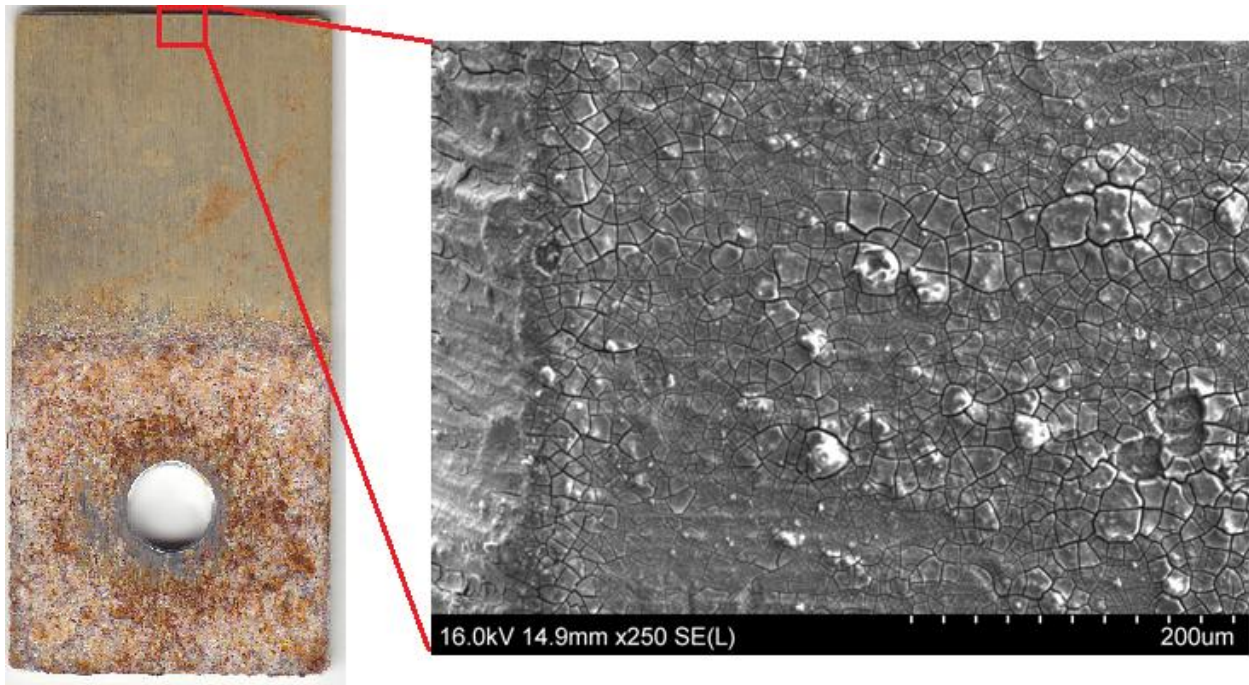


Fig. 56. SEM of uncovered region of Al coupled to mild steel exposed at Kilauea.

Table 41: Elemental composition of region shown in Fig. 56.

Element	O	Al	Fe	C	S	Si
Atomic %	67.1	18.3	5.93	4.37	4.01	0.27

The Al coupled to Mg had the lowest corrosion rate of all Al coupons exposed at Kilauea. This is reflected in the corrosion morphology shown in Fig. 57.

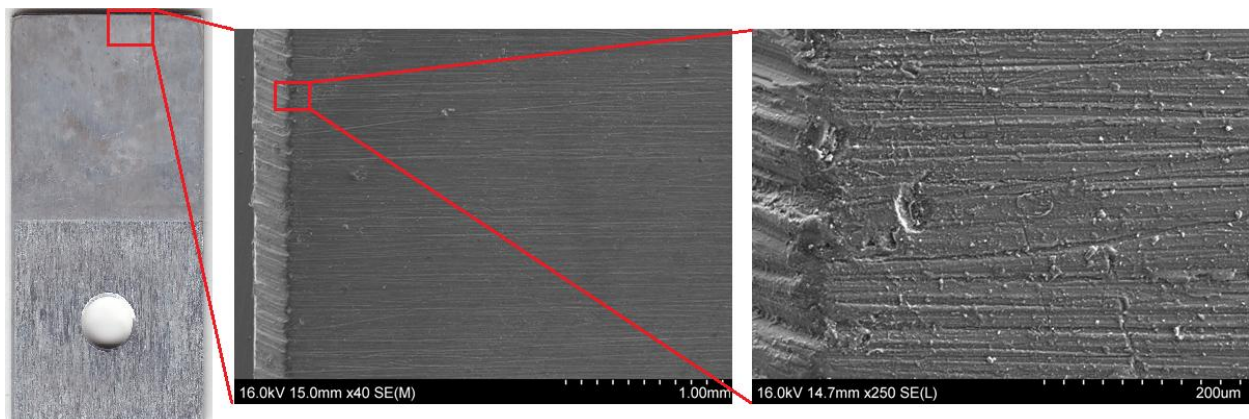


Fig. 57. Uncovered region of Al coupled to Mg exposed at Kilauea.

6.1.4. Test specimens in the cyclic corrosion testing chamber

Corrosion morphology in the Al coupons exposed in the CCTC was difficult to view in the uncoupled Al coupons as well as in the uncovered regions of the coupled Al coupons. This was due to the thick layer of salt deposited on the exposed surface of the Al from the accelerated corrosion test. A typical exposed region is shown in Fig. 58 which shows an Al coupon that was coupled to stainless steel following 30 cycles of the GM-9540P test; this region was subjected to elemental analysis. The region was further magnified and elemental analysis was again taken, showing an elemental composition predominated by calcium carbonate. Compositions of these regions are shown in Table 42.

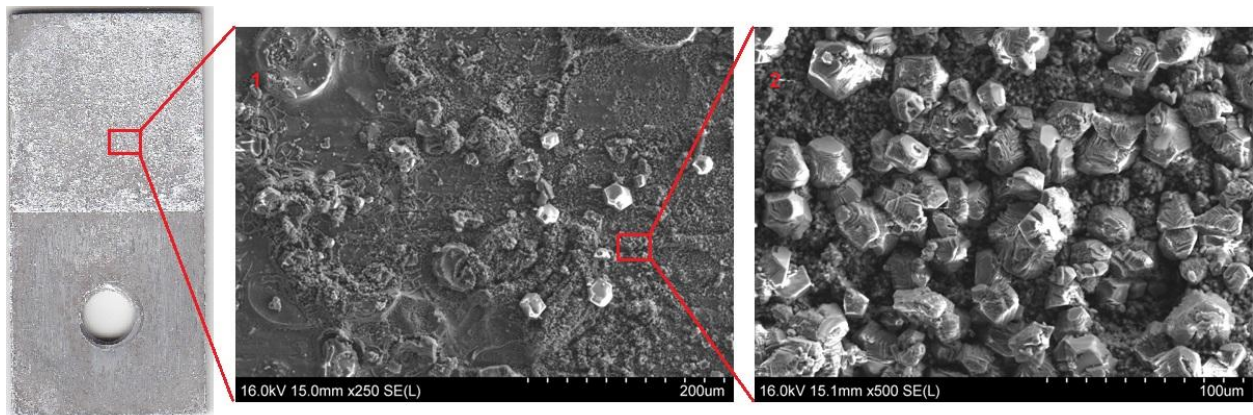


Fig. 58. SEM of uncovered region of Al coupled to stainless steel exposed in the CCTC.

Table 42: Elemental composition of regions shown in Fig. 58.

Element		O	Al	C	Ca	Na	Fe	Cl
Atomic %	Region 1	74.6	20.6	3.63	0.74	0.23	0.15	0.12
	Region 2	68.9	3.14	15.8	12.2			

In the covered region, however, some regions of the Al were exposed. In one such region on the Al coupon coupled to Ag, an abundance of unfamiliar flakes of product were found

(Fig. 59). The elemental analysis on these products showed a composition of mostly silver and oxygen and are thought to be elemental silver or silver oxide from the Ag coupon (Table 43).

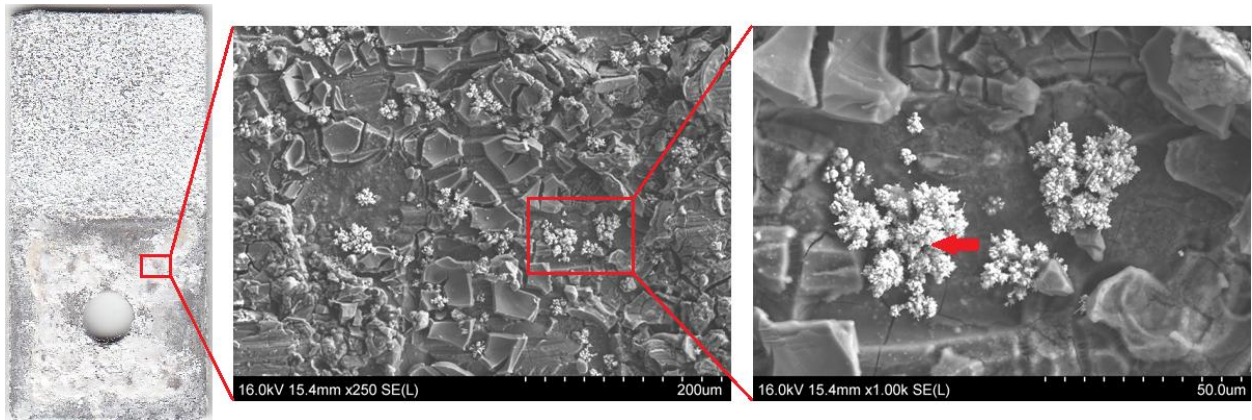


Fig. 59. SEM of covered region of Al coupled to Ag exposed in the CCTC.

Table 43: Elemental composition of regions shown in Fig. 59.

Element		O	Al	C	Na	Ag	Ca	Mg
Atomic %	Region	74.9	16.9	3.8	2.21	1.21	0.71	0.24
	Flakes	50.7	2.85		1.00	42.8		0.39

Both covered and uncovered regions of Al coupled to Cu were obscured by thick layers of product and the base Al underneath was difficult to view using SEM. Fig. 60 is a micrograph of the product covering the Al coupon in the region of the couple underneath the Cu coupon; the corresponding elemental analysis of this layer is shown in Table 44.

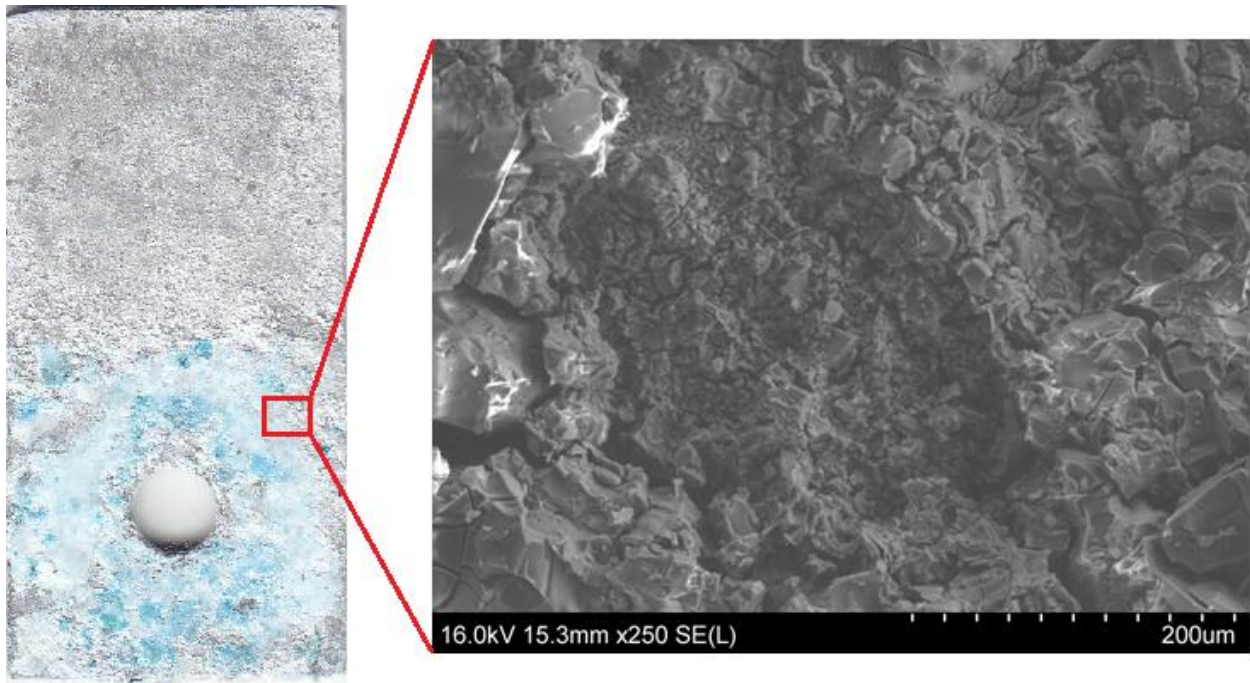


Fig. 60. SEM of covered region of Al coupled to Cu exposed in the CCTC.

Table 44: Elemental composition of region shown in Fig. 60.

Element	O	Al	C	Cu	Cl
Atomic %	74.8	20.7	4.04	0.41	0.12

The two types of coupled Al with the lowest amount of corrosion in the X-on-top orientation, those coupled to Ti and Mg, showed visible corrosion in the crevices (Figs. 61 and 62). Their elemental compositions consisted of elements in the salt spray and the Al coupon (Tables 45 and 46).

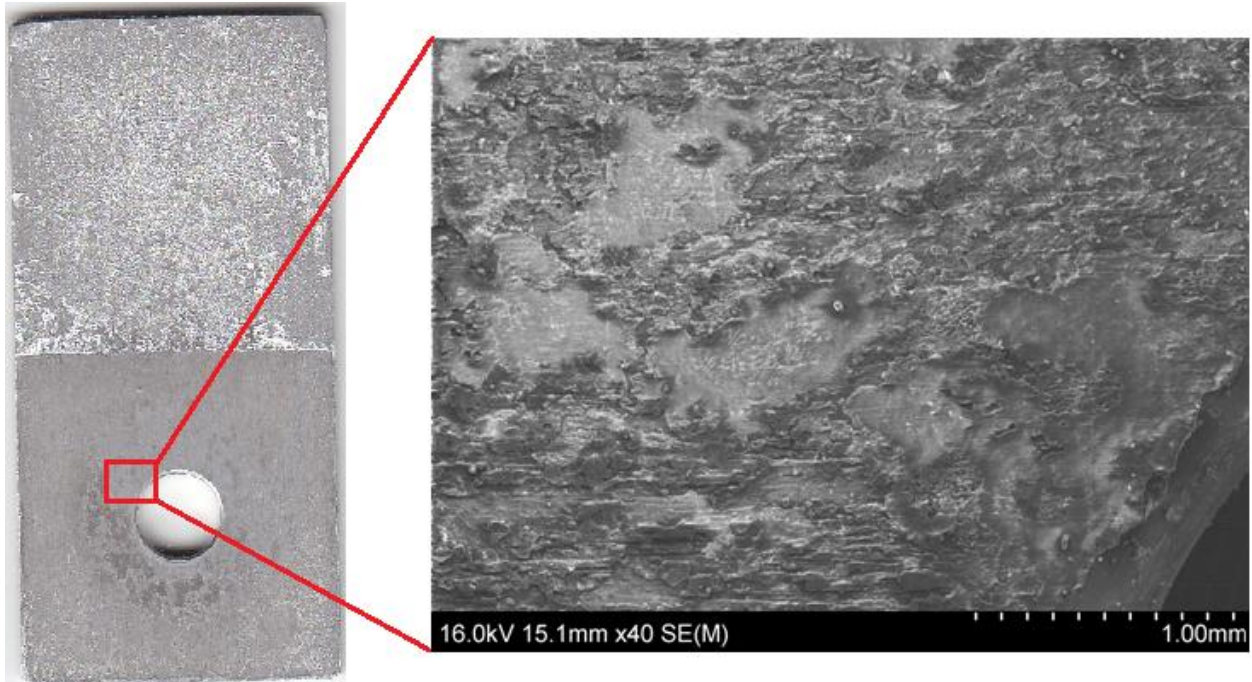


Fig. 61. SEM of uncovered region of Al coupled to Ti exposed in the CCTC.

Table 45: Elemental composition of region shown in Fig. 61.

Element	O	Al	C	Na	Ca	Cl	Ti
Atomic %	75.3	21.8	2.36	0.33	0.12	0.11	<0.00

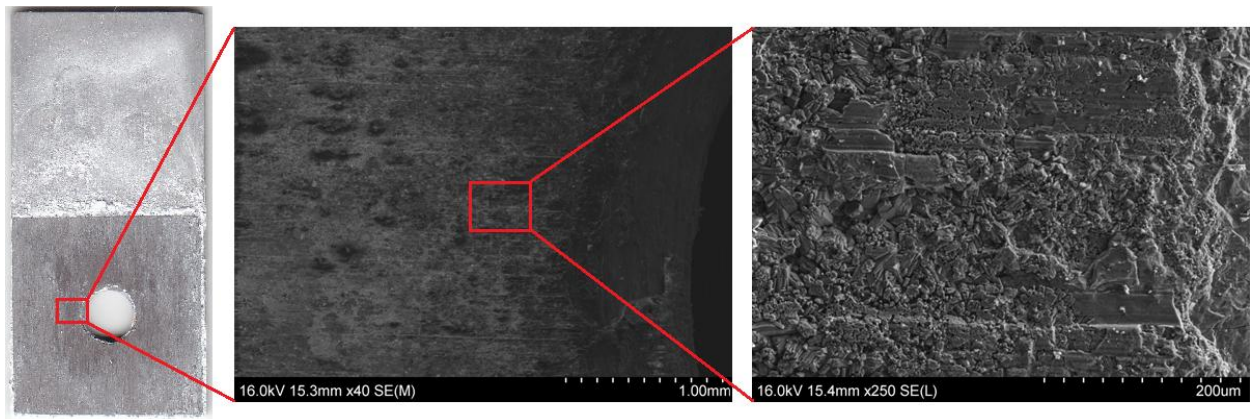


Fig. 62. SEM of uncovered region of Al coupled to Mg exposed in the CCTC.

Table 46: Elemental composition of region shown in Fig. 62.

Element	O	Al	Mg	C	Na	Ca
Atomic %	75.3	16.8	4.22	3.30	0.28	0.10

The covered region of the Al coupled to Fe was similar to that of the Al coupled to Cu in that the layer of corrosion product from the coupling metal was abundant and did not uncover the Al surface underneath (Fig. 63). The composition of this corrosion product layer is shown in Table 47. The layer is shown to consist of mostly iron and aluminum oxides, as well as elements from the salt spray.

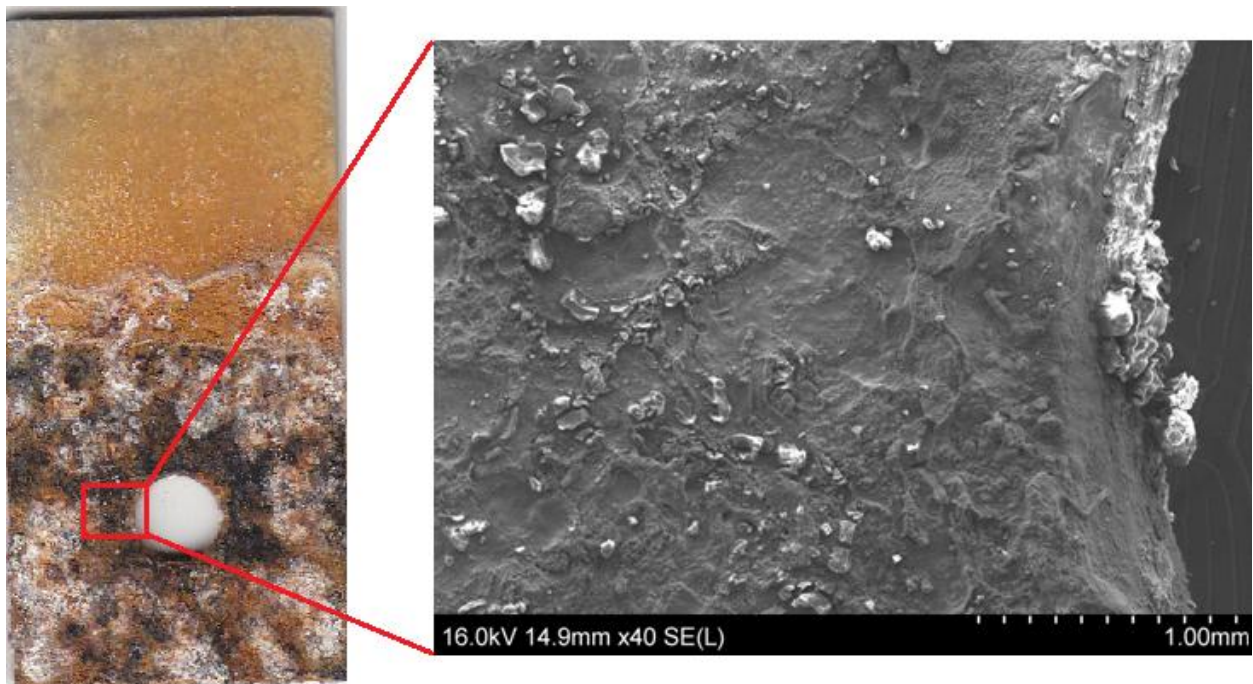


Fig. 63. SEM of covered region of Al coupled to mild steel exposed in the CCTC.

Table 47: Elemental composition of region shown in Fig. 63.

Element	O	Al	Fe	C	Na
Atomic %	67.5	16.6	11.5	2.92	1.51

6.2. X-ray diffraction analysis

X-ray diffraction (XRD) analysis was performed using a Rigaku MiniFlex II Desktop X-ray Diffractometer on the corroded Al samples from the sets of uncoupled Al and coupled Al in the X-on-top orientation. Diffraction patterns for the coupled Al were obtained in the region covered by the corresponding metal in order to obtain a comparison of corrosion product. Comparisons were performed between a single type of Al set at every exposure location as well as between every type of Al set at a single exposure location. The International Centre for Diffraction Data library was used to characterize peaks displayed in the spectra.

6.2.1. Comparison of Al spectra by location

In order to identify corrosion products formed by exposure, an initial spectra of virgin unexposed Al was obtained (Fig. 64). In descending order of intensity, the peaks identified were of 44.7° , 38.4° , 65.1° , 78.2° , 82.4° , and 22.4° . These peaks were used to identify which peaks in the spectra of the exposed Al were of the base metal itself.

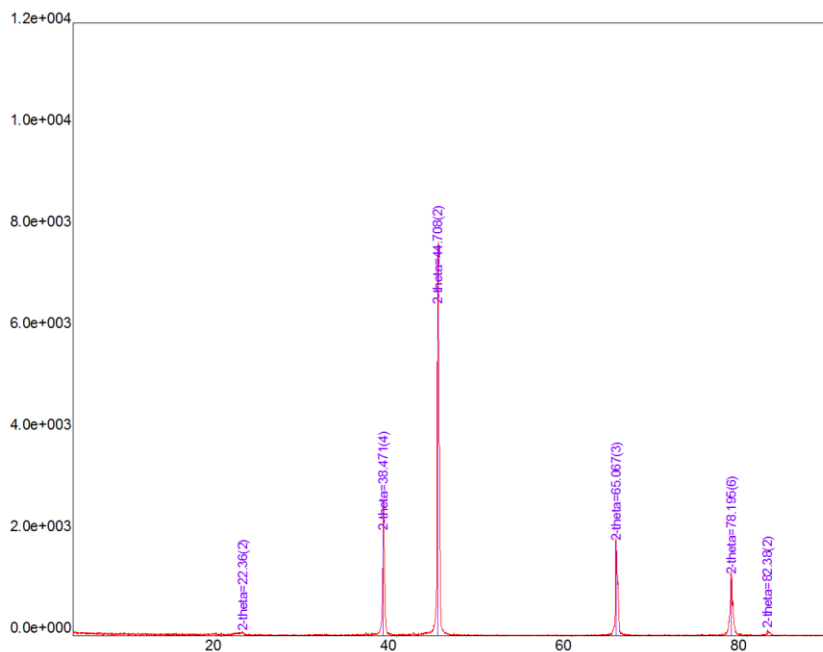


Fig. 64. XRD spectra of virgin Al coupon.

Spectra were obtained of the uncoupled Al coupons from each exposure site. Fig. 65 displays an overlay of these spectra.

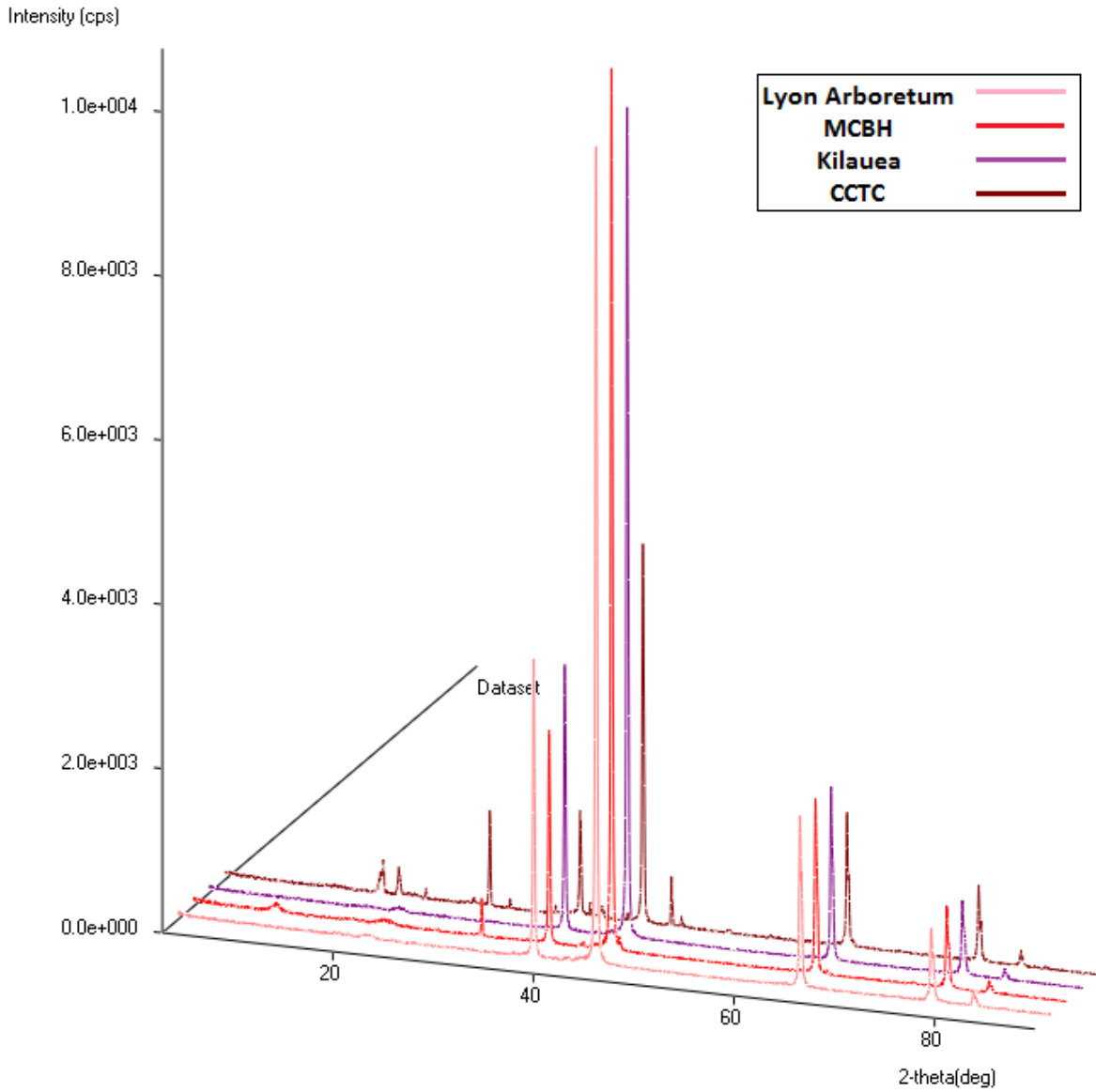


Fig. 65. XRD spectra overlay of unexposed Al at each exposure location.

Relative intensities for the base Al peaks were much lower for the uncoupled Al exposed in the CCTC than the other sites. The outdoor sites, which had roughly the same corrosion rate, show

similar intensities in their base metal peaks. The two peaks shown at 18.8° and 20.3° correspond to the peaks of aluminum hydroxide $\text{Al}(\text{OH})_3$, a common corrosion product of aluminum when reacted with water. Additional peaks in the unexposed Al from the CCTC at 23.1° , 29.4° , 31.4° , 39.4° , 43.1° , 47.5° , and 48.5° correspond to calcium carbonate CaCO_3 which during SEM and EDXA analysis was shown to be abundant on the samples exposed in the CCTC. The Al exposed at MCBH also display low peaks in the ranges of calcium carbonate.

The spectra of Al coupled to Ag are displayed in Fig. 66. The $\text{Al}(\text{OH})_3$ peaks appeared for all test sites except for Kilauea at which Al had the lowest corrosion rate. The intensity of the base metal peaks for the Al at Kilauea also remained much higher than the Al exposed at the other test sites. The higher intensity of the base metal peaks also indicated that the oxide film was thinner, which could also be attributed to the acid rain at Kilauea that dissolved the aluminum oxide corrosion products preventing its buildup. Calcium carbonate on the sample from the CCTC remained abundant.

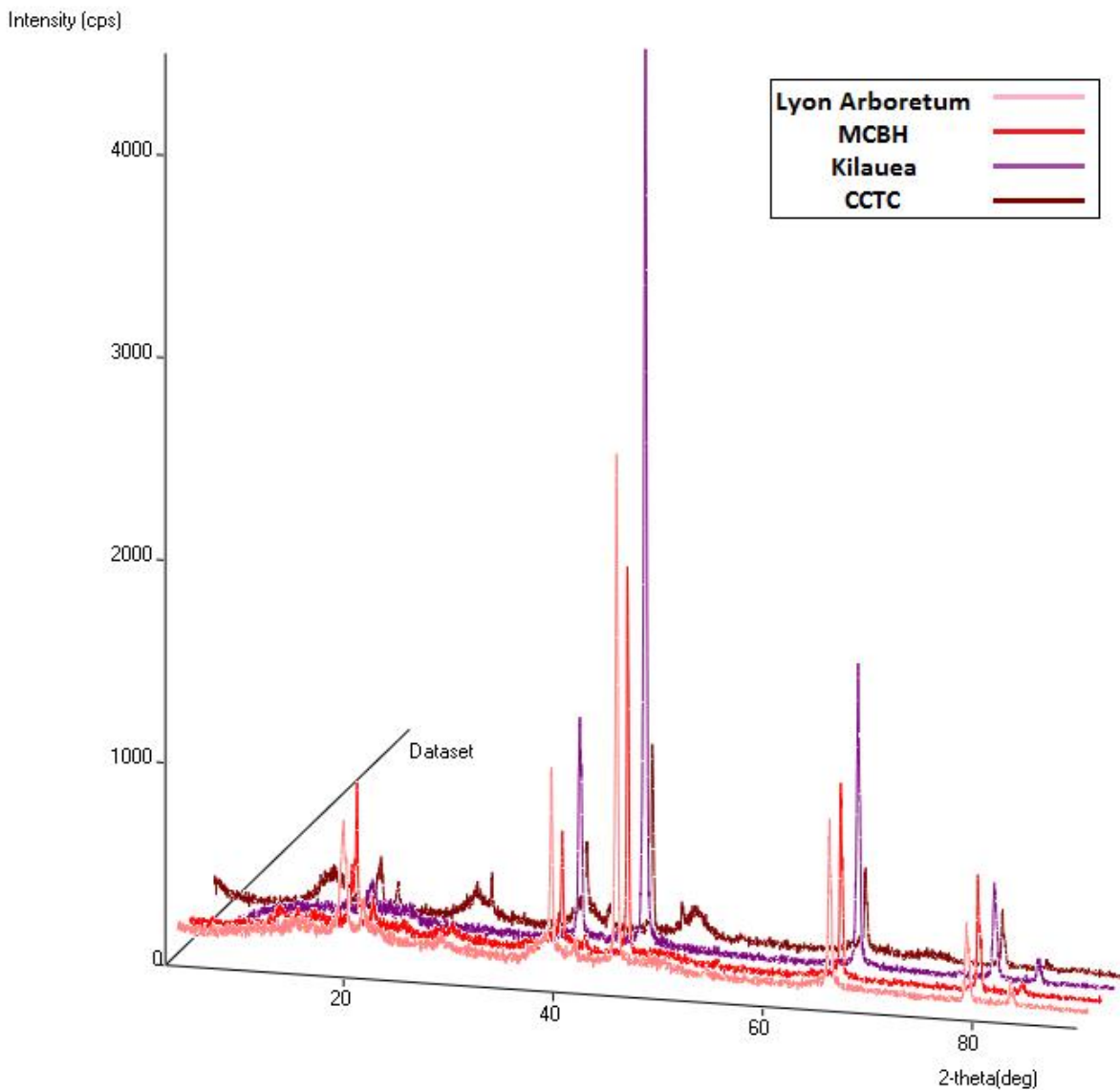


Fig. 66. XRD spectra overlay of Al coupled to Ag at each exposure location.

The Al coupled to Cu produced broad peaks for Al at all locations (Fig. 67). The abundance of corrosion product on these samples produced many peaks of varying intensities. Common to each sample was the presence of Al(OH)₃, even at the Kilauea test site.

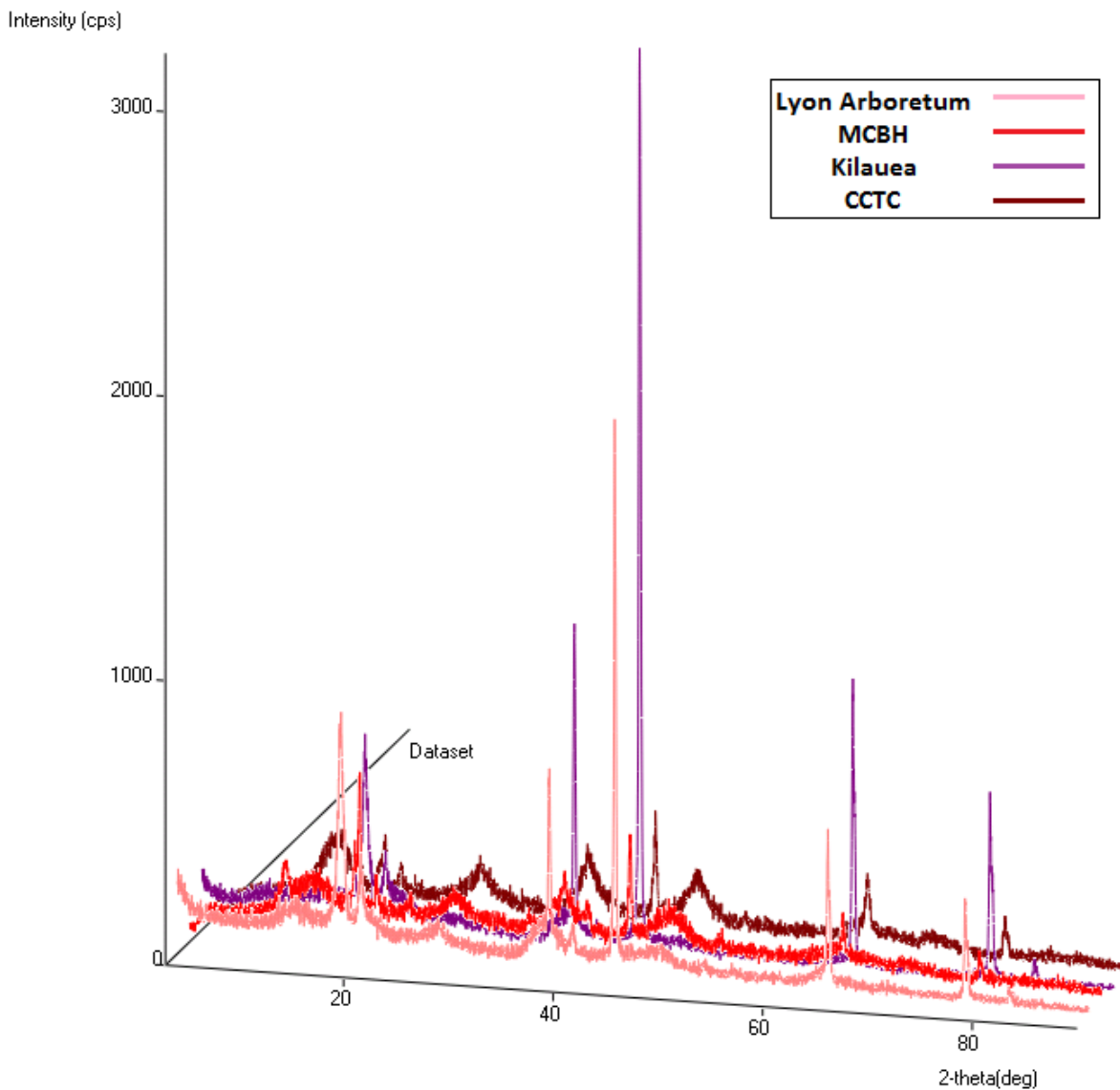


Fig. 67. XRD spectra overlay of Al coupled to Cu at each exposure location.

Al coupled to Ti produced the spectra most similar to that of the base metal (Fig. 68). The Al(OH)_3 peaks are most intense in the CCTC location. The Al at MCBH displays a peak at 31.7° which could possibly be attributed to calcium carbonate which the EDXA confirms was abundant at this location.

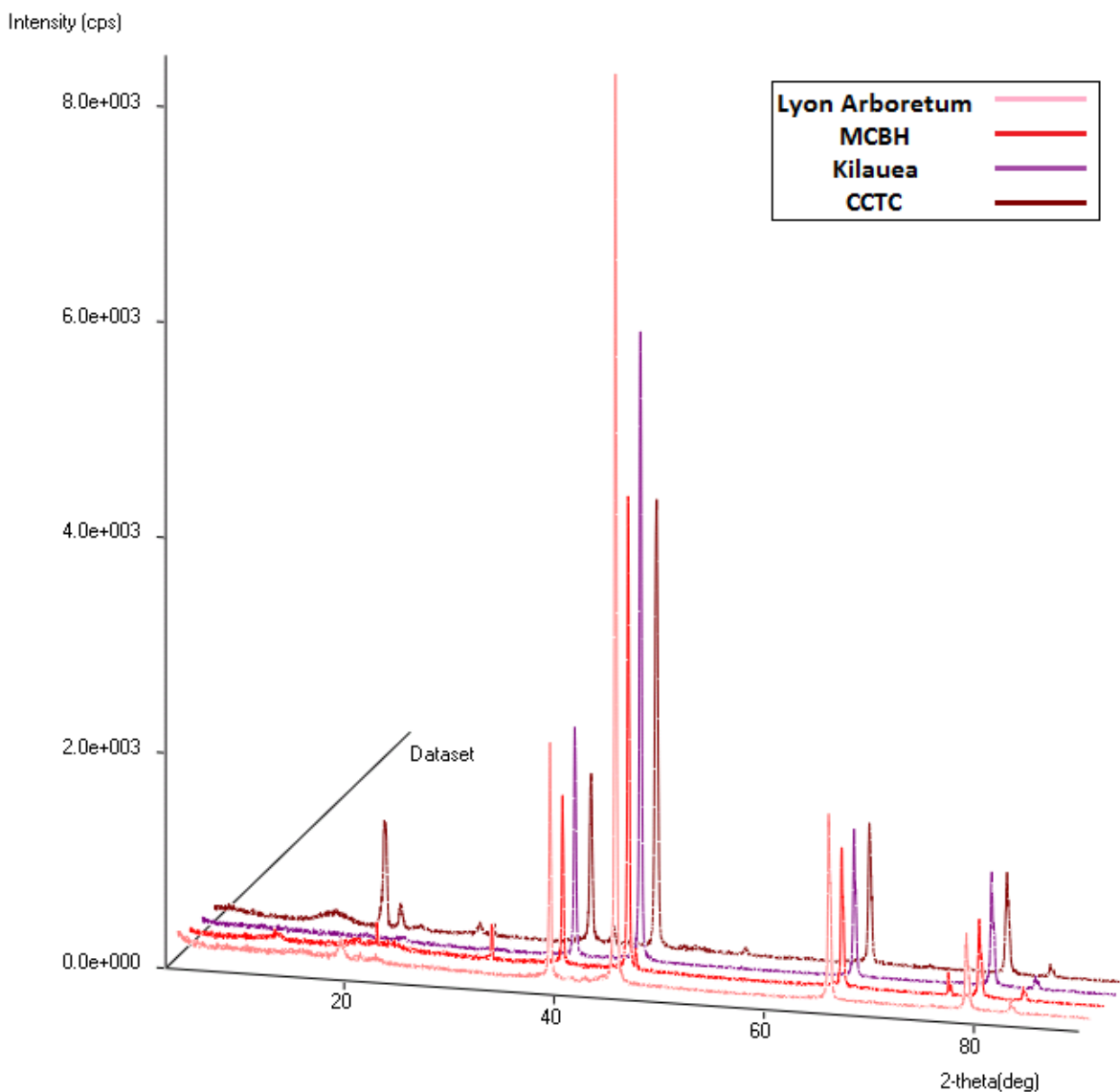


Fig. 68. XRD spectra overlay of Al coupled to Ti at each exposure location.

The spectra for Al coupled to stainless steel are shown in Fig. 69. Noticeable in this case was the splitting pattern shown for peaks at 18.5° and 19.0° for the Al at MCBH. The library analysis matched the slightly higher peak, along with the 20.3° peak, with aluminum oxide hydrate $\text{Al}_2\text{O}_3 \cdot 3\text{H}_2\text{O}$. It is possible that this sample retained moisture, causing this pattern to occur.

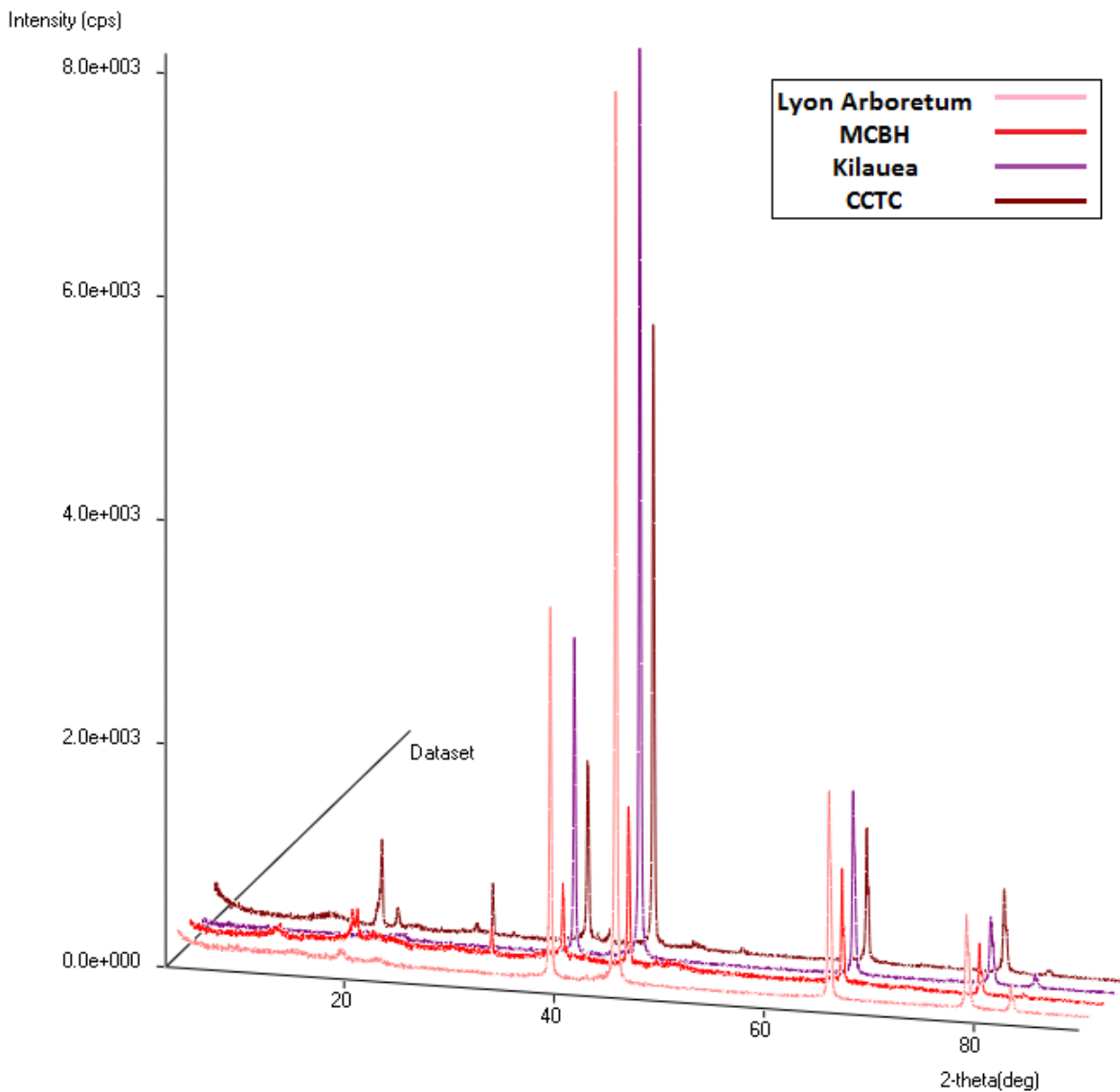


Fig. 69. XRD spectra overlay of Al coupled to stainless steel at each exposure location.

Similar to the Al coupled to Cu, the Al coupled to mild steel produced spectra with very broad peaks and low intensity due to the thick layer of corrosion product present on the sample (Fig. 70). Albeit with the lowest intensity compared to every other Al couple type, $\text{Al}(\text{OH})_3$ peaks were identified at the Lyon Arboretum, MCBH, and Kilauea sites. These peaks were not

identified on the sample exposed in the CCTC, likely due to the excess of corrosion product from the mild steel.

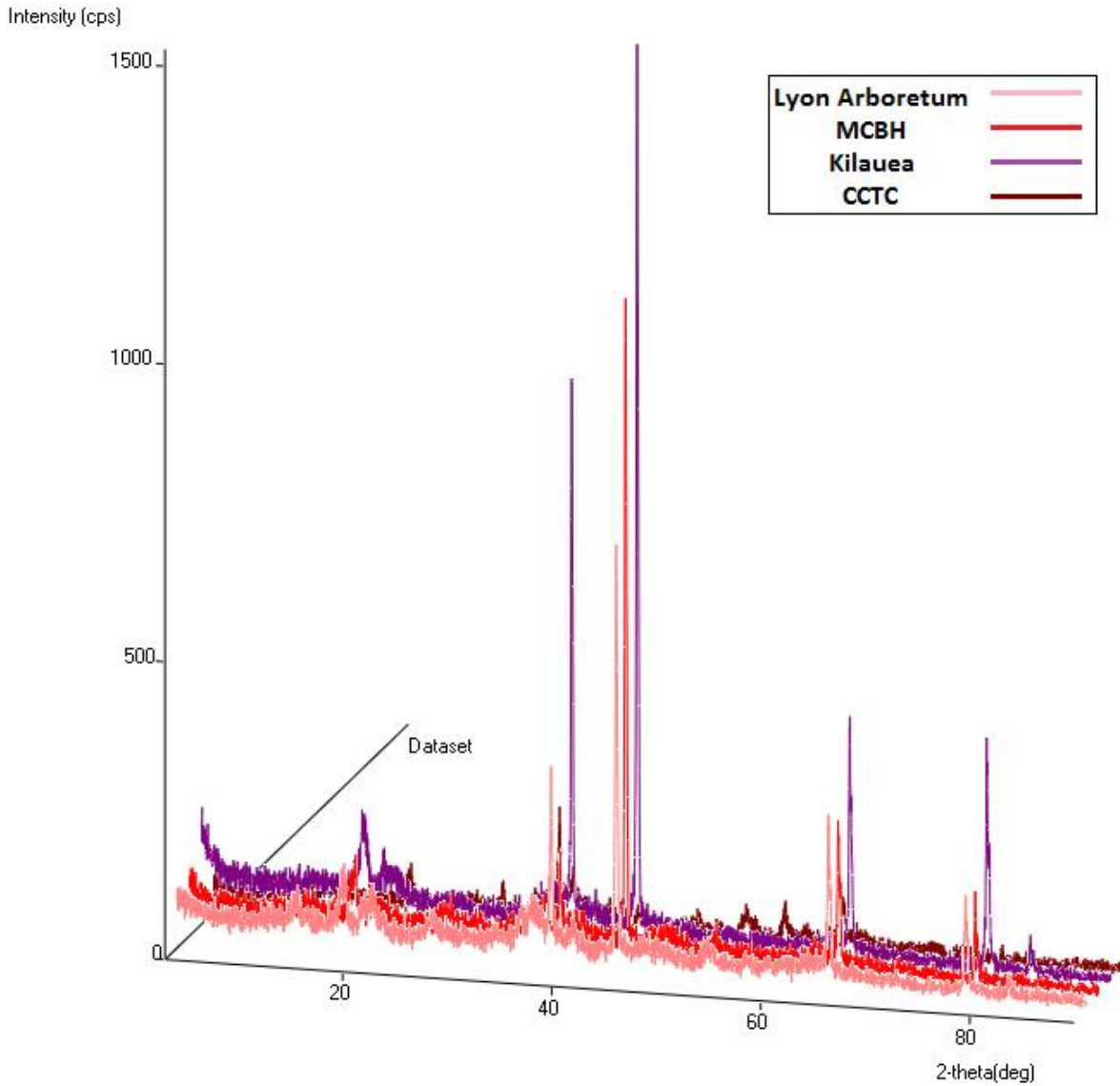


Fig. 70. XRD spectra overlay of Al coupled to mild steel at each exposure location.

The spectra for the Al coupled to Mg at each test site is shown in Fig. 71. Again, the splitting pattern between the peaks of $\text{Al}(\text{OH})_3$ and $\text{Al}_2\text{O}_3 \cdot 3\text{H}_2\text{O}$ is noticeable in the Al from MCBH and the CCTC. An additional peak upstream at 11.7° in the Al sample from the CCTC

matches a library spectra of magnesium aluminum hydroxide hydrate $Mg_4Al_2(OH)_4 \cdot 3H_2O$. A compound containing magnesium and the aluminum corrosion product is feasible in this sample.

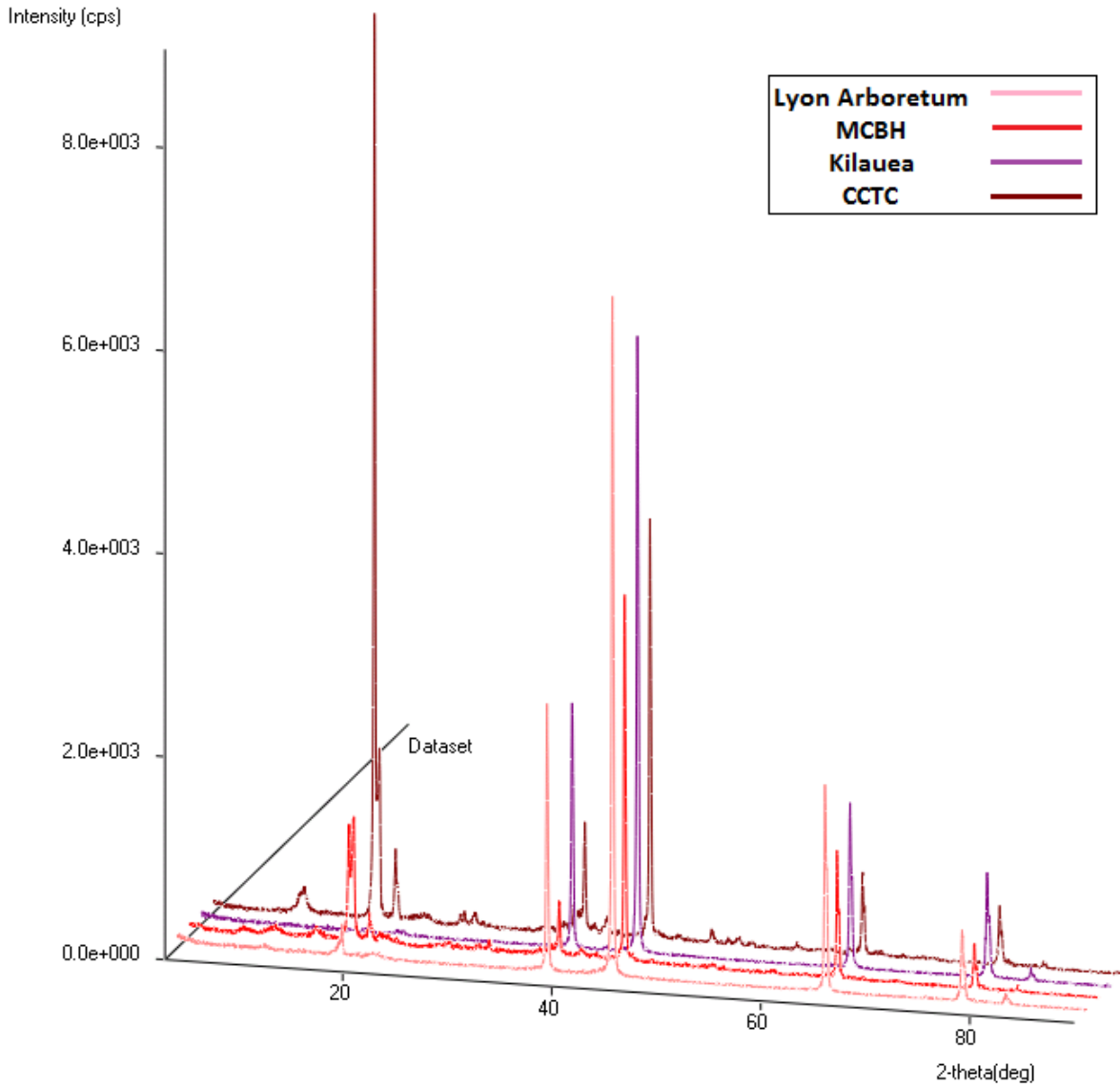


Fig. 71. Overlay of Mg coupled to stainless steel at each exposure location.

6.2.2. Comparison of Al spectra by couple type

The comparison of each spectra by the metal to which it was coupled shows the intensities of the peaks relative to each other in order to highlight the differences in corrosion behavior. Spectra of each type of Al sample exposed at Lyon Arboretum are shown in Fig. 72.

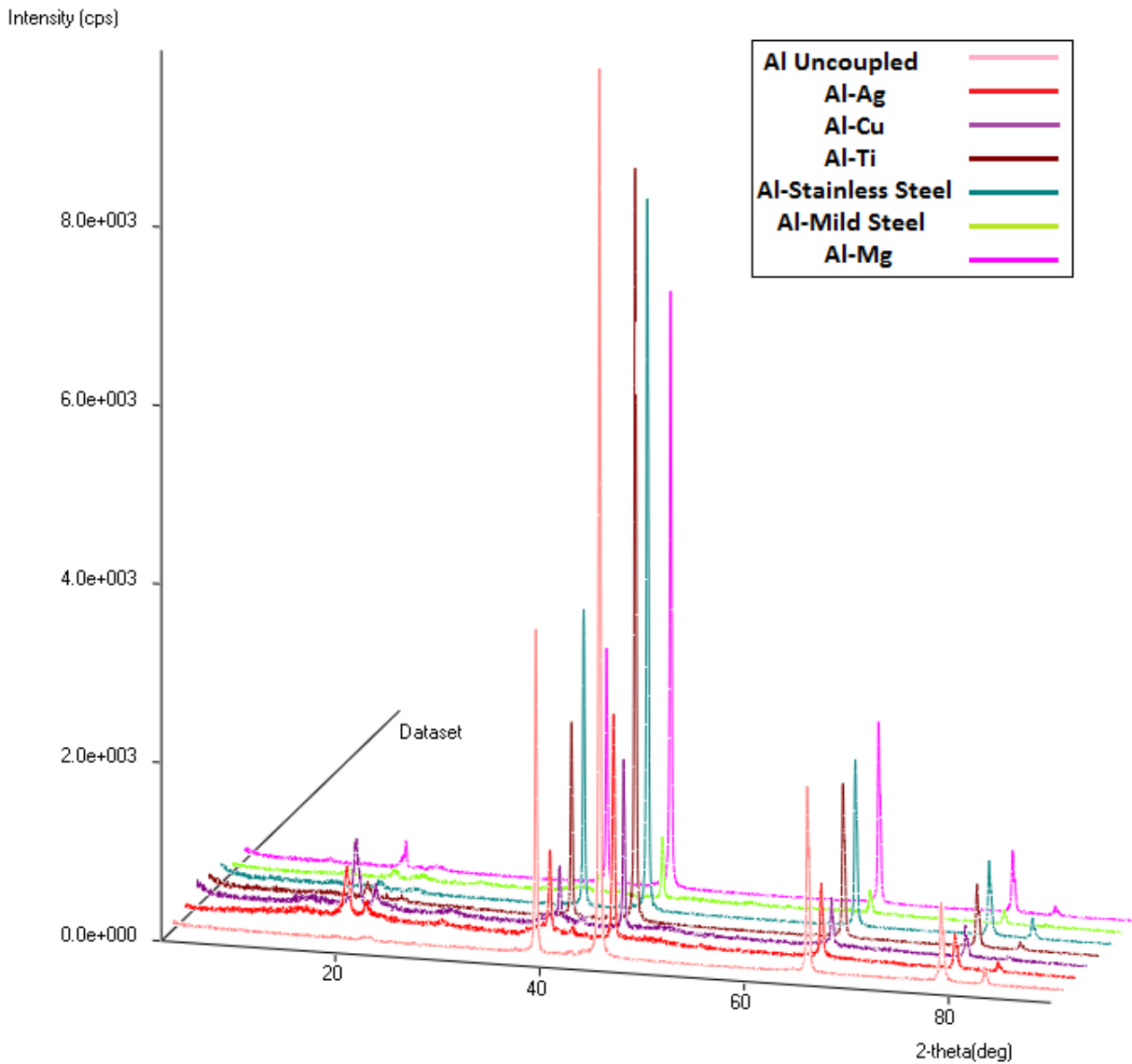


Fig. 72. XRD spectra overlay of all exposed Al types at Lyon Arboretum.

At Lyon Arboretum, the peaks for $\text{Al}(\text{OH})_3$ are most pronounced for the Al coupled to Ag and to Cu while having the lowest intensity for the base metal peaks. This correlates to these two couple types experiencing the highest corrosion rate. The intensity of the base metal peaks is also low for Al coupled to mild steel, which experienced the next highest corrosion rate. Base metal peaks for Al coupled to Ti, stainless steel, and Mg were lower than in the uncoupled Al, albeit not as severe as in the former three couple types.

The spectra for the Al exposed at MCBH are shown in Fig. 73.

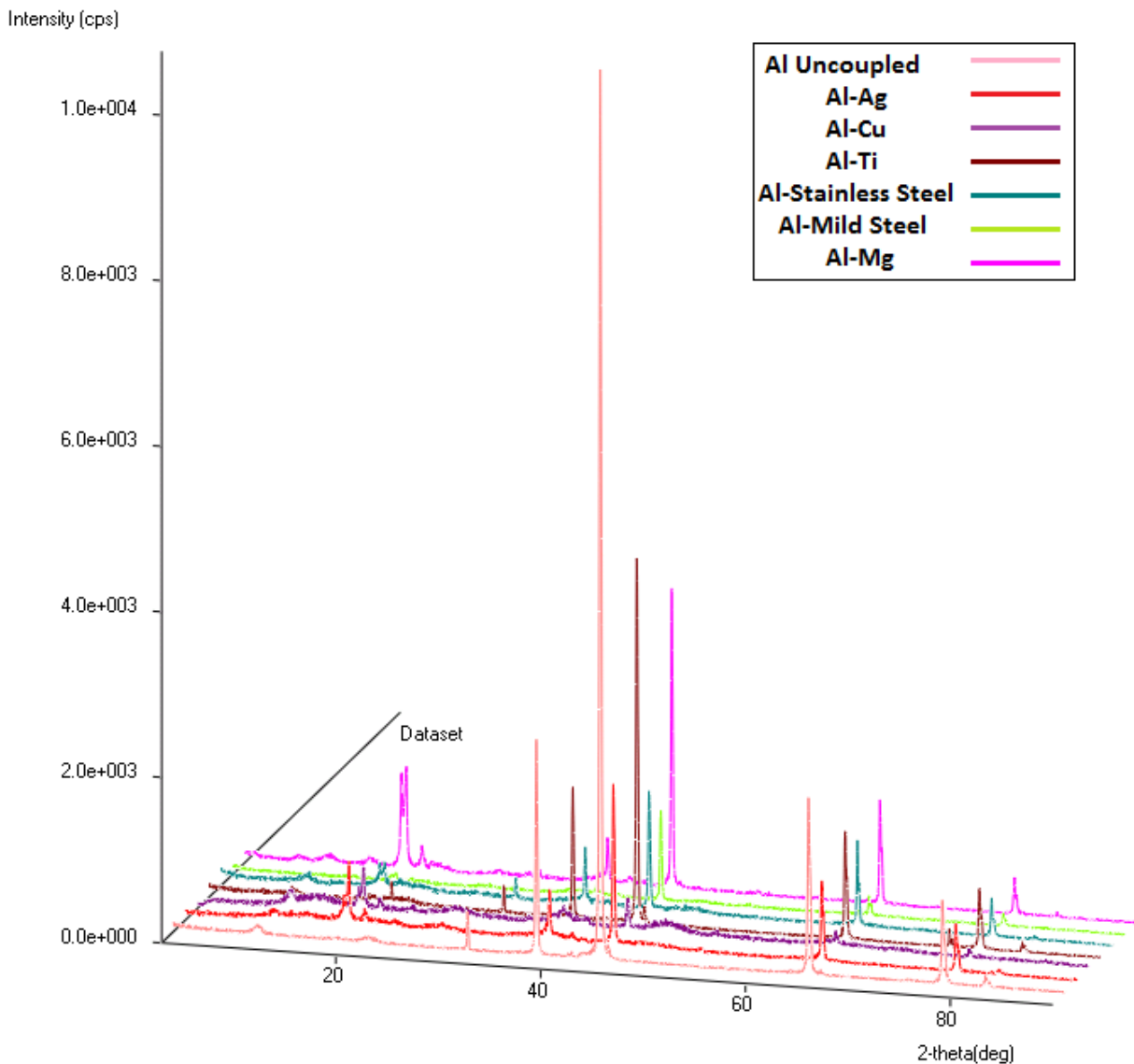


Fig. 73. XRD spectra overlay of all exposed Al types at MCBH.

The peak intensities for the base metal vary drastically between the uncoupled Al and the coupled metals at MCBH, which is in accordance with the coupled Al having the highest disparity in corrosion of the coupled Al versus the uncoupled Al. Peaks corresponding to calcium compounds were observed between couple types, likely due to the environment.

The spectra for the couple types exposed at Kilauea are shown in Fig. 74.

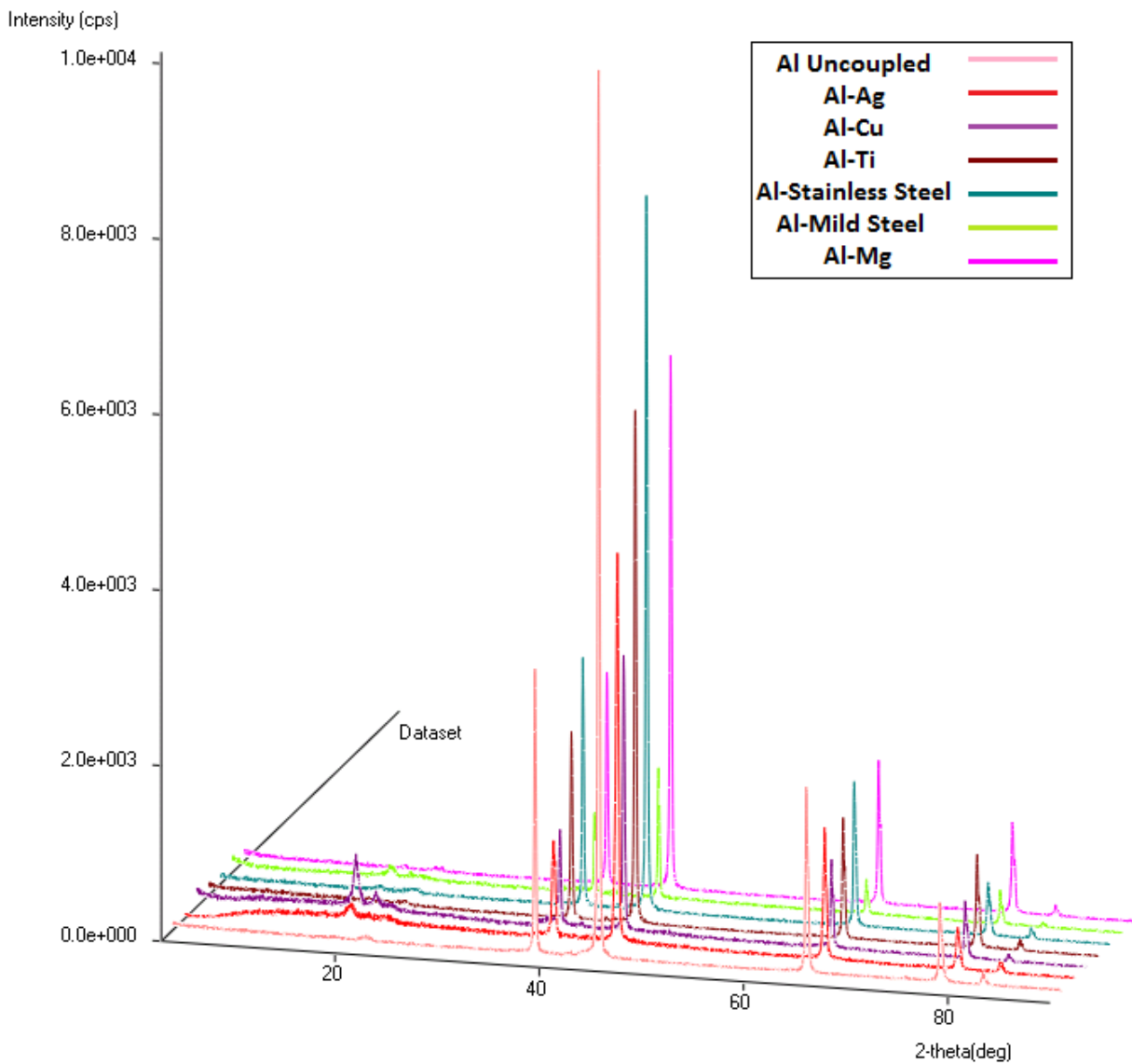


Fig. 74. XRD spectra overlay of all exposed Al types at Kilauea.

Similar to Lyon Arboretum, the presence of $\text{Al}(\text{OH})_3$ is most noticeable for the Al coupled to Ag and Cu with slight peaks seen for Al coupled to mild steel. Although the Al coupled to Ti and stainless steel experienced roughly the same corrosion rate, the peak intensities for Al-Ti are generally lower than those for Al-stainless steel. This may be due to the region in which the spectra was obtained; the covered region of Al may have been more corroded in the Al-Ti couple than for the Al-stainless steel couple.

Fig. 75 displays the spectra for all exposed Al types in the CCTC. Here we see an extremely high intensity peak for Al which was coupled to Mg—this is likely due to the combination of both aluminum hydroxide and magnesium hydroxide. $\text{Al}(\text{OH})_3$ peaks are seen for most samples including the uncoupled Al, though by comparison the intensity of these peaks for Al coupled to mild steel is relatively low. However, since Al coupled to mild steel had the third highest corrosion rate in the CCTC, this again may be attributed to the large amount of corrosion product obscuring the diffraction of the Al.

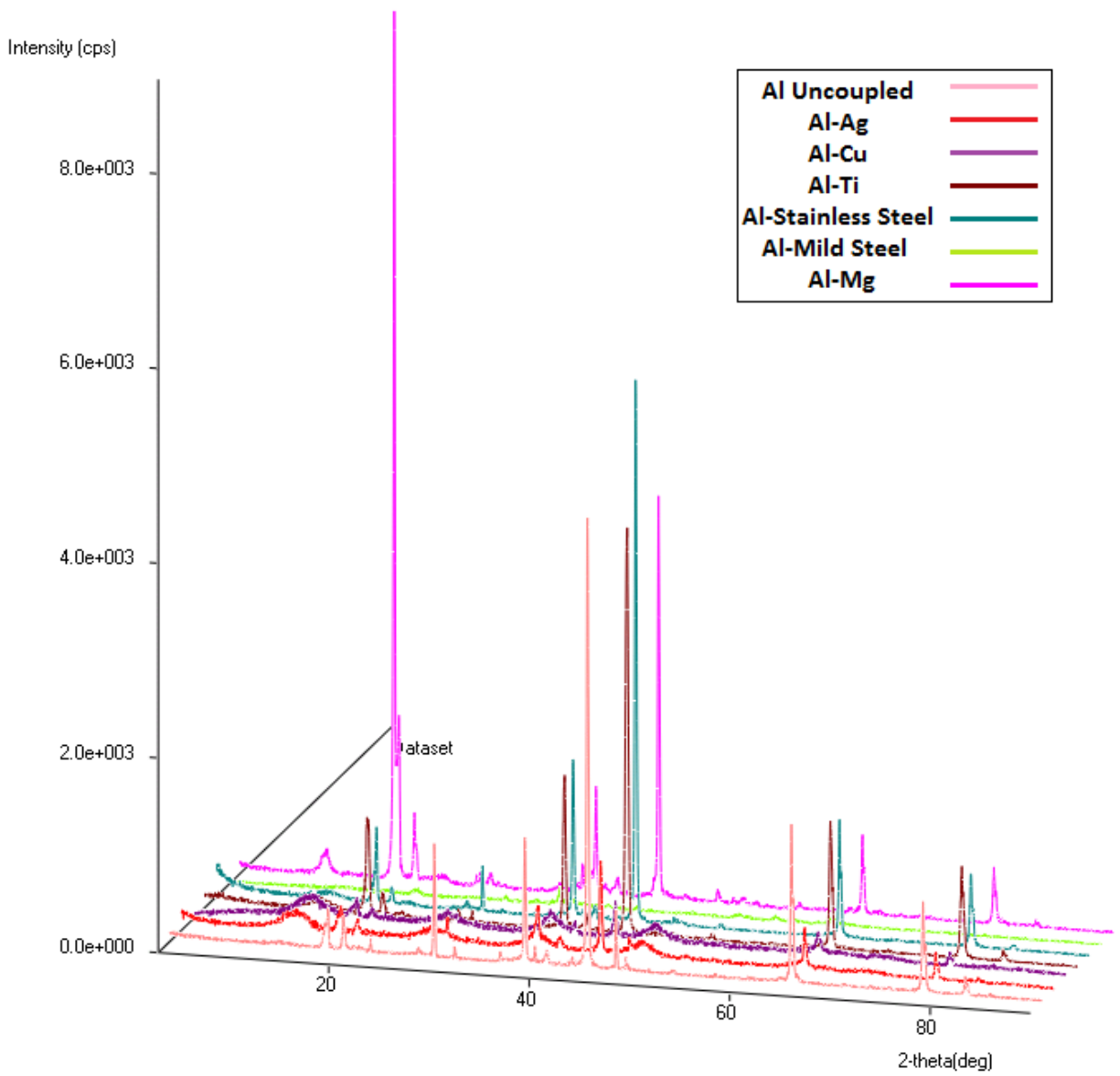


Fig. 75. Overlay of all exposed Al types in the CCTC.

Chapter 7: Conclusions

The results of the potentiodynamic polarization experiments highlight the importance of field data in conjunction with laboratory data. While the mild steel acted as anodic to Al in the sodium sulfate solution, in every iteration of exposure testing the galvanic current data showed that mild steel was the cathode when coupled to Al. Also of significance regarding outdoor testing is that even when exposed in a naturally chloride-heavy marine environment, the uncoupled Al retained its passive layer and was highly resistant to corrosion; whereas, in the accelerated test chamber, the combination of cyclic salt spraying, high humidity, and high temperatures up to 60°C significantly caused more passive-film breakdown and pitting, lowering the ratio of total corrosion between the coupled Al versus the uncoupled Al. The Kilauea test site was expected to have the third highest corrosion rate due to the proximity of the ocean to the volcano; however, in practice Lyon Arboretum proved to be the more corrosive environment.

For all couple types in which Al was the anode, galvanic current only accounted for a small fraction of the total mass loss. Local corrosion was likely accelerated due to the development of pH gradients caused by the separation of the anode and cathode. The physical coupling of Al to another metal also increases corrosion due to crevice corrosion in addition to galvanic coupling. For the noble metals, the composition analysis of the pits in the region of Al not covered by the Cu or Ag coupons showed an increased amount of these elements; this suggests local corrosion acceleration by precipitation of Cu or Ag onto the Al surface creating cathodic sites. For the mild steel, iron corrosion products were abundantly present on the Al surface both in the uncovered and covered regions, which may have also accelerated corrosion. For the passivating alloys, i.e. stainless steel and Ti, the contamination of the Al by these metals

was minimal, suggesting that the corrosion-accelerating factors in addition to galvanic corrosion were pH gradients and crevice corrosion. Thus, in practice, the total corrosion of many types of an aluminum-containing galvanic couple may not be estimated simply by the galvanic component of corrosion in addition to the local corrosion rate as calculated by uncoupled aluminum.

The Mg did not show as dramatic a difference in the local corrosion of the uncoupled metal versus the coupled Mg. The fraction of calculated galvanic corrosion to actual total corrosion of Al was fairly consistent with the component of local corrosion as calculated by the mass loss of the uncoupled Mg. Without the ability to passivate and also being an active metal, Mg does not have the innate corrosion resistance as Al does and, thus, does not exhibit radically different corrosion behavior in a galvanic couple apart from local corrosion in conjunction with galvanic corrosion.

Consistent with the literature, the chloride-heavy environments, i.e. MCBH and the GM-9540P test in the CCTC, caused the highest amount of corrosion. The XRD data shows that the Al at these two sites produce the main Al corrosion product $\text{Al}(\text{OH})_3$ the most consistently across all couple types. Although less corrosive than the high chloride-containing sites, the volcanic site has acid rain due to the emission of SO_2 . Accordingly, high concentrations of sulfur (likely in the form of sulfate) were found in the pits on Al. The anionic SO_4^{2-} is likely to migrate into the anodic pit. The average calculated mass loss due to galvanic current was higher for all couple types at Lyon Arboretum versus Kilauea. This increase in galvanic current is thought to be due to the extremely humid and rainy environment at Lyon Arboretum; wherein, the couples are consistently exposed to the electrolyte creating a salt bridge and therefore galvanic current.

References

- ¹Wesley, W. A.; Brown, R. H. In *The Corrosion Handbook*; Uhlig, H. H., Ed.; John Wiley & Sons: New York, 1948; pp 481–496.
- ²Revie, R. W.; Uhlig, H. H. *Corrosion and Corrosion Control: An Introduction to Corrosion Science and Engineering*, 4th ed.; John Wiley & Sons: Hoboken, NJ, 2008.
- ³Huang, I.-W.; Hurley, B. L.; Yang, F.; Buchheit, R. G. *Electrochim. Acta* **2016**, *199*, 242–253.
- ⁴Mccafferty, E. *Corros. Sci.* **2003**, *45* (7), 1421–1438.
- ⁵Szklarska-Smialowska, Z. *Corros. Sci.* **1999**, *41* (9), 1743–1767.
- ⁶Blanc, C.; Mankowski, G. *Corros. Sci.* **1997**, *39* (5), 949–959.
- ⁷Datta, J.; Bhattacharya, C.; Bandyopadhyay, S. *B. Mater. Sci.* **2005**, *28* (3), 253–258.
- ⁸Dan, Z.; Muto, I.; Hara, N. *Corros. Sci.* **2012**, *57*, 22–29.
- ⁹Cui, Z. Y.; Li, X. G.; Man, C.; Xiao, K.; Dong, C. F.; Wang, X.; Liu, Z. Y. *J. Mater. Eng. Perform.* **2015**, *24* (8), 2885–2897.
- ¹⁰Ezuber, H.; El-Houd, A.; El-Shawesh, F. *Mater. Design* **2008**, *29* (4), 801–805.
- ¹¹Acevedo-Hurtado, P. O.; Sundaram, P. A.; Caceres-Valencia, P. G.; Fachini, E. R.; Miller, C.E.; Placzankis, B. E. *Corros. Sci.* **2008**, *50* (11), 3123–3131.
- ¹²Raj, X. J.; Nishimura, T. *Prot. Met. Phys. Chem. Surf.* **2016**, *52* (3), 543–554.
- ¹³Rafla, V.; King, A. D.; Glanvill, S.; Parsons, A.; Davenport, A.; Scully, J. R. *Corrosion* **2015**, *71* (10), 1171–1176.
- ¹⁴Vera, R.; Verdugo, P.; Orellana, M.; Muñoz, E. *Corros. Sci.* **2010**, *52* (11), 3803–3810.
- ¹⁵Lacroix Loïc; Blanc, C.; Pébère Nadine; Tribollet, B.; Vivier, V. *J. Electrochem. Soc.* **2009**, *156* (8).
- ¹⁶Younan, H.; Zhiqiang, M.; Siping, Z.; Hao, G. In *ISTFA 2007, Proceedings of the 33rd International Symposium for Testing and Failure Analysis*, San Jose, CA, Nov 4-8, 2007; ASM International; pp 193-196.
- ¹⁷Caspers, H. *The Ocean: A Scientific American Book*; WH Freeman & Co: San Francisco, CA, 1969.
- ¹⁸Hatch, J.E. *Aluminum: Properties and Physical Metallurgy*; ASM International, 1984.